Electronic Thesis and Dissertation Repository

8-12-2013 12:00 AM

The atmospheric chemistry of magnetic Bp stars

Jeffrey D. Bailey
The University of Western Ontario

Supervisor
Dr. John D. Landstreet
The University of Western Ontario

THE ATMOSPHERIC CHEMISTRY OF MAGNETIC BP STARS

(Thesis format: Integrated Article)

by

Jeffrey Bailey

Graduate Program in Astronomy

A thesis submitted in partial fulfillment
of the requirements for the degree of
Doctor of Philosophy

The School of Graduate and Postdoctoral Studies
The University of Western Ontario
London, Ontario, Canada

Abstract

The chemically peculiar magnetic A- and B-type (Ap/Bp) stars are characterised by large overabundances, of the order of 10^2 and 10^4 times the Sun, of Fe-peak and rare earth elements, respectively. Further, they possess strong, ordered magnetic fields (of order 1 kG) that are roughly dipolar in nature. We present in-depth investigations of magnetic Ap/Bp stars, ranging from detailed analyses of specific stars to larger surveys aimed at studying stratification and atmospheric abundance evolution.

For HD 133880 and HD 147010, we offer complete investigations of their magnetic fields and chemical abundance distributions. For each star, a simple magnetic field model is derived, from both line-of-sight and surface magnetic field measurements, that consists of dipole, quadrupole and octupole components. Abundance analysis is then performed using ZEEMAN, a spectrum synthesis program that takes into account the effects of the magnetic field.

Discrepant results between abundances derived from Si II and Si III in B-type stars has been documented in the literature. We report on the first comprehensive study of this phenomenon in various classes of B-type stars (including the non-magnetic HgMn and normal stars and magnetic Bp stars) ranging in effective temperature from about 11000 to 15000 K. We interpret the results in the context of vertical stratification in the atmospheres of these stars.

The abundance anomalies that exist in magnetic Ap/Bp stars are known to be produced by diffusion processes, when the gravitational settling of ions competes with radiative levitation. However, nothing is known about how these abundance anomalies may evolve during the main sequence lifetime of these stars. We present an extensive study of the atmospheric abundances for several elements of magnetic Ap/Bp stars, that are members of open clusters or associations (and therefore have well-determined ages), and attempt to interpret the results in the context of diffusion.

Keywords: Stars: abundances, chemically peculiar, magnetic field

Co-Authorship Statement

This thesis is based on work done in collaboration with several co-authors including my supervisor J. D. Landstreet, as well as G. Wade, S. Bagnulo, J. Grunhut, M. Shultz, D. Bohlender, J. Lim, K. Wong, S. Drake, and J. Linksy. Below, I briefly describe my contributions to each project.

Chapter 2: This chapter presents the extensive study of HD 133880. This project was the idea of myself, D. Bohlender and G. Wade. I was responsible for determining the star's physical parameters, deriving the magnetic field model (including the magnetic field modulus measurements) and performing the abundance analysis. I wrote the majority of the manuscript, excluding the sections on the period refinement and magnetosphere (G. Wade), the line profile variations (J. Grunhut) and the longitudinal magnetic field measurements (M. Shultz).

Chapter 3: This chapter presents the investigation of HD 147010. I envisioned this entire project and am responsible for writing the observing proposal that collected the data used. I performed all the analysis and wrote the entire manuscript.

Chapter 4: This chapter investigates the abundances determined using lines of Si II and Si III in B-type stars. This project was based on my analysis under the guidance of J. D. Landstreet. I am responsible for the majority of the manuscript, excluding the stratification and non-LTE effects.

Chapter 5: This chapter presents the study of the time evolution of abundances in magnetic Bp stars. This project was the idea of J. D. Landstreet, but I performed all the analysis. The discussion section was mainly the work of J. D. Landstreet, with some input from me. All other aspects of the paper were written exclusively by me, with suggestions from J. D. Landstreet.

Acknowledgements

I have had the distinct pleasure of being supervised by John D. Landstreet. I thank him for his dedication, guidance and patience. It is my sincere hope that I can inject my career with the same unwavering enthusiasm and love of science that John has displayed over the past five years that I have been at Western.

To my parents, Raymond and Johanna Bailey. Words cannot adequately express how important they are to me, nor the role they played in making me the man I am today. I thank them for their unconditional love, support and for affording me the opportunity to fulfill my potential. If asked, they will say that they are proud of what I have accomplished. To them I say that I am proud to be your son.

To the rest of my family, I thank you for your support and for always showing interest in my endeavours.

To my friends, Robbie Halonen, Alex DeSouza, Allison Hill and Megan Mattos. I thank you for necessary distractions and for friendships that will last a lifetime.

Lastly, I'd like to thank the love of my life, my wife Nicole Bailey. You are my best friend and I can't imagine a more fitting partner to journey through life with. I thank you for being my sounding board, for your encouragement and for your confidence in me.

Contents

List of Figures

List of Tables

List of Abbreviations, Symbols, and Nomenclature

Table 1: Glossary of abbreviations and symbols

Abbreviation/Symbol	Definition
Å	Angstrom
β	angle between magnetic field and rotation axes
ϵ_ν	emissivity
κ_ν	opacity coefficient
λ	wavelength
η_ν	line opacity divided by continuum opacity
η_V	ratio of Zeeman opacities
η_Q	ratio of Zeeman opacities
μ	magnetic dipole moment
μ_B	Bohr magneton
τ_ν	optical depth
ν	frequency
ρ_R	anomalous dispersion
ρ_W	anomalous dispersion
ξ	microturbulence
Am	metallic-line A-type star
Ap	chemically peculiar A-type star
$\mathbf{B}$	magnetic field vector
$\langle B \rangle$	surface magnetic field
B_d	magnetic dipole
$\langle B_l \rangle$	line-of-sight magnetic field
B_{oct}	magnetic octupole
B_q	magnetic quadrupole
B_{rms}	root mean square magnetic field
$\langle B_z \rangle$	line-of-sight magnetic field
Bp	chemically peculiar B-type star
c	speed of light
CFHT	Canada-France-Hawaii Telescope
ΔE	difference in energy between two energy levels
e	charge of an electron
	Continued on next page

Table 1 – continued from previous page

Abbreviation/Symbol	Definition
ESPaDOnS	an **E**chelle **S**ectro**P**olarimetric **D**evice for the **O**bservatio**n** of **S**tars
g	gravity
G	Gauss
g_{eff}	effective Landé factor
g_{R}	radiative acceleration
h	Planck's constant
$\hbar$	Planck's constant divided by 2π
HAeBe	Herbig Ae and Be stars
HgMn	mercury-manganese star
HJD	Heliocentric Julian Date
i	angle between line-of-sight and rotation axis
I	intensity
J	total angular momentum
K	Kelvin
L	luminosity
$\log g$	logarithm of gravity
$\log t$	logarithm of time
LSD	Least Square De-convolution
LTE	local thermodynamic equilibrium
$M_{\odot}$	solar mass
m_{e}	mass of an electron
m_{J}	magnetic quantum number
MDI	Magnetic Doppler Imaging
MiMeS	Magnetism in Massive Stars
nm	nanometer
P	period
q	quadrupole-to-dipole ratio
Q	linear polarisation at $0°$ compared to $90°$
R	spectral resolution
RV	radial velocity
S	source function
SNR	signal-to-noise ratio
S/N	signal-to-noise ratio
	Continued on next page

Table 1 – continued from previous page

Abbreviation/Symbol	Definition
T_{eff}	effective temperature
t_{exp}	exposure time
TAMS	terminal-age main sequence
U	linear polarisation at $45°$ compared to $135°$
v	velocity
V	circular polarisation
v_{R}	radial velocity
$v \sin i$	projected rotational velocity
VALD	Vienna Atomic Database
W_{λ}	equivalent width
z	Landé factor
$\bar{z}$	effective Landé factor
ZAMS	zero-age main sequence

Chapter 1

Introduction

As a proto-star contracts under the influence of gravity, it eventually stops accreting material and reaches a state of hydrostatic equilibrium (when the inward force of gravity balances the outward radiative pressure). At this point, the central pressure and temperature are high enough that it can burn H into He in the core and the proto-star becomes a star on the *main sequence*, the evolutionary state where a star will spend the majority of its lifetime. The evolution of this star on the main sequence is predominantly governed by its mass. The more massive a star is, the faster it will use up its fuel and the less amount of time it will spend on the main sequence. The luminosity L of a star (the energy it emits per unit time) is directly correlated with its mass through what is referred to as the mass-luminosity relation:

$$\frac{L}{L_\odot} = \left(\frac{M}{M_\odot}\right)^\alpha, \tag{1.1}$$

where α is generally between 3 and 4 for main sequence stars.

Observationally, the main sequence is a linear band of stars on the Hertzsprung-Russell (HR) diagram, a plot of brightness versus colour. A star's brightness is defined by its *apparent magnitude m* via the equation $m = -2.5 \log F$, where F is the stellar flux (energy per unit time per unit area)[1]. In principle, both of these quantities depend upon the wavelength (or frequency) at which the star is observed. The spectral energy distribution of a star is approximately equal to a blackbody and because each star has a different temperature, their blackbody curves peak at different wavelengths. Recall the blackbody (or Planck) distribution:

$$B_\lambda = \frac{2hc^2/\lambda^5}{e^{hc/\lambda kT} - 1}, \tag{1.2}$$

where h (= 6.626×10^{-27} erg s) is Planck's constant, c the speed of light, k (= $1.38 \times$

---

[1]By definition, a smaller magnitude means the star is brighter.

10^{-16} erg K^{-1}) Boltzmann's constant, λ the wavelength and T the temperature. Taking the derivative of the Planck function with respect to wavelength, one obtains Wien's law, the wavelength at which the radiation emitted is maximum:

$$\lambda_{\max}T = 0.29 \text{ cm K}. \tag{1.3}$$

Based on this law, a star with a temperature of about 20 000 K, would peak at a wavelength of 1450 Å, whereas a star of about 4000 K at 7250 Å. Therefore, hotter stars will appear bluer and cooler stars redder. This simple example illustrates how a star's colour, which depends upon its flux, is a function of its temperature. Specifically, a star's flux is a function of its *effective temperature*, T_{eff}, via the Stefan-Boltzmann law: $F = \sigma T_{\text{eff}}^4$, where $\sigma = 5.67 \times 10^{-5}$ ergs cm^{-2} s^{-1} K^{-4}. The effective temperature is therefore defined as the temperature at which a star actually radiates the same total flux as the equivalent blackbody.

We can now present a theoretical HR diagram of luminosity L (the energy emitted per unit time)[2] versus effective temperature. An example of an HR diagram is shown in Figure 1.1. Shown are the evolution of L and T_{eff} from the arrival of a star on the main sequence, with the hatched area on the left outlining the main sequence life, to the giant structure for stars of various mass. In general, during the main sequence lifetime of a star, T_{eff} decreases by roughly 30%, while L increases by a factor of 2 - 3, due to the substantial increase in radius. The temperature sequence defines a spectral classification scheme of O-B-A-F-G-K-M, with the O stars being the hottest and most massive and the M stars the coolest and least massive. Stars occupying the upper or lower main sequence differ structurally, transporting energy from the core to the surface in disparate ways. Below a mass of approximately 2 M$_\odot$, stars have radiative cores and convective envelopes, whereas above this threshold the opposite is true, with stars possessing convective cores and radiative envelopes.

How does the main sequence lifetime of the Sun compare to stars that are roughly 10 and 0.1 times its mass? To answer this question, assume that a star is comprised entirely of hydrogen and that about 10% of the star's mass will be converted from H to He via the simplified nuclear reaction of 4H $\longrightarrow$ 1He. Note that the mass of four hydrogen atoms ($m_{\text{H}} = 1.00782u$,where $u = 1.6605 \times 10^{-24}$ g is the atomic mass unit) is greater than the mass of a He atom ($m_{\text{He}} = 4.00260u$). Comparing the ratio,

$$\frac{4m_{\text{H}}}{m_{\text{He}}} = 1.00715,$$

---

[2]A star emits radiation nearly isotropically, therefore, if the surface flux is the amount of energy emitted per unit time per unit area, the luminosity is simply the surface flux multiplied by the area of a sphere with radius d, where d is the distance of the star from the observer.
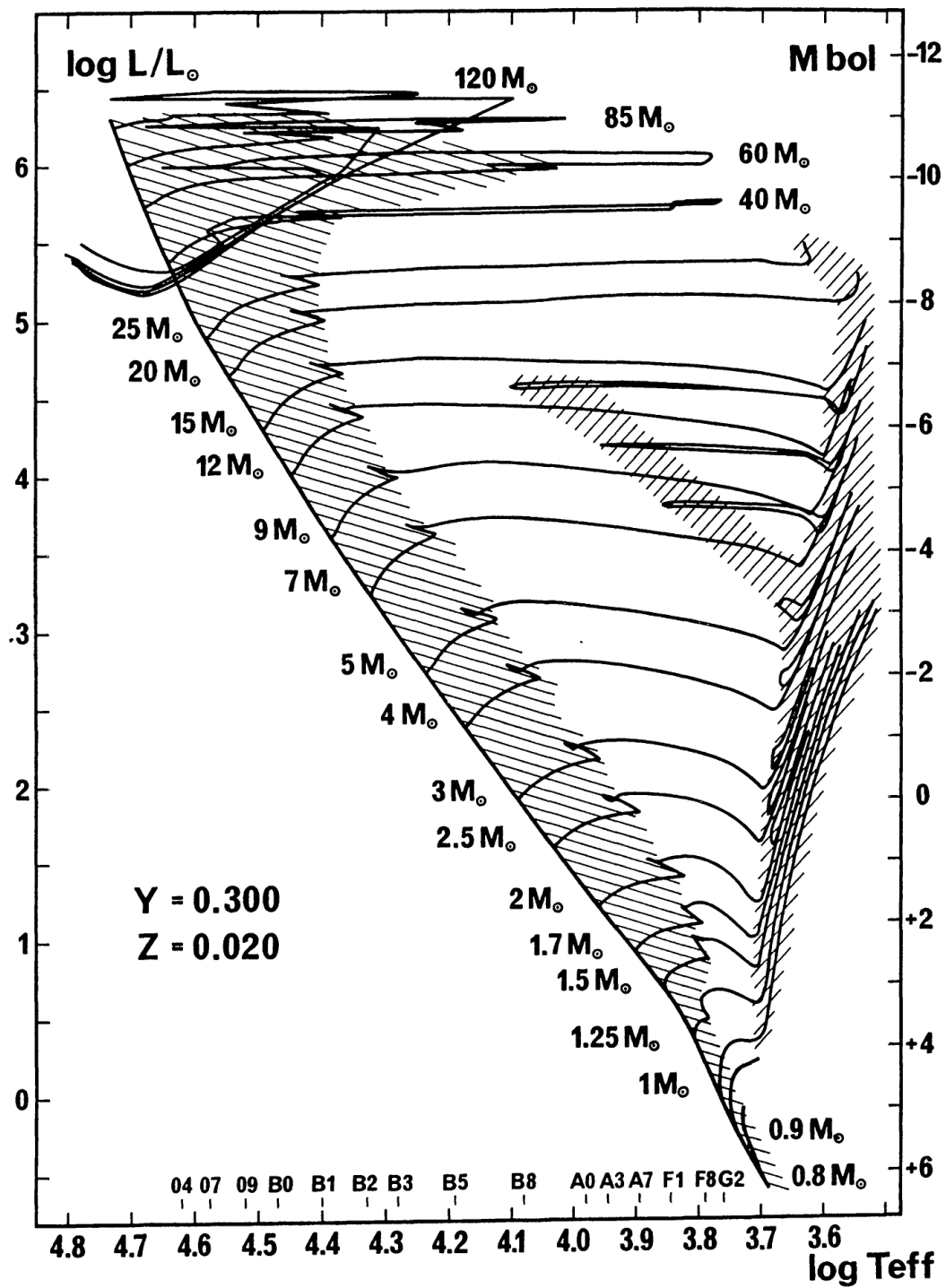
Figure 1.1: Theoretical HR diagram from Schaller et al. (1992). Of note are the zero-age main sequence (linear solid line) for various masses and their respective evolutionary tracks.

we see that roughly 0.7% of the mass of H is converted into energy when making an atom of He. Given this information, to estimate the main sequence lifetime t_{ms} of a star one simply divides the nuclear generation (or fuel) E_n by the stars luminosity (or energy output):

$$t_{ms} = \frac{E_n}{L}. \tag{1.4}$$

Substituting Equation 1.1, assuming $\alpha = 4$, into the above expression and recognising that the nuclear generation is proportional to Mc^2, the main sequence lifetime becomes,

$$t_{ms} = \frac{0.1 \times 0.007 \times M_\odot^4 c^2}{M^3 L_\odot}, \tag{1.5}$$

where $M_\odot = 2 \times 10^{33}$ g and $L_\odot = 3.826 \times 10^{33}$ ergs are the solar mass and luminosity, respectively, M is the star's mass and $c = 3 \times 10^{10}$ cm/s is the speed of light. Thus, a solar-like star will spend about 10^{10} yrs on the main sequence, while a 0.1 $M_\odot$ and 10 $M_\odot$ star will spend of order 10^{13} yrs and 10^7 yrs, respectively.

Stars that were formed in the last several billion years have bulk compositions similar to that of the Sun. On the lower main sequence (roughly mid to late[3] F stars and later), the deep convective cells keep the stellar surface well mixed and roughly homogeneous, resulting in little measurable star-to-star variations in chemistry. Further, the strong stellar winds in the O- and early B stars of the upper main sequence induce mass loss rates in these stars such that chemical peculiarities cannot develop (Landstreet, 2004). The stellar winds in the hottest stars are driven by radiation pressure, the exact same phenomenon that, in its weaker form, acts to produce the abundance anomalies in middle main sequence stars and has almost no effect in the less massive lower main sequence stars that have small radiative fluxes. However, the middle main sequence (roughly early F to late B stars) can exhibit atmospheric abundance anomalies, with variations between stars, that are drastically different from what is found in the Sun. We refer to this phenomenon as being *chemically peculiar*. This makes the A and late B stars of great interest to study.

In this chapter a review of the chemically peculiar stars, with emphasis on the magnetic peculiar A- and B-type stars (Ap/Bp), is presented. We further discuss the magnetic field signatures in stellar spectra, with particular consideration given to how these fields are measured. Lastly, the physics of spectral line formation and the use of spectrum synthesis to compute an observed emergent spectrum is explored.

---

[3]The expression *early type* refers to hotter stars, whereas *late type* refers to cooler stars within a given spectral type

1.1 A- and late B stars: a peculiar lot

Approximately 10% of main sequence A and late B stars, ranging in effective temperatures from about 7000 to 15000 K, exhibit peculiarities in their spectra (Landstreet et al., 2007). The degree of peculiarity is seemingly correlated to the physical parameters of the star, namely effective temperature, gravity and the presence of magnetic fields. The spectral anomalies vary from the non-magnetic Am and HgMn stars to the magnetic Ap/Bp stars. However, before one can discuss the middle main sequence (A and late B) chemically peculiar stars, a definition of what constitutes a "normal" star must be established. For the purposes of this discussion, we shall consider a normal star as one that has an atmospheric chemical composition comparable to the Sun and does not possess a detectable magnetic field. In this section, we briefly review the various types of chemical peculiarities found in A and late B stars.

1.1.1 Non-magnetic stars

Am stars

Am, or metallic-line, stars reside on the main sequence and range in effective temperature from about 7000 - 10000 K. The atmospheric chemical peculiarities they exhibit are generally mild, rarely more than a factor of 10 different than solar. Am stars can be slightly overabundant in Fe-peak elements, as well as Zn and Sr; however, lighter elements, such as Ca, Mg, and Sc, are underabundant (Preston, 1974).

Am stars are slow rotators (Richard et al., 2004), with projected rotational velocities $v \sin i$ generally less than about 40 km s^{-1}, which is considerably less than their normal counterparts with $v \sin i$'s of order 120 km s^{-1}. Their frequency of close binaries is considerably higher than for normal stars, with periods that range from about 2 to 100 days (Abt & Levy, 1985). It is this binarity frequency that is often attributed to an Am star's slow rotation, which may be the result of tidal braking due to close binary interactions. Am stars do not posses strong, ordered magnetic fields (Fossati et al., 2007). An example of an Am star is Sirius A (see Landstreet, 2011).

HgMn stars

As the name suggests, HgMn stars are overabundant in Hg and Mn, by as much as 1000 and 100 times the solar values, respectively. Further to this, they are He underabundant and Cr overabundant. They range in effective temperature from about 11000 - 16000 K (early A and late B stars), and in many respects are the higher mass counterparts to the Am stars (Abt et al.,
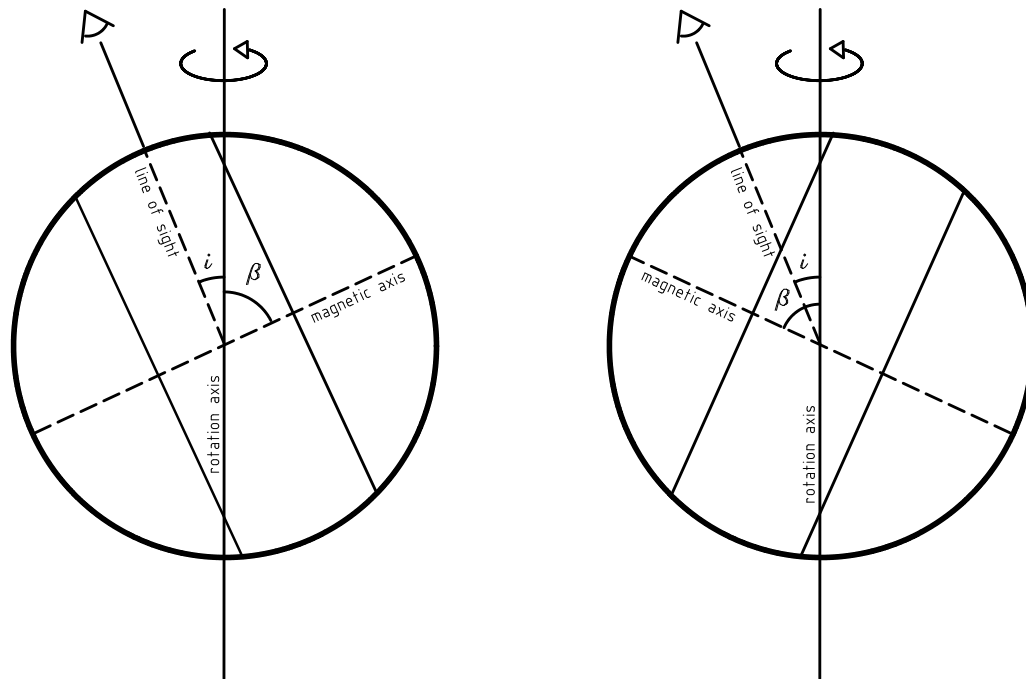
Figure 1.2: The geometry for HD 318107 borrowed from Bailey et al. (2011). The angles between the rotation axis (vertical line) and the line-of-sight and magnetic field axes are $i = 22°$ and $\beta = 65°$, respectively. The left panel depicts an orientation where the magnetic axis is farthest from the line of sight and the right panel when the magnetic axis is nearer alignment with the line of sight.

2002). HgMn stars are also slow rotators and are mostly found in spectroscopic binary systems. They have no detectable large scale magnetic fields.

1.1.2   Magnetic stars

Ap/Bp stars

The magnetic peculiar A (Ap) and B (Bp) stars are characterised by having weak He lines and therefore often clumped as one group: the Ap stars. This lack of distinction stems from the spectral classification of stars, where A stars show no He-absorption lines, which is a characteristic of the magnetic Ap/Bp stars. In principle, the magnetic Ap stars range in effective temperature from about 7000 to 10000 K, with masses between about 1.5 to 2.5 $M_\odot$, whereas

the magnetic Bp stars range in effective temperature and mass from about 10000 to 15000 K
and 2.5 to 5 M$_\odot$, respectively. It is important to note that this thesis mainly focuses on the mag-
netic Bp stars; however, little effort will be made to distinguish between the magnetic Ap and
Bp stars (often times being used interchangeably). As a group, the Ap/Bp have three defining
characteristics:

1. Large, global magnetic fields with strengths of the order of 1 kG or more.

2. Anomalous atmospheric abundances, notably for He, Si, Fe-peak and rare-earth ele-
   ments.

3. Substantially slower rotation than their normal counterparts, with typical values of order
   50 km s^{-1} or less.

The magnetic fields of Ap stars are well-ordered and roughly dipolar in nature. The origin
of the field is unknown but is most likely a fossil field retained from the star formation process.
In the most extreme cases, the surface field $\langle B \rangle$ is of the order of 30 kG in strength (e.g.
Babcock's star; see Babcock, 1960). All Bp stars are He-weak with observed underabundances
compared to the Sun. For Ap stars, the abundance of He is unknown, although upper limits are
possible, that suggest values of order 10 to 100 times less than in the Sun (Ryabchikova, 1991).
Heavier elements such as the Fe-peak and rare-earth elements are overabundant. For example,
Cr can be as much as 100 times and Pr and Nd of the order of 10^4 times the solar ratios,
respectively. Moreover, the distribution of these elements on the stellar surface is "patchy"
because the magnetic field quenches any convective motions and prevents horizontal mixing.

Ap stars rotate at roughly 10% the rate of main sequence stars of similar mass, with typical
rotation periods of a few days, but can vary from less than about 1 day to decades (Mathys
& Hubrig, 1997). As the star rotates, we detect changes in light, spectra and magnetic field
strengths that vary with the rotation period of the star. This variability is best explained using
the oblique rigid rotator model: the line-of-sight and magnetic field axes are inclined at angles
i and β to the rotation axis, respectively. An example of this geometry for the magnetic Ap star
HD 318107 is provided in Figure 1.2, with $i = 22°$ and $\beta = 65°$. In this figure, as the star rotates,
distinct portions of the magnetic field and stellar surface are observed. Within this model, the
variations are a direct result of the the inhomogeneous distribution of elements over the stellar
surface as the star rotates. Light variations are caused by changes in the photospheric opacities
that are a result of the "patchy" abundance distributions. Since the field structure is roughly
dipolar, the line-of-sight magnetic field strength $\langle B_z \rangle$ is also modulated with the rotation period,
with often a sinusoidal variation. The inhomogeneous distribution of elements is attributed to

the magnetic field, which therefore produces the spectral line variability. The correlation of these variabilities with the rotation period provide the strongest observational support for the oblique rigid rotator model.

1.2   Diffusion processes

The extensive range of chemical peculiarities in cluster A and late B stars argues against the point that the anomalies are the result of the environment from where they formed. In fact, the bulk chemistries of these stars do not differ significantly from the interstellar medium (ISM). Therefore, the peculiarities must be the result of a process (or processes) within the stellar interior and/or atmosphere. The most probable mechanism that creates the observed atmospheric chemical peculiarities is *chemical diffusion*. Diffusion was first postulated by Michaud (1970), suggesting that the competition between gravitational settling and radiative levitation causes trace elements to migrate into and out of the stellar atmosphere. A and late B stars are the perfect laboratory for diffusion processes to occur because they lack deep convective zones.

Consider a box of atoms that consists of all H except for one atom of Fe. Under the influence of no external forces, the atoms will collide and support one another, with no net upward or downward diffusion. Now suppose the box is placed in a gravitational field. The only significant difference between an atom of H and Fe is mass. Therefore, the Fe atom will diffuse downwards in the sea of hydrogen. The box is now removed from the gravitational field and placed in a radiation field, being bombarded by photons from below. Let's further assume that the photons have a specific energy that is equal to the proper excitation or ionisation potential of the Fe atom. What will happen to the Fe atom? The photons will be absorbed and impart an upward radiative force, causing the Fe to diffuse upward.

Finally, consider both effects acting contemporaneously on any trace element, as is the case in a star. Further suppose that, below the atmosphere, a trace atomic species undergoes an upward radiative acceleration g_{rad}. If this acceleration exceeds the local gravitational acceleration g (i.e. $g_{rad} > g$), then this species will diffuse into the atmosphere. The amount of radiative acceleration imparted to an atomic species depends upon the particular situation. For strong resonance lines, the acceleration per ion decreases with increasing abundance because of saturation (i.e. a reduction in the overall flux that provides radiative support). For weak line support, the net upward acceleration does not decrease with abundance. Thus, a situation where g_{rad} decreases with height in the atmosphere would allow a specific species to accumulate. This could be the case for a species with saturated lines, where the high local abundance in the atmosphere reduces the radiative acceleration such that $g_{rad} = g$. If g_{rad} does not decrease substantially in the atmosphere, a species can be lost from the top of the atmosphere to space.

Alternatively, if the local gravity exceeds the radiative acceleration (i.e. $g > g_{rad}$), then the species will sink below the atmosphere.

It's now easily understood that, in general, when a given species has a net upward acceleration that chemical overabundances in the atmosphere may exist, whereas those species with a net downward acceleration will be underabundant. This mechanism has been shown to be sufficient to explain the observed abundance anomalies (e.g. Michaud et al., 1976; Alecian et al., 2011). The presence of a magnetic field influences the effects of diffusion. For instance, when the magnetic field lines are vertical, ions are able to diffuse readily along the field. However, when the field lines are horizontal, ions are trapped. This naturally explains the horizontal inhomogeneities of chemical abundances in the atmospheres of Ap stars discussed in Section 1.1.2. For example, the energy density ($B^2/8\pi$) in a magnetic field of order 10^3 G (typical for an Ap star) is at least of order 10^4 ergs cm^{-3}. Compare this to the energy density due to thermal motions ($\propto nkT$) for a temperature of about 10000 K and a typical atmospheric number density n of order 10^{14} cm^{-3} (recall that Boltzmann's constant is of order 10^{-16} ergs K^{-1}), which is of order 10^2 ergs cm^{-3}. The magnetic field is therefore more than sufficient to quench any turbulent atmospheric motions, allowing for horizontal abundance anomalies to form. Diffusion processes can also create the vertical stratification that is observed in the atmospheres of both magnetic and non-magnetic A and late-B stars (e.g. Ryabchikova et al., 2001). Vertical stratification and diffusion are discussed in greater detail in Chapters 4 and 5, respectively.

1.3 Nature of magnetic fields in A- and B-type stars

1.3.1 Origin

In principle, the generation of the magnetic field of the Sun (and solar-like stars) is a process attributed to electrical currents moving through the solar plasma. Within the outer convective region, the conducting plasma rises and falls due to a super-adiabatic temperature gradient. The differential rotation of the Sun essentially converts a simple dipolar magnetic field to a much more complex toroidal field, where the magnetic field lines are wrapped around the Sun. Furthermore, the turbulent motions in the convective zone drags in and twists the magnetic field lines, creating localised spots of stronger fields. This process, known as the solar dynamo, creates a magnetic field that is spatially non-uniform and inherently variable, changing rapidly on relatively short time-scales (evident in the breaking of these twisted flux lines creating solar flares and re-connection events).

The magnetic fields observed in Ap/Bp stars are static for as long as fields of this nature have been detected (the first such field was a 1.5 kG field in 78 Vir in 1947, see Babcock,

1947). Therefore, the stellar dynamo field is not a feasible explanation. Another possibility is that these fields are fossils, which are retained from the star formation process (see Mestel & Landstreet, 2005). It is still not understood where these fossil fields originate. The leading hypothesis is that the magnetic field originates from the interstellar medium and, as a molecular cloud collapses to form stars, that these magnetic field lines are swept in, retained, and amplified as the star contracts towards the main sequence. Another possibility is that the fields are retained from a dynamo produced during the pre-main sequence evolution of these stars, when the proto-star traverses a fully convective phase as it contracts towards the main sequence.

The fossil field is a very attractive solution. If we start from a weak magnetic field (of the order of 1 μG, which is typical of the interstellar medium) and require that magnetic flux ($\phi = \pi R^2 B$) be conserved, a main sequence stars can easily expect to have field strengths of the order of a kG or more. In fact, the field should be of the order of 10^8 G (note that a proto-star will contract by a factor of order 10^7 as it evolves towards the main sequence), meaning that a substantial fraction of the magnetic flux must be dissipated during the pre-main sequence phase. Further, the fossil field aids in braking the star during the star formation process, possibly allowing the transfer of angular momentum to the stellar wind (Stepien, 2000). This may explain the slower rotation observed in Ap/Bp stars compared to "normal" stars of similar mass.

Even though the fossil field is an appealing option, it raises the question as to why less than about 10% of main sequence A and B stars are magnetic. What mechanism(s) is/are responsible for the retention (or lack thereof) of these fossil fields?

1.3.2   Main sequence evolution

Until recently, little was known about how the magnetic fields of Ap/Bp stars may evolve during their main sequence lifetimes. Studying Ap/Bp stars that are members of open clusters or associations offers a laboratory to study this time evolution, since they can have accurately determined ages. A spectropolarimetric[4] survey of cluster magnetic Ap/Bp stars suggests that magnetic field strengths decline sharply with age for stars between 2 - 5 M$_\odot$ (see Bagnulo et al., 2006; Landstreet et al., 2007, 2008). In general, the less massive stars retain larger fields (greater than about 1 kG) for a larger fraction of their main sequence lifetime than do the more massive ones, but all Ap/Bp stars, regardless of age, will have fields greater than order 10^2 G. This result provides the first observational evidence that these fossil fields are stable enough to persist throughout the main sequence.

---

[4]Spectropolarimetry is the measurement of polarised light as a function of wavelength. As will be shown in the subsequent section, the simultaneous acquisition of the intensity and circular polarisation spectrum allows for the measurement of the surface and line-of-sight magnetic fields, respectively.

1.4 Measurement of magnetic fields in stars

1.4.1 Basic Physics

Consider an atom with one valence electron that is placed in an external magnetic field. The energy levels of this atom will be split into several $(2J + 1)$ components due to the interaction energy of the spin and angular momentum (orbit) of the electron. This atom will have a total magnetic dipole moment μ that is the sum of its orbital and spin components (μ_l and μ_s). The interaction energy between the split components can then be easily understood,

$$\Delta E = -\mu \cdot \mathbf{B}, \tag{1.6}$$

where $\mathbf{B}$ is the external magnetic field and $\mu = \frac{g\mu_B \mathbf{J}}{\hbar}$. Here, μ_B is the Bohr magneton ($\mu_B = \frac{e\hbar}{2m_e c}$), g is the Landé factor (a number of order 1) and $\mathbf{J}$ is the total angular momentum (in the case of L-S coupling, the total angular momentum can be expressed as the sum of the orbital angular momentum L and spin angular momentum S). The change in energy between the atomic states can then be written as

$$\Delta E = \mu_B g m_J B, \tag{1.7}$$

where m_J is the magnetic quantum number ($-J \leq m_J \leq +J$).

From Equation 1.7, we recognise that a single atomic level will be split into $2J + 1$ Zeeman components. The magnitude of the splitting will be different for each energy level depending on the Landé g factor. The allowed transitions are determined by the selection rules. In the case of L-S coupling, they state that $\Delta L = \pm 1$ and $\Delta m_J = 0, \pm 1$. The lines resulting from a transition with $\Delta m_J = 0$ are called pi components and are spread symmetrically about the line centre $\lambda_\circ$ in the absence of a magnetic field. The lines resulting from a transition with $\Delta m_J = \pm 1$ are the sigma components. These lines are red and blue shifted with respect to $\lambda_\circ$. Transitions between the sub-levels from a higher energy state to a lower energy state produce the observed lines. Utilising equation 1.7, the wavelength separation between the sigma and pi components can be derived:

$$\Delta\lambda(\text{Å}) = \frac{e}{4\pi m_e c^2}\lambda_0^2 B\bar{z} = 4.67 \times 10^{-13}\lambda_0^2 B\bar{z}, \tag{1.8}$$

where λ_o is the position of the unsplit line in Å, B is the magnetic field strength in Gauss, and $\bar{z}$ is the effective Landé factor of the transition. For example, a typical Fe II transition at 6149 Å ($\bar{z} = 1.35$) will be split by about 0.24 Å in a 10 kG field.
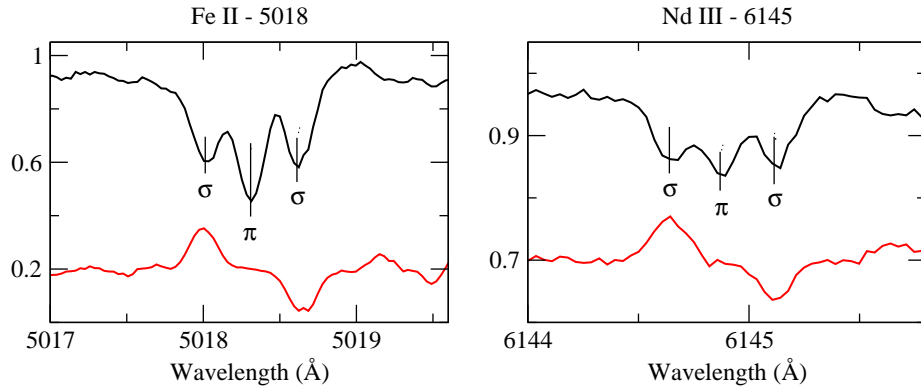
Figure 1.3: Two examples of Zeeman components for lines of Fe II and Nd III in the magnetic Ap star HD 318107. Shown are the observed intensity spectra in black and the Stokes V (circular polarisation) across the lines, vertically translated for easy viewing, in red.

Polarisation of Zeeman components

Magnetic fields also cause the Zeeman components of a spectral line to have specific polarisation properties that depend upon the orientation of the magnetic field to the line-of-sight (the direction from which the light is emitted). Emitted light can either be linearly or circularly polarised, based upon the orientation of the magnetic field. For lines in absorption, linear polarisation occurs when the magnetic field is perpendicular to the line-of-sight. In this case, the pi and sigma components are linearly polarised perpendicular and parallel to the field direction, respectively. This idealised case occurs when the line-of-sight is directly aligned to the magnetic equator of a star. Circular polarisation occurs when the magnetic field has a net component parallel to the line-of-sight. In this case, the pi components will vanish and the sigma components will be circularly polarized with the $\Delta m_J = +1$ and -1 being polarised in the opposite sense. Figure 1.3 presents a typical example of Zeeman split components and circular polarisation across spectral lines for HD 318107, a magnetic Ap stars with a line-of-sight magnetic field strength of the order of 5 kG.

1.4.2   Detecting magnetism in stars

Direct measurement of the surface magnetic field $\langle B \rangle$ can be done when spectral lines are clearly split into their respective Zeeman components via Equation 1.8. However, the detection of Zeeman splitting is not very common in stellar spectra, where often the rotation of the star smears out the individual Zeeman components. As a rough approximation, the surface field in

kG must be about twice the projected rotation velocity $v \sin i$ in km s^{-1} in order to successfully measure $\langle B \rangle$.

Polarisation can be a powerful tool for detecting magnetic fields in stars. As opposed to $\langle B \rangle$, the line-of-sight field $\langle B_z \rangle$ requires polarisation spectra of both left and right circularly polarised light in order to determine the Stokes V parameter.

One method involves measuring the circular polarisation in the wings of a broad Balmer line, such as Hβ (see Landstreet, 1982; Bagnulo et al., 2002). In this case, the circular polarisation V and the line profile $I(\lambda)$ can be measured and $\Delta\lambda$ computed. Then, an estimate of $\langle B_z \rangle$ can be made using Equation 1.8. We refer the reader to Landstreet et al. (2009) where a simple explanation of this technique is provided.

Another method, called Least Squares Deconvolution (LSD), involves measuring $\langle B_z \rangle$ directly from the Stokes V profiles (see Donati et al., 1997). In this method, all metallic and He line profiles are assumed to have the same shape and are averaged together into one mean Stokes profile of both I and V, with each line weighted by depth and Landé splitting factor. Essentially, this allows for stronger lines and lines affected more by the magnetic field to be assigned a larger contribution towards the average profile. We then measure the magnetic field from the averaged Stokes V profile with the added advantage of a significantly increased signal-to-noise ratio (SNR), making it possible to detect weaker magnetic fields. Specifically, the line-of-sight magnetic field is computed from the first-order moment of the Stokes V profile:

$$\langle B_z \rangle = -2.14 \times 10^{12} \frac{\int v V(v) \mathrm{d}v}{\lambda z c \int [I_{\mathrm{c}} - I(v)] \, \mathrm{d}v}, \tag{1.9}$$

where $\langle B_z \rangle$ is measured in Gauss, λ is the mean wavelength of the mean Stokes profile in Å, z is the mean Landé factor and v is velocity in km s^{-1}. A more detailed description of this method is discussed, for example, by Donati et al. (1997), Wade et al (2000) and Landstreet et al. (2008).

1.5   Spectral line formation

An adequate explanation of spectral line formation requires the ability to track the path that a photon will take in the stellar atmosphere. This is achieved using the *equation of radiative transfer*, which is discussed in the following section.
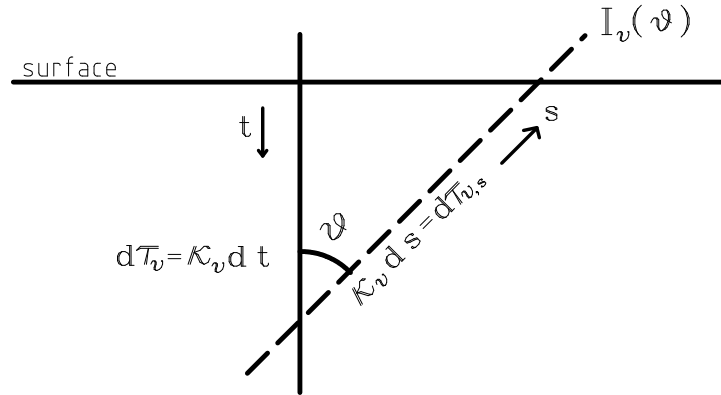
Figure 1.4: This is the geometry used to solve the transfer equation. It shows the relation between the radiation leaving the surface at an angle θ to the normal and the optical depth $\tau_{\nu,s}$ along s.

1.5.1 Equation of radiative transfer

The equation of radiative transfer is most easily understood under the assumption of a purely absorbing and thermally radiating gas. Under the assumption that absorption occurs throughout the atmosphere of a star, and ignoring scattering processes, one can model the basic physics of stellar line formation. To begin, assume a plane parallel atmosphere (a good approximation for a star where the depth of the atmosphere is a tiny fraction of the stellar radius). Figure 1.4 outlines the geometry in the atmosphere of a star. Consider radiation emitted from the star, passing through the atmosphere at an angle θ. The intensity of radiation $I_\nu(\theta)$ at a given frequency ν passes along the vector s. As per the equation of radiative transfer, some radiation will be absorbed and emitted along path s, but not lost due to scattering processes:

$$\frac{dI_\nu(\theta)}{ds} = -\kappa_\nu I_\nu(\theta) + \epsilon_\nu. \tag{1.10}$$

Absorption of radiation along path s is taken into account by the opacity coefficient, κ_ν (cm^{-1}), where the emissivity, ϵ_ν, is the amount of radiation being emitted (ergs cm^{-3} s^{-1} Hz^{-1} ster^{-1}). In principle, if $dI_\nu/ds > 0$ the intensity of radiation increases along the vector s with $\epsilon_\nu > \kappa_\nu I_\nu$. This produces an emission spectrum. If $dI_\nu/ds < 0$, meaning that $\epsilon_\nu < \kappa_\nu I_\nu$, there is a loss of intensity along the path s, which produces absorption features in a spectrum.

Noting that $d\tau_{\nu,s} = \kappa_\nu ds$ and $\cos(\theta) = -d\tau_\nu/d\tau_{\nu,s}$ one can show that the angular dependence

of the equation of radiative transfer is

$$\cos(\theta)\frac{dI_\nu(\theta)}{d\tau_\nu} = I_\nu(\theta) - S_\nu, \tag{1.11}$$

where S_ν is the source function and is defined as ϵ_ν/κ_ν (the emissivity divided by the opacity coefficient). Solving this differential equation, one can obtain the surface intensity and find that

$$I_\nu(0, \theta) = \int_0^\infty S_\nu(\tau_\nu)e^{-\tau_\nu \sec \theta}d(\tau_\nu \sec \theta). \tag{1.12}$$

This equation can be easily understood. The optical depth along s is $d(\tau_\nu \sec \theta)$ and $S_\nu e^{-\tau_\nu \sec \theta}d(\tau_\nu \sec \theta)$ is the fraction of radiation that reaches the surface of the star. One can obtain an explicit solution by assuming a linear source function,

$$S_\nu = a_\nu + b_\nu \tau_{\text{cont}}, \tag{1.13}$$

where a_ν and b_ν are taken as constants (that in principle would depend upon the choice of frequency) and τ_{cont} is the continuum optical depth. Further, local thermodynamic equilibrium (LTE) is assumed so that $S_\nu = B_\nu$, where B_ν is the Planck function (black body radiation). The assumption of LTE is a good approximation, regardless of the fact that energy is lost at the surface of the star. This is due to the fact that the mean free path of the radiation is small compared to the size scale of the region under consideration. Defining $\mu = \cos \theta$, $S_o = a_\nu$, and $\beta = b_\nu/a_\nu$ and solving Equation 1.12 one finds that

$$I_{\text{cont}}(\theta) = S_o(1 + \beta\mu) = S_{\text{cont}}(\tau_{\text{cont}} = \mu). \tag{1.14}$$

This is a very powerful equation. For a given source function, one has the emerging specific intensity at varying inclinations μ to the vertical. Notice that the emergent specific intensity depends upon the choice of frequency and the angle. As a simple example, consider limb darkening in the Sun. At the centre of the Sun, where $\theta = 0$, I_{cont} is maximum whereas at the edge of the Sun ($\theta = 90°$) I_{cont} is minimum.

1.5.2   Spectral Lines

We know that $\kappa_\nu = \kappa_{\text{cont}} + \kappa_{\text{line}}$, where the total opacity is the sum of the continuum opacity and the opacity in the spectral line. Defining η_ν to be $\kappa_{\text{line}}/\kappa_{\text{cont}} = $ constant one can express the opacity at a given frequency as,

$$\kappa_\nu = (1 + \eta_\nu)\kappa_{\text{cont}}. \tag{1.15}$$

Here, η_ν describes the line profile. For $\kappa_{\text{line}} \ll \kappa_{\text{cont}}$, the opacity in the line is small compared to that of the continuum and only weak lines (if any) are observed. Conversely, for $\kappa_{\text{line}} > \kappa_{\text{cont}}$ the absorption features are substantially stronger than that of the continuum; stronger lines are observed. Assuming that η_ν is independent of depth in the atmosphere (the Milne-Eddington approximation), one can rewrite Equation 1.15, recalling that $\tau_\nu = \kappa_\nu s$:

$$\tau_\nu = (1 + \eta_\nu)\tau_{\text{cont}}, \tag{1.16}$$

with η_ν now equally $\tau_{\text{line}}/\tau_{\text{cont}}$. Modifying Equation 1.13, the source function now becomes

$$S_\nu(\tau_\nu) = S_o(1 + \frac{\beta\tau_\nu}{1 + \eta_\nu}). \tag{1.17}$$

Simply solving Equation 1.12 for this new source function yields a new expression for the surface intensity:

$$I_\nu(0) = S_o(1 + \frac{\beta\mu}{1 + \eta_\nu}). \tag{1.18}$$

This expression (which applies locally to a point on the stellar surface) describes the specific intensity that is emergent throughout a spectral line. At line centre, notice that $\eta_\nu \gg 1$ (ie. $\tau_{\text{line}} \gg \tau_{\text{cont}}$); the intensity in the line decreases to create a larger absorption feature because of the larger line opacities. Nearer the wings, the opacity drops off and the intensity increases in the line.

Absorption Features

The creation of absorption lines requires a temperature gradient. In stars, this gradient is created with the cooler atmosphere. Specifically, absorption features are due to bound electrons in a certain energy state absorbing a photon of energy $h\nu$ and jumping to a higher energy level. The absorption feature will occur at frequency ν, but can only occur if there is an energy level to jump to such that $E_f = E_i + h\nu$. However, the physics is more complicated: What broadens a spectral line? What determines line depth?

Photons coming into the atmosphere encounter atoms moving at different velocities. These thermal motions allow photons of slightly different energies to be absorbed and contribute locally to the line. Away from line centre, a photon that is slightly shifted in wavelength ($\lambda \pm \Delta\lambda$) will see an optically thin medium for a longer distance in the line-forming region than it would otherwise without the thermal motions of the atom, which means that the photon will not be absorbed immediately. This serves to broaden the spectral line around the wavelength, λ. This is referred to as thermal broadening. Other local broadening effects include microturbulence

and magnetic fields. Microturbulence is characterised by small-scale motions in the stellar atmosphere that are characterised by a Gaussian velocity distribution. Analogous to thermal broadening, the microturbulent velocities produce Doppler shifts that broaden spectral lines. The broadening of spectral lines due to magnetic fields can be seen following the discussion of Section 1.4 (see Equation 1.8). Stellar rotation is a non-localised effect that broadens spectral lines. The rotation of the star creates blue and red-shifted components (as portions of the star moves toward and away from the observer, respectively). The spectral lines necessarily broaden proportional to the rotation velocity of the star. This is often the dominant form of spectral line broadening in a star.

The strength of a spectral line is a function of the depth in the atmosphere from which the line was formed. Stronger lines form at shallower depths whereas weaker lines form at deeper depths. This can easily be seen from Equation 1.18. The emergent specific intensity is described completely by η_ν. For $\eta_\nu \ll 1$ (optically thin case) the line depth is proportional to the total number of absorbing atoms. This creates weak spectral lines. As η_ν approaches 1 or becomes much greater than 1 (optically thick case) the line strengths necessarily increase. As per Equation 1.18, the line centre has the lowest intensity when $\eta_\nu \gg 1$ where $I_\nu(0) = S_o = S_\nu(0) = B_\nu(0)$ for LTE. In the wings, the line is still optically thin. The line depth increases with η_ν, which increases the line width causing the line profile to broaden: with increasing η_ν, the profile is first Gaussian, becoming more rectangular and eventually Lorentzian in shape.

1.5.3   Polarisation and the equations of radiative transfer

In the presence of polarised light, the equation of radiative transfer has to be modified from the above discussion. We describe polarised light using the Stokes' parameters: I, Q, U and V. In brief, I is the total specific intensity, V is the circular polarisation (see Section 1.4) and linear polarisation is described by Q and U. Specifically, $V = I_{\text{right}} - I_{\text{left}}$, measuring the intensity of light beams through two circular polarisers, one of which allows only right circularly polarised light and the other only left circularly polarised light. Similarly, linear polarisation is measured using a linear polariser that only allows light linearly polarised at a certain angle to be transmitted, while blocking the orthogonal polarisation. Specifically, $Q = I_0 - I_{90}$ (comparing light linearly polarised at 0° to 90°), whereas $U = I_{45} - I_{135}$ (comparing linearly polarised light at 45° to 135°). In general, all of the Stokes quantities are functions of frequency.

We now present the equations of radiative transfer for polarised light, without proof (see

Stenflo, 1994, for a more complete discussion):

$$
\begin{aligned}
\mu \frac{dI}{d\tau_\nu} &= \eta_I(I - B_\nu) + \eta_Q Q + \eta_V V \\
\mu \frac{dQ}{d\tau_\nu} &= \eta_Q(I - B_\nu) + \eta_I Q + \rho_R U \\
\mu \frac{dU}{d\tau_\nu} &= \rho_R Q + \eta_I U - \rho_W V \\
\mu \frac{dV}{d\tau_\nu} &= \eta_V(I - B_\nu) + \rho_W U + \eta_I V.
\end{aligned}
\tag{1.19}
$$

In the above equations, η_Q and η_V are the ratios of the Zeeman opacities, which allow us to follow the linear and circular polarisation in a given light ray. The variables ρ_R and ρ_W describe the anomalous dispersion. The equations of radiative transfer are now much more complicated and involve solving four coupled, linear, first order differential equations (see Martin & Wickramasinghe, 1979, for solution methods).

1.6 Spectrum Synthesis

The main focus of this thesis will be on performing spectrum synthesis of magnetic Ap/Bp stars in order to derive accurate atmospheric chemical abundances using the FORTRAN program ZEEMAN. ZEEMAN was developed in the mid-1980's by John Landstreet with the intent of providing a first approximation to the magnetic field and abundance distributions of magnetic Ap stars to compare with diffusion theory (Landstreet, 1988). Originally, the program neglected anomalous dispersion, but the most recent incarnation (see Wade et al., 2001) adds this effect because it has been shown that its proper treatment is crucial to reproduce accurately all four Stokes parameters, even the unpolarised parameter I.

In this section, we briefly describe the spectrum synthesis program ZEEMAN with focus on its capabilities as opposed to its inner workings. A more detailed description of how the code works is documented by Landstreet (1988), Landstreet et al. (1989) and Wade et al. (2001).

1.6.1 Computing emergent spectra with ZEEMAN

Landstreet et al. (2009) outline an accurate qualitative description of how ZEEMAN computes an emergent spectrum, which we will endeavour to summarise succinctly. At its heart, ZEEMAN numerically solves the equations of radiative transfer (Equations 1.19) under the assumption of LTE, a non-trivial exercise, using a method proposed by Martin & Wickramasinghe (1979). The program requires as input an appropriate T_{eff} and $\log g$ (usually derived from photometry)

in order to obtain a suitable model atmosphere, which is interpolated from a pre-tabulated grid of ATLAS 9 models that assume a plane-parallel atmospheric structure. The four equations of radiative transfer are then solved on a grid with 0.01 Å spacing (Landstreet et al., 2009). Accurate atomic data are taken from the VALD database (Piskunov et al., 1995; Ryabchikova et al., 1997; Kupka et al., 1999) and provide the appropriate spectral linelists with precise wavelengths, gf values, Landé factors and excitation potentials to compute local line profiles assuming a Voigt profile. Zeeman patterns are computed using tabular Landé splitting factors or assuming L-S coupling. Line blending is dealt with by adding the necessary polarised line opacities prior to solving the equations of radiative transfer.

A simple magnetic field structure is assumed that consists of colinear dipole, quadrupole and octupole components with the angles of the rotation axis to the line-of-sight i and the magnetic field axis to the rotation axis β specified. To describe the abundance variations over the stellar surface, ZEEMAN allows up to six rings, with equal spans in co-latitude, that are axisymmetric to the magnetic field axis. Within each ring, the abundance for each element is assumed uniform. This provides only a coarse description of the true abundance variations on the surface of magnetic Ap/Bp stars, but provides a useful first step to describe the physical conditions and atmospheric chemical abundances of these stars.

Once the appropriate fundamental parameters of the star are set, the program compares the computed spectrum to an observed one and chooses the best-fit model from a reduced χ^2 analysis. The fit can further be optimised by iteratively searching for the best-fit abundance, or abundance distribution, in the desired spectral window for one element at a time. ZEEMAN also provides the best fit projected rotational velocity $v \sin i$ and radial velocity v_R.

Illustrative examples

ZEEMAN was designed to model magnetic stars, but it works well for non-magnetic stars (e.g. Landstreet, 2011). For such fits, accurate values of T_eff, $\log g$, $v \sin i$, radial velocity, and microturbulent velocity are necessary. An example of a synthetic fit to the non-magnetic star HD 22136 is shown in Figure 1.5. The abundances for the Fe-peak elements of Ti, Cr, and Fe are roughly solar.

An example of a fit to the magnetic star HD 318107 is shown in Figure 1.6. This star has large line-of-sight and surface magnetic field strengths of the order of 5 and 15 kG, respectively (Bailey et al., 2011). To illustrate the enhanced Fe-peak and rare-earth elemental abundances of magnetic Bp stars, Figure 1.6 offers a comparison of two model fits with the enhanced abundances of Bailey et al. (2011) and solar abundance ratios. The figure clearly shows magnetically split spectral lines as well as the necessity for Fe-peak elements of the order of 100 times the solar ratio to satisfactorily model the observed spectrum. The obvious residual
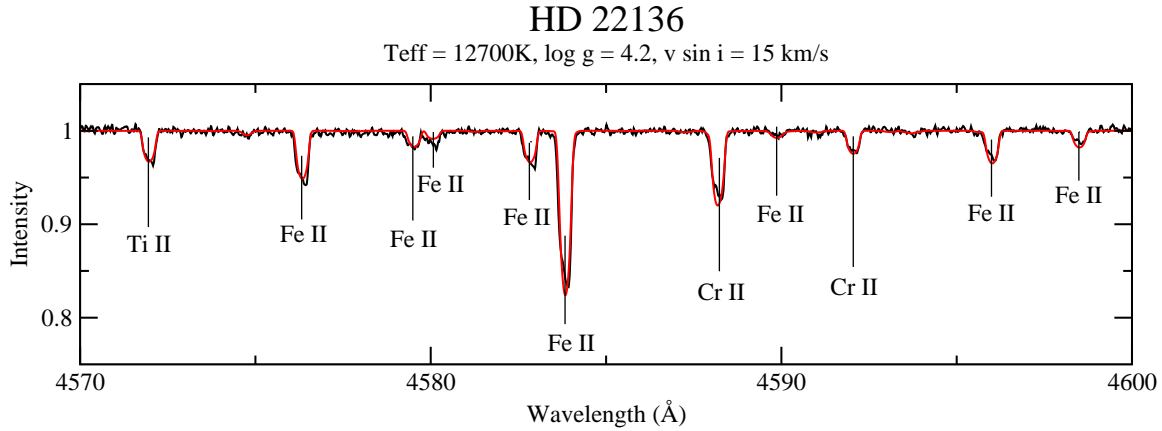
Figure 1.5: An example of a model fit for the normal, non-magnetic B-type star HD 22316. The observed spectrum is in black and the synthetic spectrum in red.
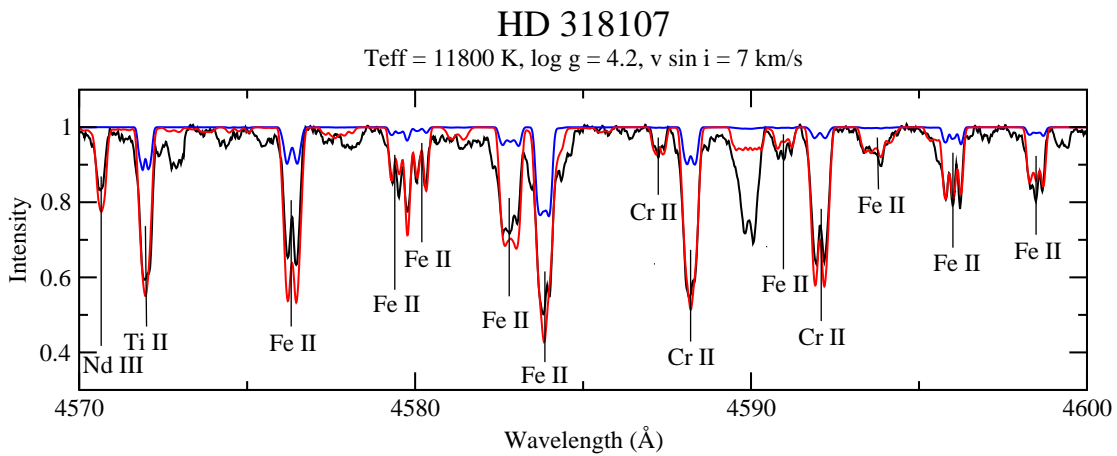
Figure 1.6: An example of a model fit for the magnetic Bp star HD 318107. The observed spectrum is in black, a solar abundance model is in blue and the fit in red assumes the enhanced Fe-peak and rare-earth abundances from Bailey et al. (2011).

differences between the observed and computed spectra are likely due to vertical stratification of elements in the stellar atmosphere (see Chapter 4). In addition, this star is about 10^5 times more abundant in rare-earth elements than the Sun, which is highlighted by the presence of Nd III at 4571 Å.

1.7 Abundance analysis of magnetic Bp stars

The main focus of this thesis is in performing abundance analyses of magnetic Bp stars using the fortran program ZEEMAN. In chapters 2 and 3, detailed models of the magnetic Bp stars HD 133880 and HD 147010 are described, which include models of their magnetic field geometries and chemical abundance distributions based on spectropolarimetric observations from the Canada-France-Hawaii Telescope's (CFHT) ESPaDOnS spectropolarimeter. Chapter 4 investigates the discrepancy between abundances derived from Si II and Si III in late B-type stars. We report abundances derived from the two ionisation states of silicon for normal, HgMn and magnetic Bp stars ranging in effective temperature from about 10500 to 15000 K in an effort to determine regularities in the phenomenon. We attempt to explain this discordance in terms of vertical stratification in the atmospheres of these stars. In chapter 5, we present a comprehensive study of the atmospheric chemical abundances of a sample of 15 magnetic Bp stars, with mass 3.5±0.5 M$_\odot$, that are members of open clusters, and thus have well-known ages. We characterise trends with stellar age in the atmospheric abundances of these stars, providing the first observational constraints to diffusion theory on how these abundances evolve during the main sequence lifetime of these stars. Finally, chapter 6 summarises the work presented and suggests future avenues to expand upon this research.

Bibliography

Abt H. A. & Levy S. G., 1985, ApJS, 59, 229

Abt, H. A., Levato, H., & Grosso, M. 2002, ApJ, 573, 359

Alecian E. et al., 2009, in EAS Publications Series, Vol. 39, EAS Publications Series, C. Neiner & J.-P. Zahn, ed., pp. 121–132

Alecian G., Stift M. J., Dorfi E. A. 2011, MNRAS, 418, 997

Babcock H. W., 1947, ApJ, 105, 105B

Babcock H. W., 1960, ApJ, 132, 521

Bagnulo S., Szeifert T., Wade G. A., Landstreet J. D., Mathys G., 2002, A&A, 389, 191

Bagnulo S., Landstreet J. D., Mason E., Andretta V., Silaj J., Wade G. A., 2006, A&A, 450, 777

Bailey J. D., Landstreet J. D., Bagnulo S., Fossati L., Kochukhov O., Paladini C., Silvester J., Wade G., 2011, A&A, 535, A25

Bailey, J. D. & Landstreet, J. D. 2013b, A&A, 551, A30

Donati J.-F., Semel M., Carter B. D., Rees D. E., Collier Cameron A., 1997, MNRAS, 291, 658

Fossati, L., Bagnulo, S., Monier, R. et al. 2007, A&A, 476, 921

Kupka, F., Piskunov, N. E., Ryabchikova, T. A., Stempels, N. C., & Weiss, W. W. 1999, A&A, 138, 119

Landstreet J. D., 1982, ApJ, 258, 639

Landstreet J. D., 1988, ApJ, 326, 967

Landstreet, J. D., Barker, P. K., Bohlender, D. A., & Jewison, M. S. 1989, ApJ, 344, 876

Landstreet, J. D. (2004). A stars as physics laboratories. In J. Zverko, J. Ziznovsky, S. J. Adelman, & W. W. Weiss, editor, *The A-Star Puzzle*, volume 224 of *IAU Symposium*, pages 423–432

Landstreet J. D., Bagnulo S., Andretta V., Fossati L., Mason E., Silaj J., Wade G. A., 2007, A&A, 470, 685

Landstreet, J. D., Silaj, J., Andretta, V., et al. 2008, A&A, 481, 465

Landstreet, J. D. (2009). Observing and Modelling Stellar Magnetic Fields 2. Models. In C. Neiner & J. -P. Zahn, editor, *Stellar Magnetism*, volume 39 of *EAS Publication Series*, pages 21–37

Landstreet, J. D. 2011, A&A, 528, A132

Mestel, L., & Landstreet, J. D. 2005, in Lecture Notes in Physics vol. 664, Cosmic Magnetic Fields, ed. R. Wielebinski, R. Beck, 183

Michaud, G. 1970, ApJ, 160, 641M

Michaud, G., Charland, Y., Vauclair, S., & Vauclair, G. 1976, ApJ, 210, 447

Martin, B. & Wickramasinghe, D. T. 1979, MNRAS, 189, 883

Mathys, G. & Hubrig, S. 1997, A&AS, 124, 475

Piskunov, N. E., Kupka, F., Ryabchikova, T. A., Weiss, W. W., & Jeffery, C. S. 1995, A&A, 112, 525

Preston, G. W. 1974, ARA&A, 12, 257

Richard, O., Talon, S., & Michaud, G. 2004, in IAU Symp. 224, The A-Star Puzzle, ed. J. Zverko, J. Ziznovsky, S. J. Adelman, & W. W. Weiss (Cambridge: Cambridge Univ. Press), 215

Ryabchikova T. A., 1991, in IAU Symposium, Vol. 145, Evolution of Stars: the Photospheric Abundance Connection, G. Michaud & A. V. Tutukov, ed., pp. 149–+

Ryabchikova, T. A., Piskunov, N. E., Kupka, F., & Weiss, W. W. 1997, Baltic Astronomy, 6, 244

Ryabchikova, T. A., Savanov, I. S., Malanushenko, V. P., & Kudryavtsev, D. O. 2001, Astron-
    omy Reports, 45, 382

Schaller, G., Schaerer, D., Meynet, G., & Maeder, A. 1992, A&A, 96, 269

Stenflo, J.-O. 1994, Solar Magnetic Fields: Polarized Radiation Diagnostics (Berlin: Springer)

Stepien, K. 2000, A&A, 353, 227

Wade, G. A., Donati, J. F., Landstreet, J. D., Shorlin, S. L. S. 2000, MNRAS, 313, 851

Wade G. A., Bagnulo S., Kochukhov O., Landstreet J. D., Piskunov N., Stift M. J. 2001, A&A,
    374, 265

Wade G. A., Drouin D., Bagnulo S., Landstreet J. D., Mason E., Silvester J., Alecian E., Böhm
    T., Bouret J.-C., Catala C., & Donati J.-F. 2005, A&A, 442, L31

Chapter 2

The rapidly rotating magnetic Bp star HD 133880

2.1   Introduction

HD 133880 (=HR 5624) is a rapidly rotating late B-type chemically peculiar (Bp) star with the Si λ4200 peculiarity. It exhibits an unusual magnetic field. The mean line-of-sight magnetic field $\langle B_z \rangle$ is very strong and observed to vary from about -4 to +2 kG (Landstreet, 1990). Unlike most chemically peculiar stars, HD 133880 has a field that is predominantly quadrupolar as opposed to dipolar. HD 133880 is a photometric variable with variations on the order of 0.15 mag in the U-band, which may be the result of the large magnetic field (Waelkens, 1985). The magnetic field serves to create a "patchy" distribution of elements on the surface of the star. This non-uniform abundance distribution, and its associated line blocking and back-warming, may explain the photometric variations (Ryabchikova, 1991). Specifically, several elements are distributed non-uniformly over the stellar surface in a non-axisymmetric pattern about the rotation axis. As the star rotates, the observed magnetic field strength $\langle B_z \rangle$ varies and over/underabundances of elements are detected. The most striking anomalous abundances in Bp stars are often found for Cr and rare-earth elements, which can be as much as 10^2 and 10^{4-5} overabundant compared to the Sun, respectively (Ryabchikova, 1991). The resultant variability is explained by the oblique rotator model: the rotation and magnetic field axes are at angles i and β to the line-of-sight and rotation axis, respectively.

Landstreet (1990) used longitudinal magnetic field measurements obtained from Hβ, in conjunction with photometric data reported by Waelkens (1985), to deduce a period of P = 0.877485 ± 0.00002 days for HD 133880. Lim, Drake & Linsky (1996) did a preliminary

---

[1]A version of this chapter is published as Bailey, J.D. et al. 2012, MNRAS, 423, 328.

analysis of the rotational modulation of 3 cm and 6 cm radio emission from HD 133880. The radio emission variation had both broad and narrow peaks that correlated with the maximum extrema of the dipolar, B_d, and quadrupolar, B_q, contributions to the magnetic field reported by Landstreet (1990), respectively.

Landstreet et al. (2007) confirmed HD 133880 as a member of the Upper Cen Lup association and thus it is a star with a well known age of $\log t = 7.20 \pm 0.10$ (yrs). HD 133880 is a very young star, having completed only about 5% of its main sequence lifetime (Landstreet et al., 2007, 2008). Their preliminary analysis of many physical characteristics concluded that $T_{\text{eff}} = 12000 \pm 500$ K, $\log L/L_\odot = 2.10 \pm 0.1$, and M/M$_\odot$ = 3.20 ± 0.15. Note that our analysis (see below) has shown that the T_{eff} is likely closer to 13000 K. Table 1 summarises the physical properties of HD 133880.

There are few hot chemically peculiar stars with broad spectral features for which abundance analyses have been carried out. Because of the very complex, strong and unusual magnetic field, HD 133880 is a worthwhile candidate to study in detail. It is also interesting from the fact that it is a star with a well known age. HD 133880 is one in a large sample of cluster Ap/Bp stars first compiled by Bagnulo et al. (2006) and Landstreet et al. (2007, 2008) to study the time evolution of magnetic fields in Ap stars. The current study is part of an effort to understand empirically how chemical abundances evolve with time and stellar age in the magnetic chemically peculiar stars. Recently Bailey et al. (2011) characterised one star in this sample, the Ap star HD 318107 (=NGC 6405 77). HD 133880 is a second star of great interest from that sample.

This chapter will discuss the efforts to characterise the magnetic field and abundance distributions of several elements for HD 133880. The following section discusses the polarimetric and spectroscopic observations used as well as the deduced longitudinal fields; Sect. 2.3 discusses improvement of the rotational period ; Sect. 2.4 describes the determination of physical parameters; Sect. 2.5 addresses the observed line profile variations; Sect. 2.6 & 2.7 discuss the magnetic field and abundance models; Sect. 2.8 reports the abundances obtained; Sect. 2.9 discusses the Hα and radio magnetosphere; and Sect. 2.10 summarises the presented work.

2.2 Observations

2.2.1 Polarised spectra

High-resolution spectropolarimetric (Stokes I and V) observations of HD 133880 were collected with ESPaDOnS at the 3.6m Canada-France-Hawaii Telescope and HARPSpol on the ESO 3.6m telescope. ESPaDOnS and HARPSpol are both high resolution fibre-fed spectropo-

Table 2.1: Summary of stellar, wind, magnetic and magnetospheric properties of HD 133880.

Spectral type	B8IVp Si $\lambda 4200$	SIMBAD & BSC
T_{eff} (K)	13000 ± 600	This thesis
$\log g$ (cgs)	4.34 ± 0.16	This thesis
$R_\star$ ($R_\odot$)	2.01 ± 0.32	This thesis
$v \sin i$ (km s^{-1})	103 ± 10	This thesis
P (d)	0.877476 ± 0.000009	This thesis
$\log(L_\star/L_\odot)$	2.02 ± 0.10	This thesis
$M_\star$ ($M_\odot$)	3.20 ± 0.15	Landstreet et al. (2007)
$\log t$ (Myr)	7.20 ± 0.10	Landstreet et al. (2007)
B_{d} (G)	-9600 ± 1000	This thesis
B_{q} (G)	-23000 ± 1000	This thesis
B_{oct} (G)	1900 ± 1000	This thesis
i (°)	55 ± 10	This thesis
β (°)	78 ± 10	This thesis
η_*	$\sim 10^7$	This thesis
W	0.3	This thesis
τ_{spin}	11 Myr	This thesis

larimeters. Three ESPaDOnS observations were obtained on August 3, 2010, and on July 14 and 15, 2011 (the latter in the context of the Magnetism in Massive Stars Large Programme (MiMeS)), and one HARPSpol spectrum was obtained on May 3, 2010. Each ESPaDOnS spectropolarimetric sequence consisted of four individual subexposures taken in different retarder configurations, whereas the HARPSpol spectrum results from the combination of four independent spectra, each comprised of four subexposures, obtained over the course of about 9 minutes. The ESPaDOnS measurements cover a spectral range from 370 nm to 1050 nm at a spectral resolution of R~65000, while the HARPSpol observation covers 370 nm to 690 nm at a spectral resolution of R~100000.

From each set of four subexposures, we derived Stokes *I* and Stokes *V* spectra following the double-ratio procedure described by Donati et al. (1997), ensuring, in particular, that all spurious signatures are removed at first order. Null polarisation spectra (labeled *N*) were calculated by combining the four subexposures in such a way that polarisation cancels out, allowing us to verify that no spurious signals are present in the data (see Donati et al. 1997 for more details on the definition of *N*). All ESPaDOnS frames were processed using the CFHT's Upena pipeline, feeding the automated reduction package Libre ESpRIT (Donati et al., 1997). The HARPSpol spectrum was reduced using the REDUCE code (Piskunov & Valenti, 2002). The details of this reduction can be found in recent papers by Makaganiuk et al. (2011) and Kochukhov et al. (2011b). The peak signal-to-noise ratios (SNRs) per 1.8 km s^{-1} velocity bin in the reduced ESPaDOnS and HARPSpol spectra range from 449-697.

The log of spectropolarimetric observations is presented in Table 2.2.

2.2.2 Unpolarised spectra

High resolution spectroscopic observations (Stokes *I*) were obtained from ESPaDOnS at CFHT and ESO's FEROS instrument at the 2.2m telescope located at La Silla. FEROS is an Échelle spectrograph that has a wavelength coverage from 350 nm to 920 nm with a spectral resolution of R~48000. FEROS is fed by two fibres (object and sky fibres), which in principle can be used to subtract the contribution of the sky from the object spectrum. A more detailed description is given by Kaufer et al. (1999). The two ESPaDOnS observations were taken on August 4 and 6, 2010, and the six FEROS spectra were collected on February 5, 6 and July 19, 2009 as well as February 7, 8 and 9, 2011.

The ESPaDOnS data were reduced using Libre-Esprit in a manner similar to that described above. The FEROS data were reduced using the data-reduction software (DRS) implemented under MIDAS (Kaufer et al., 1999). The log of unpolarised spectra is presented in Table 2.3.

2.2.3 Longitudinal Magnetic Field Measurements

The circular polarisation observations were analysed using the multi-line analysis technique Least Squares Deconvolution (LSD; Donati et al. 1997). LSD combines the information from essentially all metallic and He lines in the spectrum by means of the assumption that the spectrum can be reproduced by the convolution of a single "mean" line profile (the LSD profile) with an underlying spectrum of unbroadened atomic lines of specified line depth, Landé factor, and wavelength (the line mask, as described by Wade et al., 2000). This process allows the computation of single averaged Stokes *I* and *V* profiles with much higher signal-to-noise ratios than those of the individual lines, dramatically improving the detectability of Zeeman signatures due to stellar magnetic fields.

The atomic data were taken from the Vienna Atomic Line Database (VALD) (Piskunov et al., 1995; Ryabchikova et al., 1997; Kupka et al., 1999, 2000). The VALD line list used in this analysis is characterised by the stellar effective temperature T_{eff} and surface gravity log g reported in Table 2.1, abundances as derived from the detailed abundance analysis (see Sect. 2.8), and an unbroadened line depth threshold equal to 1% of the continuum intensity I_c, yielding approximately 10000 lines in the ESPaDOnS spectral window and 8000 lines in the HARPSpol window. The line depths were then interactively adjusted so that the line depths predicted by the LSD convolution model matched the observed depth of the spectral absorption lines as well as possible, thus improving the fit between the spectrum and the LSD model. Because Stokes *V* profiles are detected in many individual spectral lines of HD 133880, we ver-

Table 2.2: Log of ESPaDOnS and HARPSpol observations of HD 133880. Listed are the instrument used, the Heliocentric Julian date of the midpoint of the observation, total exposure time, the peak signal-to-noise ratio per 1.8 km s^{-1} velocity bin, the phase of the observation (according to Eq. 2), the evaluation of the detection level of a Stokes V Zeeman signature (DD=definite detection, MD=marginal detection, ND=no detection), and the derived longitudinal field and longitudinal field detection significance z from both V and N. In no case is any marginal or definite detection obtained in the N profiles.

Instrument	HJD	t_{exp} (s)	SNR pix^{-1}	Phase	Detect	V $B_\ell \pm \sigma_B$ (G)	z	N $B_\ell \pm \sigma_B$ (G)	z
ESPaDOnS	2455411.732	720	629	0.640	DD	2029 ± 38	53.4	-51 ± 31	1.6
ESPaDOnS	2455756.795	720	697	0.878	DD	-2103 ± 38	55.3	43 ± 23	1.9
ESPaDOnS	2455757.877	720	573	0.111	DD	-3671 ± 43	85.4	-23 ± 26	0.88
HARPSpol	2455319.726	520	449	0.787	DD	650 ± 62	10.5	-15 ± 58	0.26

Table 2.3: Log of unpolarised spectra. Listed are the instrument used, the Heliocentric Julian date, the peak SNR per 1.8 km s^{-1} velocity bin, the exposure time and the phase computed using the ephemeris of Eq. (2).

Instrument	HJD	SNR	t_{exp} (s)	Phase
ESPaDOnS	2455412.727	180	386	0.774
ESPaDOnS	2455414.728	180	394	0.054
FEROS	2454867.846	130	143	0.809
FEROS	2454868.818	130	103	0.917
FEROS	2455031.608	250	122	0.438
FEROS	2455599.820	240	141	0.990
FEROS	2455600.828	240	151	0.139
FEROS	2455601.868	300	121	0.325

ified (by examining simultaneously the Stokes V and I profiles) that this adjustment procedure also resulted in a better agreement between the observed and computed Stokes V spectrum.

The mean longitudinal magnetic field was measured by computing the first-order moment of the Stokes V LSD profile within the line according to the expression:

$$\langle B_z \rangle = -2.14 \times 10^{11} \frac{\int v V(v) \mathrm{d}v}{\lambda g_{\text{eff}} c \int [I_c - I(v)] \, \mathrm{d}v}, \tag{2.1}$$

where $\langle B_z \rangle$ is in G, g_{eff} is the effective Landé factor, λ is the mean wavelength of the LSD line in Å (typically around 5200 Å), and v is the velocity within the profile measured relative to the centre of gravity (Mathys et al., 1989; Donati et al. 1997; Wade et al., 2000). The uncertainties associated with $\langle B_z \rangle$ were determined by propagating the formal (photon statistical) uncertainties of each pixel through Eq. (1). The integration ranges employed in the evaluation of Eq. (1) associated with each Stokes profile were selected individually through visual inspection so as to include the entire span of the (highly variable) Stokes I profile.

2.2.4   ATCA radio continuum measurements

HD 133880 was observed with the Australia Telescope Compact Array (ATCA) at 6 cm and 3.5 cm wavelength simultaneously on February 12, 14 and 16, 1995. On each day, the observation spanned ~10 hours, during which time we observed HD 133880 continuously apart from short (~3 mins) scans of a secondary calibrator at regular (~20 mins) intervals. In this way, we were able to attain full coverage in rotation phase for the star, with repeated coverage (on two separate days) for just over half a rotation phase to check where any observed variations

were repeatable (as indeed they were, as shown in Fig. 2 of Lim, Drake & Linsky 1996). The primary (absolute flux density) calibrator used was PKS1934-638, and the secondary (complex gain) calibrator PKS1458-391. We reduced the data in the standard fashion using MIRIAD, being careful to omit data with poor phase coherence (typically at the beginning and end of each day when the source was low in the sky).

2.3 Rotation period

A period of 0.87746 ± 0.00001 d was reported by Waelkens (1985) based on Geneva photometric observations. Landstreet (1990) recommended an adjustment of the period to 0.877485 ± 0.000020 d to bring the magnetic measurements reported by Borra & Landstreet (1975) into agreement with those that he had acquired in 1987 and 1988.

When we phase the accumulated magnetic measurements of HD 133880 (i.e. the three measurements of Borra & Landstreet (1975), the 12 measurements of Landstreet (1990), and the 4 new measurements presented here) according to Landstreet's (1990) ephemeris, we observe a systematic offset of ~ 0.1 cycles between the new measurements and those published previously. Such an offset could be interpreted as the consequence of a small error in the assumed period. However, given the presence of important abundance non-uniformities on the surface of HD 133880, it is likely that the shape, and possibly the amplitude of the longitudinal field variation derived from metallic lines (i.e., our new LSD measurements) and those derived from hydrogen lines (i.e., the previously published measurements) may differ. Given the sparse phase coverage of our new measurements, it is therefore ambiguous whether this apparent offset is truly a consequence of a period error.

In an attempt to resolve this uncertainty, we examined the photometric measurements obtained by the Hipparcos mission (ESA, 1997). One hundred $H_{\rm p}$-band measurements of HD 133880 are reported in the 1997 edition of the catalogue.[1] The periodogram of those measurements in the range 0.5-1.5 days shows a clear, unique peak at 0.877479 ± 0.000030 d (The uncertainty on the period, which corresponds to 1σ confidence, is computed assuming Gaussian statistics by calculating the variation of the reduced χ^2 of a sinusoidal fit to the phased measurements in the vicinity of the best-fit period (e.g., Press, Flannery & Teukolsky, 1986)). A similar analysis applied to Waelkens' (1985) 37 V-band measurements yields $0.877459^{+0.0001}_{-0.00006}$ d. Both of these periods are consistent within the (1σ) error bars. To improve the precision of the period, we combined the two datasets. First, we used the transformation reported by Harmanec (1998) to convert the $H_{\rm p}$ measurements to Johnson V-band. We then performed the same period analysis on the combined data set (spanning nearly 15 years), obtaining a period

[1] vizier.u-strasbg.fr/viz-bin/VizieR-S?HIP%2074066

of 0.8774731 ± 0.0000060 d.

Therefore the photometric data are indicative of a period of 0.8774731 d, intermediate between those of Waelkens (1985) and Landstreet (1990).

We note that if we phase the magnetic data with the above photometric period, a slightly longer period of 0.877476 d is necessary to bring the new magnetic measurements into better agreement with the older measurements. Finally, this period also removes the phase offset between the observed radio flux variation noted by Lim, Drake & Linsky (1996) and the magnetic extrema.

Based on these results, we adopt the following ephemeris for HD 133880:

$$JD_{H\alpha^{max}} = 2445472.000(10) + 0.877476(9) \cdot E, \qquad (2.2)$$

where we have adopted a zero point corresponding to minimum photometric brightness (which occurs simultaneously with the minimum of the longitudinal magnetic field). We determined this (3σ) uncertainty by examining the χ^2 of the fit to the photometric data about this best-fit value.

2.4 Determination of Physical Parameters

2.4.1 Effective Temperature

The enhanced metal abundances and the effects of the magnetic field have to be taken into account when determining the effective temperatures of Ap stars (Stepien & Dominiczak, 1989; Hauck & Kunzli, 1996). As a result, effective temperatures determined using Geneva and/or Strömgren $uvby\beta$ photometry using normal star calibrations must be corrected to the Ap stars temperature scale. However, Hauck & North (1993) suggest that stars that are either He-weak or He-strong do not require that their temperatures be corrected.

HD 133880 has available both Geneva and Strömgren $uvby\beta$ photometry for the determination of effective temperature. We have used both in this analysis. For the Geneva photometry we have used the FORTRAN program described by Kunzli et al. (1997), and discussed by Landstreet et al. (2007), to obtain an estimate of the effective temperature. For the Strömgren $uvby\beta$ photometry we used the FORTRAN code "UVBYBETANEW-ap" which is a modified version of "UVBYBETANEW" (Napiwotzki et al., 1993; Moon & Dworetsky, 1985) that corrects the effective temperature to the Ap temperature scale. However, in this analysis no correction was applied to the temperature because HD 133880 is classified as a He-weak star (Hauck & North, 1993), which is confirmed in this thesis (see Sect. 2.8).

We found T_{eff} = 13300 K and 12700 K using $uvby\beta$ and Geneva photometry respectively.
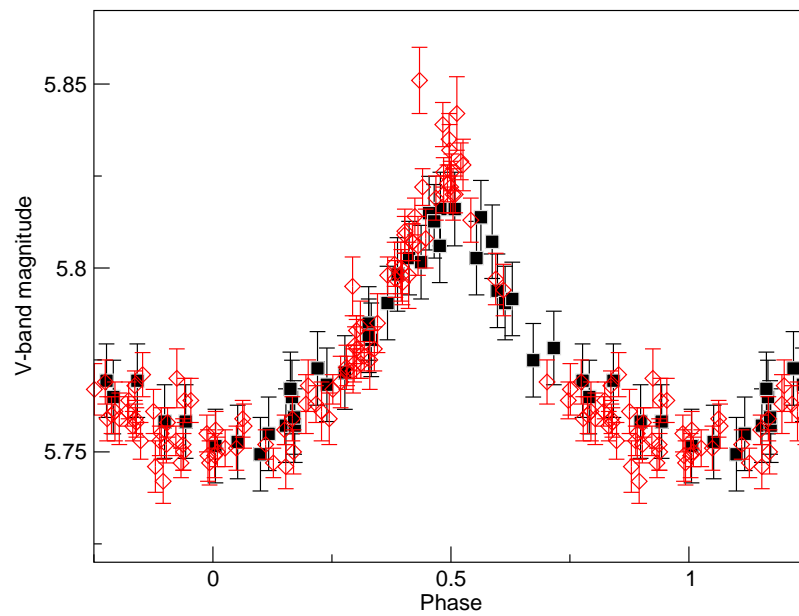
Figure 2.1: Phased *V*-band (Waelkens (1985); filled squares) and H_p-band (ESA 1997; open diamonds) photometry. The Hipparcos photometry has been scaled to the Johnson *V* system using the transformation of Harmanec (1998).

The scatter of these measurements about their mean is of the order of 300 K. Given the intrinsic uncertainties in determining the effective temperature for a magnetic Ap star, in addition to the global uncertainties in the applied methods we optimistically adopt an uncertainty of approximately ±600 K. Both the Geneva and *uvbyβ* photometries are rotationally averaged values and their variations are included within the quoted uncertainties. We use the average of the computed temperatures, adopting an effective temperature of $T_{\text{eff}} = 13000 \pm 600$ K for HD 133880. If the Ap correction to the temperature is applied, a value of $T_{\text{eff}} = 12440$ K is found, which is within the the uncertainty of our adopted value.

Netopil et al. (2008) performed an analysis on the temperature calibration of chemically peculiar stars. Included in their analysis was HD 133880. Using photometry, their calibrated temperature corrections suggest that the T_{eff} is 11930 ± 210 K. This agrees, within uncertainties, to our derived T_{eff} if we corrected our derived temperature to the Ap temperature scale. In our analysis, we favour the higher T_{eff} based on work by Hauck & North (1993) and the better quality fits to H*β* using the model fits of Kurucz (1979) with the higher of these two temperatures. We do, however, compare the derived abundances of all elements using the T_{eff} reported by Netopil et al. (2008) of 12000 K to our adopted value of 13000 K (see Sect. 8).

2.4.2 Luminosity

In addition to T_{eff} and the *V* magnitude of HD 133880 (see Table 2.1), we also require a bolometric correction in order to calculate the stellar luminosity. Landstreet et al. (2007) derived a set of bolometric corrections as a function of T_{eff} that can be applied to Ap stars. Applying this correction (see Equation 1 in Landstreet et al. (2007)) results in log $L/L_{\odot} = 2.02 \pm 0.10$. Here, the uncertainty was estimated in the same manner as described by Landstreet et al. (2007). Note that we used E(B - V) = 0.00 to compute the luminosity, which is confirmed by looking at the colour-colour diagram of (U - B) versus (B - V)

2.4.3 Other Parameters

Based on values of T_{eff} and luminosity determined in Sect. 2.4.1 and 2.4.2, the stellar radius is found to be $R = 2.01 \pm 0.32 \ R_{\odot}$. Landstreet et al. (2007) report a mass for HD 133880 of $M = 3.20 \pm 0.15 \ M_{\odot}$ (consistent with the values of T_{eff} and luminosity in this chapter), which can be used with the derived radius to estimate the surface gravity, log *g*. We find log $g = 4.34 \pm 0.16$, consistent with young age.

From our adopted period of P = 0.877476 ± 0.000009 days (Sect. 2.3) and $v \sin i = 103 \pm 10$ kms^{-1} (see below) we can estimate the inclination angle of the rotation axis to the line of

sight, i, using the equation

$$\sin i = \frac{(v \sin i)P}{50.6R}, \tag{2.3}$$

where $v \sin i$ is in km s^{-1} and R in solar radii, to obtain a value of $i = 63° \pm 18°$. All the physical parameters derived are summarised in Table 2.1 and are in agreement with those reported by Landstreet et al. (2007).

2.5   Line profile variations

To characterise the line profile variability of HD 133880 we measured the equivalent width variations for a number of spectral lines. The spectral lines were re-normalised to the surrounding continuum regions and the equivalent widths were computed by numerically integrating over the line profile. A single uncertainty value was estimated for each pixel from the RMS scatter in the continuum regions surrounding the line profile and the resulting uncertainties in the equivalent width measurements were found by adding the pixel uncertainties in quadrature.

In Fig. 2.2, we show equivalent width measurements phased to the ephemeris given in Eq. (2.2) for select lines of titanium, iron, chromium and silicon. The equivalent width curves are all similar and show strong, approximately sinusoidal variations consistent with the rotation period. For each element, the equivalent width reaches a minimum at about phase 0.5. The largest variation is seen in the Cr II 4588 Å line with the equivalent width measurements almost doubling in value. Similar equivalent width changes are found in the Ti II 4533 Å and Fe II 4583 Å lines, but a much smaller amplitude of the variation is measured in the Si II 5056 Å doublet. Clear variations are also seen in other spectral lines of these elements.

The equivalent width variations for each of the elements plotted in Fig. 2.2 appear to be the result of absorption features travelling through the line profile. The net result is a variation in the total depth, as well as shape, of the line, as demonstrated by the profiles shown in Fig. 2.3. The Si line plotted in Fig. 2.3 has the simplest variations, with what appears to be a single feature travelling from negative to positive velocities. The variations in the other lines are phased similarly, but the line profiles are generally more complex.

2.6   Magnetic Field Model

Before any meaningful abundance analysis can be done, we need to establish an appropriate magnetic field model. Landstreet (1990) derived a best-fit magnetic field model based on longitudinal field measurements of Hβ for HD 133880. He adopted a magnetic field geometry
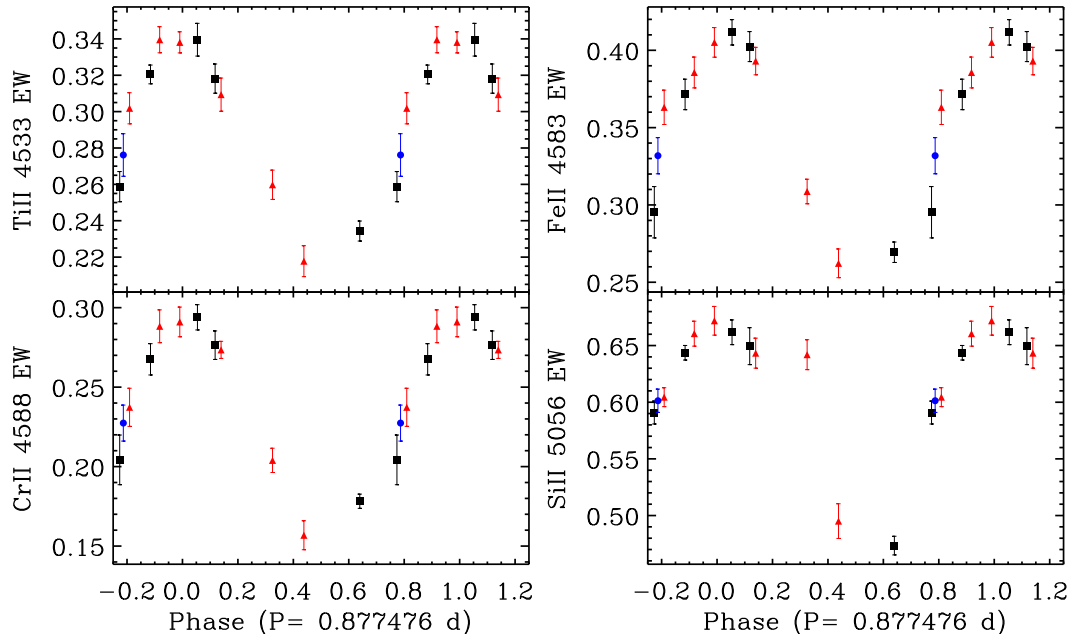
Figure 2.2: Phased equivalent widths measurements for the indicated spectral lines measured from the ESPaDOnS (black squares), FEROS (red triangles) and HARPSpol (blue circles) datasets.

with the inclination angle of the line-of-sight to the rotation axis, i, equal to the angle of the magnetic field axis to the rotation axis, β with a value of 90° ($i = \beta = 90°$). The dipolar and quadrupolar components were $B_d = -8125$ G, and $B_q = -10900$ G, respectively. (Note that we have corrected negative sign errors in both components for the derived field reported by Landstreet (1990)). From this model, it was established that the predominant magnetic field distribution over the stellar surface is quadrupolar with $\langle B_z \rangle$ variations that are clearly not sinusoidal. Further, since a change in the sign of the longitudinal field is observed, $i + \beta$ must be greater than 90°. However, Landstreet's adopted geometry is barely consistent with our calculated inclination of $i = 63° \pm 18°$ (see Sect. 2.4). Also, Landstreet (1990) had no information about the variations of the surface magnetic field modulus, $\langle B \rangle$, making it difficult to constrain the field further. Landstreet (1990) pointed out that there is not a unique model for the observed magnetic curve of HD 133880 and suggested an alternate geometry of $i = 80°$ and $\beta = 55°$ that produces a similar curve (note that the values of i and β can be interchanged without affecting the magnetic curve). This second geometry is therefore in much better agreement with our derived value of i. Unfortunately, Landstreet (1990) did not provide the values of the dipole and quadrupole components for this alternate geometry. We therefore search for a new magnetic field model that agrees well with our derived value for i of $63° \pm 18°$.
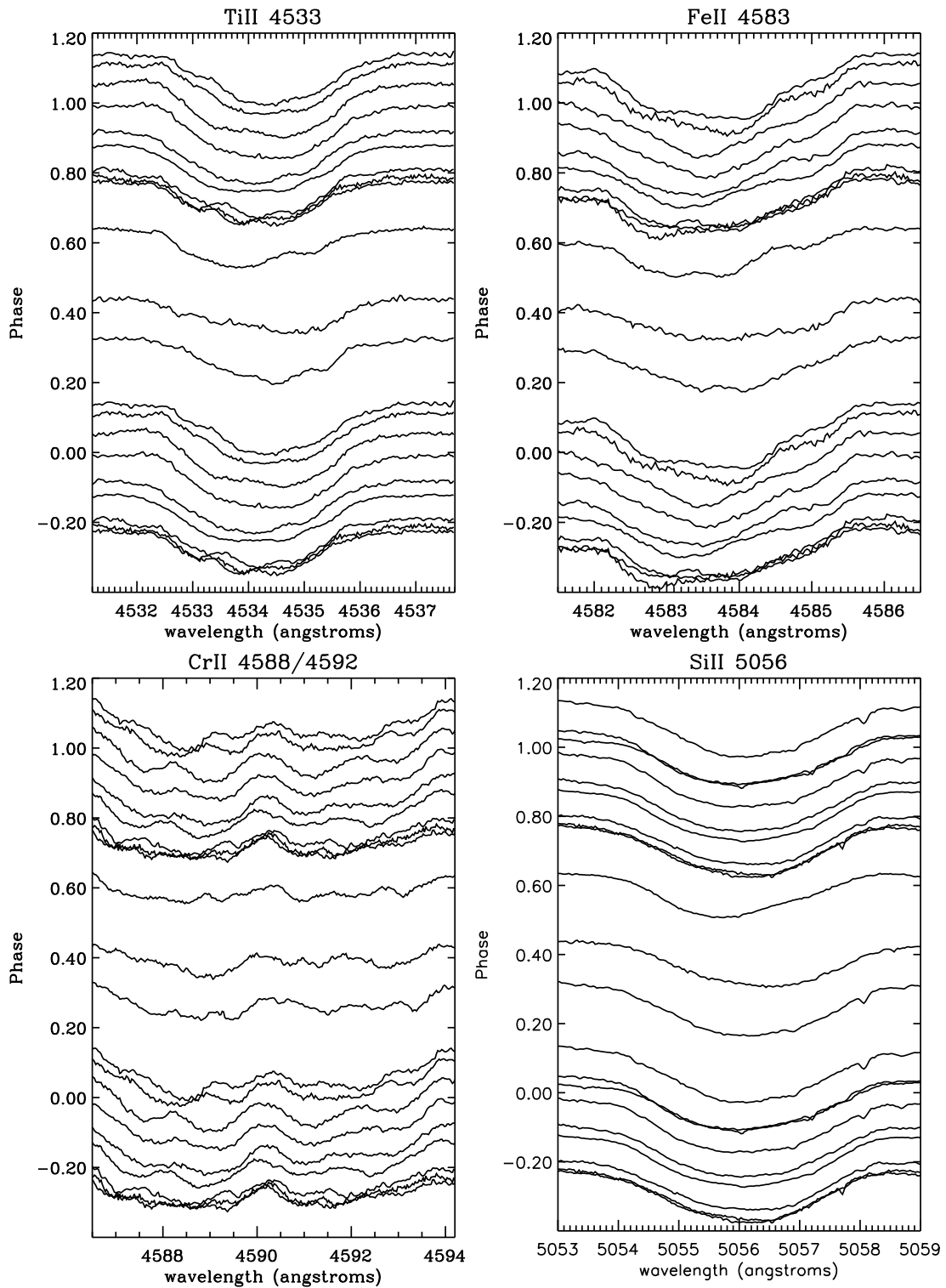
Figure 2.3: Observed metallic line profiles for the indicated lines. Shown are the continuum-normalised spectra, displayed in such a way that the continuum of each spectrum is plotted at a position on the vertical axis that corresponds to the phase of the observation.
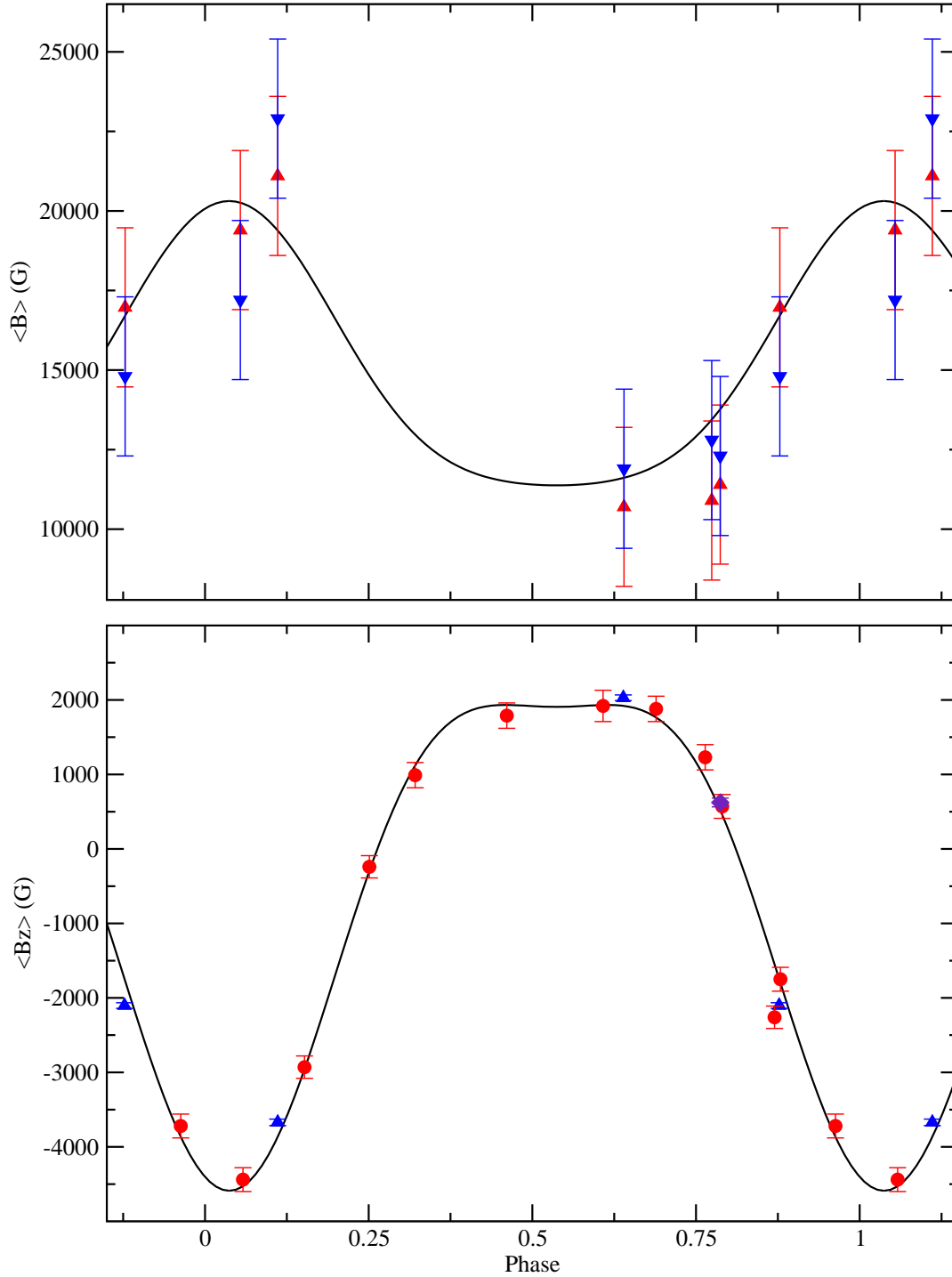
Figure 2.4: The top panel depicts the surface magnetic field modulus variations as measured from Fe II (red upward facing triangles) and Cr II (blue downward facing triangles) with the solid (black) curve representing the adopted best-fit model. The bottom panel shows the $\langle B_z \rangle$ field variations observed for HD 133880 for our adopted magnetic field model. The red circles are measurements from Landstreet (1990) using Hβ, the blue triangles are LSD measurements from ESPaDOnS, the purple diamond HARPS and the solid (black) curve the adopted magnetic field model. The minima of the $\langle B_z \rangle$ and $\langle B \rangle$ curves occur at phases 0.037 and 0.537 respectively.

Table 2.4: Lines used to measure $\langle B \rangle$. The atomic data were gathered from the VALD database.

Element	Small z		Large z	
	λ (Å)	z	λ (Å)	z
Fe II	4508.288	0.50	4520.224	1.34
Cr II	4284.188	0.52	4261.913	1.080

2.6.1   Surface magnetic field modulus measurements

To further constrain the magnetic field, information about the surface magnetic field modulus $\langle B \rangle$ is required. To obtain this, we cannot rely on Zeeman splitting because rotational broadening dominates the spectrum, smearing out any observable Zeeman components. Although dominated by rotation, the magnetic field contributes a measurable fraction to the width of a (Stokes I) spectral line. Preston (1971) outlines a method to obtain mean surface field measurements from rotationally broadened spectral lines. By comparing the widths of two spectral lines of a given element that have a large and small mean Landé factor (i.e., lines that are strongly affected by the local magnetic field to ones that are not) we can obtain a meaningful measurement of the magnetic field modulus. Preston (1971) defines a parameter K:

$$K \equiv \left(\frac{w_L^2 - w_S^2}{\langle \lambda^4 z^2 \rangle_L - \langle \lambda^4 z^2 \rangle_S} \right)^{1/2} , \tag{2.4}$$

where w_L and w_S are the averages of the measured line widths, in cm, of lines with a large and small Landé factor respectively, λ is the wavelength in cm and z the mean Landé factor where the L and S subscripts refer to the lines with large and small Landé factors respectively. Preston then finds the relationship between the surface field and K to be

$$B_s(kG) = 0.5 + 7.9K. \tag{2.5}$$

The challenge with HD 133880 was to find a pair of spectral lines that were not strongly blended with other lines from which to measure line widths. Table 2.4 presents two sets of lines for Cr II and Fe II from which line widths could be measured.

Although good candidates, these spectral lines are still quite blended with adjacent lines in the spectrum. To combat this problem, we measured line widths at the continuum by repeatedly fitting Gaussians to the spectral line using IRAF's *splot* function. The average width for each feature is taken in our calculation. We were also limited by resolving power and SNR in our

Table 2.5: $\langle B \rangle$ measurements from lines of Cr II and Fe II for spectra from ESPaDOnS and HARPSpol. Phases are computed from Eq. 2 and uncertainties estimated to be ±2.5 kG.

Instrument	Phase	$\langle B \rangle$ (kG) Fe II	Cr II
ESPaDOnS	0.054	19.4	17.2
ESPaDOnS	0.111	21.1	22.9
ESPaDOnS	0.640	10.7	11.9
ESPaDOnS	0.774	10.9	12.8
HARPSpol	0.787	11.4	12.3
ESPaDOnS	0.878	16.9	14.8

FEROS spectra. Specifically, the combination of the lower resolution of the FEROS instrument and lower SNRs in the data meant that we were unable to unambiguously measure the spectral line widths. As a result, only the ESPaDOnS and HARPSpol spectra could be utilised. Results are summarised in Table 2.5 and illustrated in the top panel of Figure 2.4.

It is encouraging that the magnetic field values measured from both Fe II and Cr II agree well with one another, suggesting the variations are indeed real. Due to the high blending in the spectral lines and the ambiguity in measuring the line widths, we estimate the uncertainties to be ± ~ 2500 G, though this value may be optimistic. Although this method is not as precise as measuring the splitting of spectral lines due to the Zeeman effect, it does provide meaningful constraints on the magnetic field. It is clear from these measurements that the surface field varies from about 20 kG at the negative magnetic pole to 10 kG near the positive magnetic pole (see below). The derived field is consistent with a non-sinusoidal curve (though no definitive conclusions can be made given the limited number of data points and size of the error bars), much in the same manner to the line-of-sight magnetic field, but in the opposite sense: the maximum of the longitudinal field curve corresponds to the minimum of the surface integrated field curve. More measurements of $\langle B \rangle$ are required to constrain the field further which requires more high SNR observations of HD 133880.

2.6.2 Magnetic field geometry

The FLDSRCH program was used to obtain the magnetic field geometry for HD 133880 (Landstreet & Mathys, 2000). This program has longitudinal and surface magnetic field strengths at
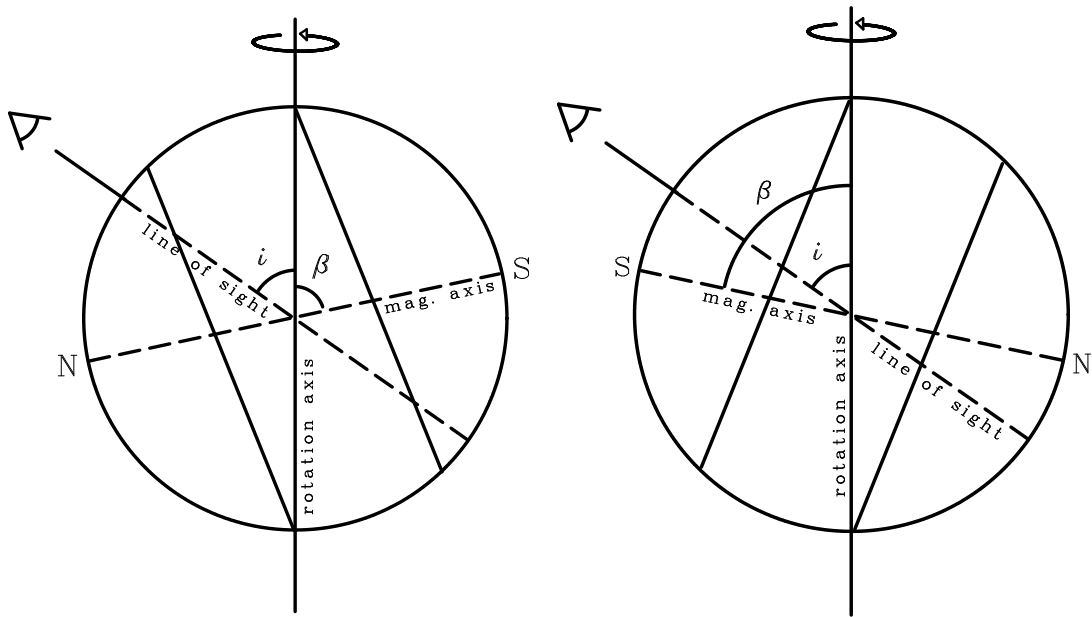
Figure 2.5: The geometry adopted for HD 133880. The vertical axis is the rotation axis of the star. The angle between the line of sight and the rotation axis is $i = 55°$. The angle between the rotation axis and the magnetic field axis is $\beta = 78°$. The left panel depicts an orientation where the positive magnetic pole is closest to the line of sight (phase $\phi = 0.537$) and the right panel is when the negative magnetic pole is nearer alignment with the line of sight ($\phi = 0.037$). The bands used for dividing the abundance distribution are shown as solid lines and are normal to the magnetic field axis.

four different phases as input, which are then used to iteratively search for the best fit i, β, B_d, B_q, and B_{oct}. For a more complete description refer to Bailey et al. (2011). Measurements of $\langle B_z \rangle$ from Landstreet (1990), as well as the four new measurements from this work, provide good constraints on the observed variations. We also have important limits on $\langle B \rangle$ that appear to range from 10 kG to 20 kG near the positive and negative magnetic poles respectively (see above). This information allowed us to derive a new field geometry: $i=55° \pm 10°$, $\beta=78° \pm 10°$, $B_d = -9600 \pm 1000$ G, $B_q = -23200 \pm 1000$ G, and $B_{oct} = 1900 \pm 1000$ G. Uncertainties were estimated by observing the deviations from the derived field by changing the input parameters of $\langle B_z \rangle$ and $\langle B \rangle$ within their uncertainties. This field corresponds well with our calculated value of $i = 63° \pm 18°$ and has the added advantage of agreeing with the alternate geometry proposed by Landstreet (1990) (see above). An illustration of our adopted geometry is presented in Figure 2.5. The bottom panel of Figure 2.4 shows the model $\langle B_z \rangle$ curve over-plotted with $\langle B_z \rangle$ measurements from Landstreet (1990) and this thesis. All the measurements agree well with the computed model and the measurements made using the metallic spectrum agree remarkably well with Landstreet (1990) who made measurements from Hβ. The field varies non-sinusoidally from about -4.5 kG at phase 0.037 to 2 kG at phase 0.537. The field curve is flat and extended around the positive magnetic pole with a rapid decline towards the negative magnetic pole. The quadrupole-to-dipole ratio, q, of the adopted model is 2.4, which clearly indicates the presence of a strong quadrupole component. We therefore concur with the conclusion of Landstreet (1990) that the field of HD 133880 departs in a significant way from a simple centred dipole.

2.7   Abundance Model

We utilise the FORTRAN program ZEEMAN (Landstreet, 1988; Landstreet et al., 1989; Wade et al., 2001) to perform the abundance analysis of HD 133880. ZEEMAN computes emergent spectra of all four Stokes parameters for stars with a permeating magnetic field. It assumes a low-order multipole geometry for the magnetic field based on the above derived values for i, β, B_d, B_q, and B_{oct}. Up to ten phases of observed Stokes I spectra can be fit simultaneously with the abundance of one element varied at a time. For each iteration, ZEEMAN automatically adjusts $v \sin i$ and the radial velocity of the star to optimum values. Currently, up to six rings of uniform abundance on the surface of the star can be specified that have equal spans in magnetic co-latitude. ZEEMAN produces output for the abundance distribution of a given element at different magnetic latitudes. In effect, this model provides a rough 1D map of the variation of abundance from one magnetic pole to the other.

   Initially, uniform mean abundances for each phase of HD 133880 were found, however, we

quickly discovered that a multi-ring model would provide a better fit. As explained by Bailey et al. (2011), zeeman was designed to quantify hemispherical abundance variations for stars similar to 53 Cam (=HD 65339) (Landstreet, 1988). HD 133880 exhibits large-scale abundance variations over the stellar surface and, as is evident from the longitudinal magnetic field curve, both magnetic hemispheres are observed. Our preliminary abundance analysis suggested that a maximum of three rings should be used to quantify the abundance variations because we saw abundance anomalies that varied between both magnetic poles and the magnetic equator. Nevertheless, we experimented with fewer and more rings on the surface of the star. We found that more than three rings did not significantly improve the quality of fits and fewer rings did not adequately model the observed variations in the Stokes I spectra.

For our analysis, T_{eff} was set to 13000 K and $\log g$ to 4.3 which are both consistent with the values determined in Sect. 2.4. The atomic data were taken from Vienna Atomic Line Database (Piskunov et al., 1995; Ryabchikova et al., 1997; Kupka et al., 1999, 2000). The best-fitting value of $v \sin i$ was found to be 103 ± 10 km s^{-1}. Due to the strong blending in the spectral lines, identifying the best fit required visual evaluation of the agreement between the computed and the observed Stokes I spectral lines in several windows of the order of 80 Å wide. Since the strong magnetic field should suppress any convective motions, which in any case are expected to be small at this T_{eff}, the microturbulence parameter was set to 0 km s^{-1}.

2.7.1 Spectra normalisation

For stars in which $v \sin i$ is greater than around 100 km s^{-1} (as is the case for HD 133880) the dominant source of error in abundance analysis is from continuum normalisation. The reason for this is that in a spectral region that is on the order of 100 Å wide, there may only exist a few continuum points from which to normalise the spectrum. Often it is difficult to determine which features should be placed near the continuum and which should not. To combat this problem, we performed continuum normalisation of spectra of normal, sharp-lined, A-type stars from both the ESPaDOnS and FEROS instruments to determine the highest degree polynomial required to normalise a given spectral window. All spectral windows were about 100 Å wide to maximise the number of continuum points present in the broad-line spectra. In all cases, no greater than two segments of a cubic spline were required to normalise the normal A-star spectra correctly. For a given instrument and spectral window, we also used two segments of a cubic spline to continuum fit the spectra for HD 133880. In this manner, we reduce the uncertainty introduced in the placement of the continuum and ensure that all spectra are normalised in the same way. Where necessary, we iteratively performed continuum fitting for spectral windows for which synthetic spectra from zeeman agreed poorly with our initial

normalisation. Hill (1995) discusses further challenges in performing abundance analysis on broad-lined stars.

2.7.2 Choice of magnetic field model

As described in Section 6, two magnetic field models adequately characterise the observed variations of the longitudinal magnetic field, $\langle B_z \rangle$: that of Landstreet (1990) and the one presented in this thesis. To explore the effect of different magnetic field geometries on the derived abundances, we performed abundance analysis of HD 133880 for all elements using both geometries. The maximum abundance differences between the two models were found to be 0.1-0.2 dex. We therefore adopt the new magnetic field geometry presented in this thesis because it agrees well with the value of i derived from physical parameters and has the added constraints of the observed surface magnetic field modulus variation, $\langle B \rangle$. We report all abundances using the new magnetic field geometry.

2.8 Abundance analysis

A total of 12 spectra, well spread in phase, were available for HD 133880, from the FEROS, ESPaDOnS and HARPS instruments. The HARPS spectrum was not used in the abundance analysis because its phase corresponded closely to two other spectra with comparable SNR and thus added no new relevant information. The large wavelength coverage of these instruments has allowed us to derive abundance distributions for O, Mg, Si, Ti, Cr, Fe, Pr, and Nd, as well as upper limits for the abundances of He and Ni. The large $v \sin i$ presented challenges in deriving abundances due to the presence of significant blending in the spectra. Nevertheless, multiple relatively clean lines of the majority of elements studied were found with varying strengths and Landé factors, providing better constraints on the derived abundances.

As discussed in the previous section, the present dataset is sufficient to perform abundance analysis using a three-ring model with rings encompassing both magnetic poles and the magnetic equator with equal span in co-latitude (60°). Initially six spectra were used (2 ESPaDOnS and 4 FEROS) that were well spaced in phase to derive the three-ring abundance model. Once the mean abundance values were found for each ring, model fits were produced for all spectra. We have no observations for HD 133880 very close to the positive magnetic pole (phase 0.537). We do, however, have two spectra sufficiently near the positive pole, at phases 0.438 and 0.640, adequate for providing a first approximation to the abundance distributions near the positive pole.

Table 2.6: Abundance distribution of elements studied for HD 133880.

	He	O	Mg	Si	Ti	Cr	Fe	Ni	Pr	Nd
					$\text{Log}(n_X/n_H)$					
Ring $0-60°$ (negative pole)	≤ -2.00	-2.78	-3.84	-2.79	-5.39	-4.55	-3.32	≤ -4.40	-6.52	-6.55
Ring $60-120°$ (magnetic equator)	–	-3.38	-4.37	-2.64	-5.62	-4.54	-3.44	–	-6.72	-6.47
Ring $120-180°$ (positive pole)	–	-3.10	-3.91	-3.93	-6.75	-5.20	-4.11	–	-7.28	-8.22
σ	–	±0.3	±0.3	±0.2	±0.2	±0.15	±0.1	–	±0.2	±0.3
Solar abundance	-1.07	-3.31	-4.40	-4.49	-7.05	-6.36	-4.50	-5.78	-11.28	-10.58
# of lines modelled	–	1	1	4	3	3	3	1	3	1

The mean abundances derived for each element in each ring are tabulated in Table 2.6 along with solar abundances reported by Asplund et al. (2009). The quality of fits was tested (where possible) using multiple spectral windows with derived uncertainties estimated from the observed window to window scatter of the abundance. For lines for which there was only one spectral line or region, we estimate the uncertainties to be about ±0.3 dex, which is the average deviation from the derived abundance required to make the quality of fit unsatisfactory between the model and observed spectra upon visual examination. We also derived a set of abundances using T_{eff} = 12000 K as reported by Netopil et al. (2008) for each of the elements listed in Table 2.6. We found that the abundances in each of the three rings changed by ±0.10 dex, or less, for the Fe-peak elements (Ti, Cr, Fe) and no more than ±0.15 dex for the rare-earths (Pr and Nd), O, Mg, and Si which are within our quoted uncertainties. This suggests that the choice of T_{eff} does not significantly influence the derived abundances for HD 133880. To illustrate the quality of fits of the three-ring model, two 80 Å windows for all 11 modelled spectra are shown in Figures 2.6 and 2.7. The quality and consistency of the model are discussed below for each element modelled.

2.8.1   Helium

Many possible lines of He I are considered when determining the abundance of helium: 4471, 5015, 5047, 5876, and 6678 Å. However, none of these lines are unambiguously detected. Nevertheless, fitting these regions provides a useful upper limit to the abundance of helium. Our analysis confirms that HD 133880 is a He-weak star with the abundance of helium at least a factor of 8 below the solar abundance.

2.8.2   Oxygen

HD 133880 is classified as a Bp star with the λ4200-Si anomaly which suggests that the oxygen abundance should be near or less than the solar abundance (Sargent & Searle, 1962; Roby & Lambert, 1990). Initially, we attempted to derive the oxygen abundance using the 7771-75 Å triplet. These lines suffer from strong non-LTE effects and are highly saturated, making them unreliable for abundance determination. A more useful set of lines are those at 6155-56-58 Å; the abundance distribution reported in Table 2.6 is from these lines. These lines are unambiguously detected, but are somewhat blended with Pr II near the redward wing. The O abundance varies from the magnetic poles to equator by a factor of about 2-3. At all phases, oxygen is found from these lines to be overabundant near the negative and positive magnetic poles by 0.5 dex and 0.3 dex compared to the solar ratio, respectively. Near the magnetic equator, oxygen is comparable in abundance to the Sun, within uncertainties.
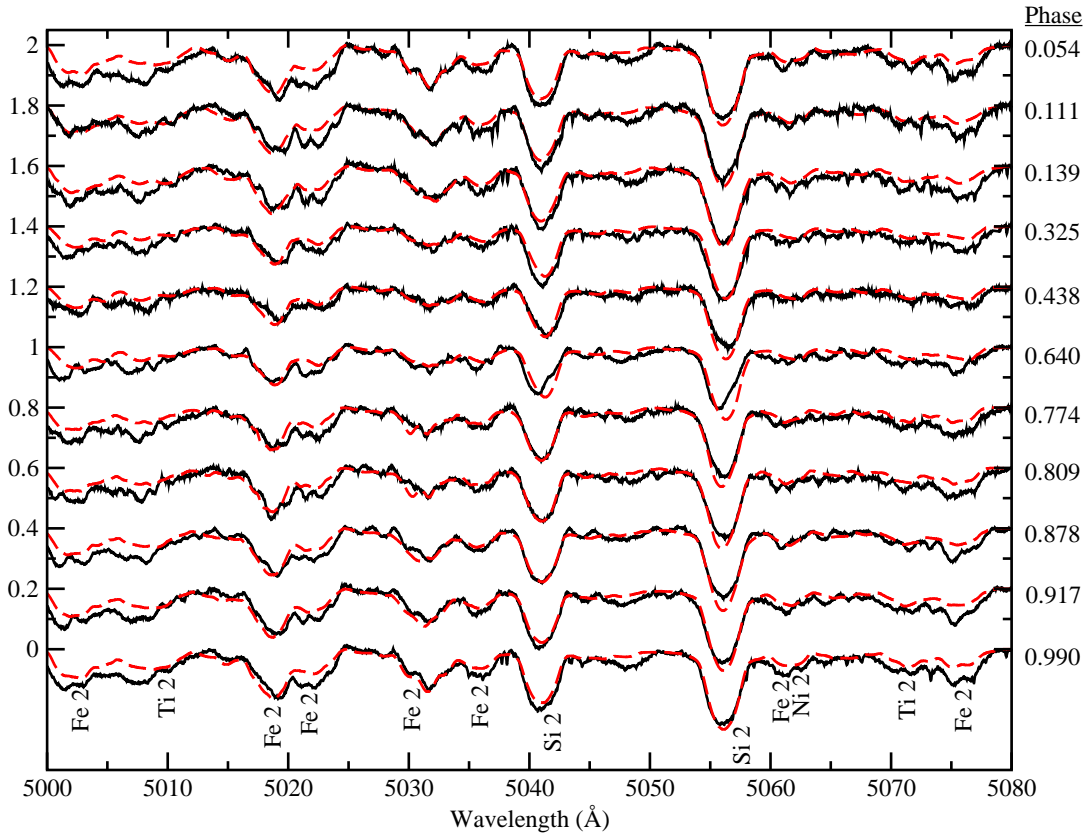
Figure 2.6: Spectrum synthesis of the region 5000 - 5080 Å using a three-ring model. The observed spectra are in black (solid) and the model fits are in red (dashed). From top to bottom phases 0.054, 0.111 (both ESPaDOnS), 0.139, 0.325, 0.438 (all FEROS), 0.640, 0.774 (both ESPaDOnS), 0.809 (FEROS), 0.878 (ESPaDOnS), 0.917, and 0.990 (both FEROS). The line of sight is closest to the negative magnetic pole at phase 0.037 and the positive magnetic pole at phase 0.537. Spectra are positioned at arbitrary positions along the vertical axis for display purposes.

2.8.3 Magnesium

Only one clean line of sufficient strength to model was found for Mg II at 4481 Å. This line shows some variability, implying an overabundance of around 0.5 dex near both magnetic poles and a roughly solar abundance near the magnetic equator.

2.8.4 Silicon

A total of four lines of Si II were found that were suitable for modelling: 5041 Å, the doublet at 5055-56 Å, 5955 Å and 5978 Å. The first two lines of Si II were fit simultaneously and the

result tested by using the same derived abundance model in the latter two lines. Satisfactory fits were obtained at each phase for all lines of Si, however the doublet at 5055-56 Å was systematically too strong in the model at all phases (see Figure 2.6). Finding the best fit model for the longer wavelength lines did not rectify the problem of stronger spectral lines in the model and produced a similar abundance distribution. We find large-scale abundance variations for Si on the surface of HD 133880 from pole to pole. At the negative magnetic pole and magnetic equator, Si is approximately 25 times more abundant than in the Sun. The lowest abundance is found at the positive magnetic pole where, however, Si is still about 3 times more abundant than in the Sun.

Figure 2.7 highlights three Si III lines at 4552, 4567, and 4574 Å that are not modelled well using the abundance derived from the Si II lines discussed above (red-dashed line). An enhancement of the Si II abundance of about 1 dex is necessary to model well the Si III lines (blue-dashed line). This discordance is very suggestive. The effects of non-LTE in the Si III lines are expected to be small at T_{eff} less than about 15000 K. Becker & Butler (1990) demonstrate that non-LTE effects in the Si III lines decrease towards lower temperatures. The most probable cause is strong stratification of Si in the atmosphere of HD 133880 with the abundance high in the atmosphere being much lower than near an optical depth (τ_c) of about 1. However, the large $v \sin i$ (103 km s^{-1}) makes normalisation difficult (see Sect. 2.7.1) and studies on more hot Ap stars with low $v \sin i$'s are necessary to determine how widespread this Si II/III discrepancy is, and how it may be explained.

2.8.5 Titanium

We have modelled the abundance of Ti using lines of Ti II at 4563 and 4571 Å as well as at 4805 Å. The final model was determined using the former two lines and tested using the latter line. Ti exhibits drastic variations between magnetic poles of nearly 1.5 dex which can be seen in Figure 2.7 where lines due to Ti II are much weaker at phases 0.423 and 0.625 than near phase 0. Ti is most abundant at the negative magnetic pole where it is more than 40 times more abundant than in the Sun and transitions to slightly lower abundances at the magnetic equator (~ 25 times overabundant). At the positive magnetic pole Ti is only about 2 times more abundant than the solar value.

2.8.6 Chromium

Several lines of Cr were found that were suitable for modelling, particularly the Cr II lines at 4558, 4588, and 4592 Å. The latter two of these three lines were relatively clean while λ4558 is blended with Fe II. All three lines were used to compute the three-ring model presented in
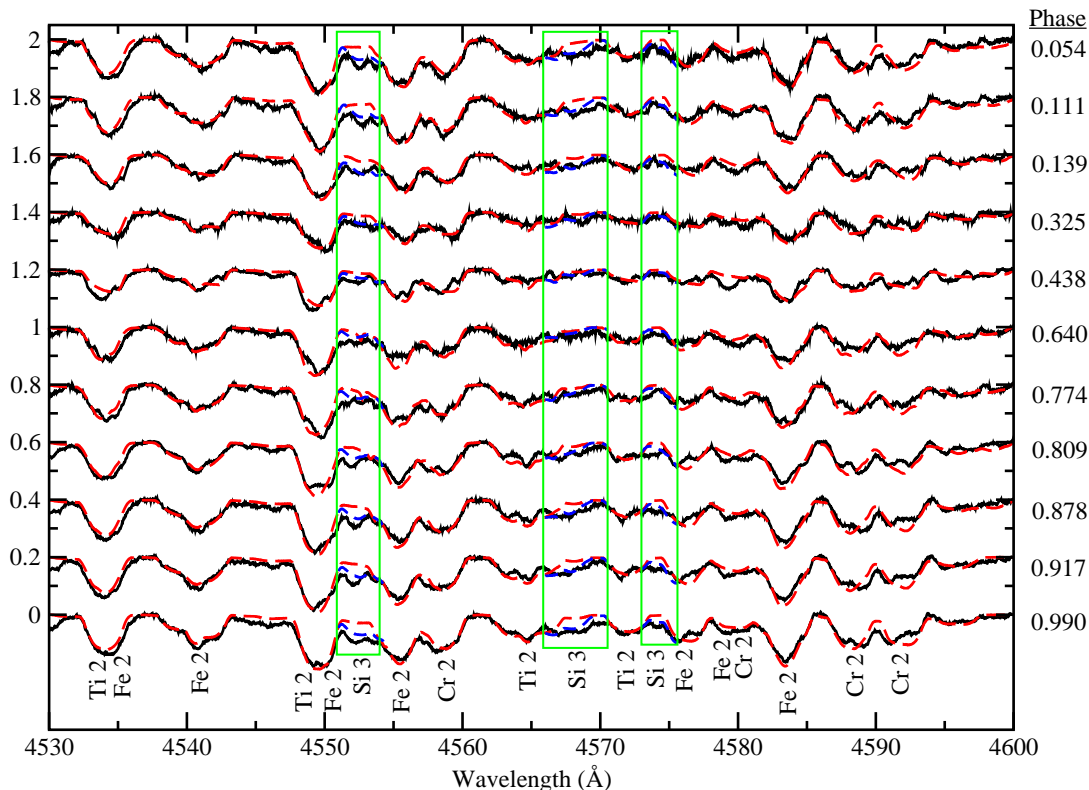
Figure 2.7: Same as Figure 6 for the region 4530 - 4600 Å. The green boxes highlight the three Si III lines at 4552, 4567, and 4574 Å. The red-dashed lines indicate the model fits to abundances derived from the Si II lines that are presented in Table 2.6. The blue-dashed lines are model fits with about a 1 dex enhancement to the Si abundances shown in Table 2.6.

Table 2.6. All Cr lines in Figure 2.7 are fit well at all phases with the model fit at 4592 Å being slightly too strong at later phases. Large variations are observed from hemisphere to hemisphere. Cr is weakest at the positive pole, but its abundance is still 10 times greater than the solar abundance. The negative pole and magnetic equator have a mean abundance that is approximately 100 times greater than in the Sun.

2.8.7   Iron

A plethora of lines are available from which to derive the abundance distribution of Fe. The model was found using Fe II lines at 4541, 4555, and 4583 Å. The lines were of sufficient strength for abundance analysis and only the line at 4555 Å is blended with Cr II. Similar to Cr, Fe is least abundant at the positive magnetic pole, where an abundance of about 2.5 times

higher than the solar abundance is found, and most abundant near the negative magnetic pole and magnetic equator where a mean abundance approximately 10 times larger than in the Sun is observed. Most lines of Fe are modelled well, as seen in Figure 2.7. Some weaker lines are systematically too weak in the model (see Figure 2.6) which is most likely attributable to unrecognized blending.

2.8.8   Nickel

There are a few possibly useful lines of Ni II to model at 5058, 5059, and 5064 Å, however none are unambiguously detected. Nevertheless, the region (labelled in Figure 2.6) proved useful for obtaining an upper limit to the abundance of Ni, which suggests that it is less than 10 times more abundant than in the Sun.

2.8.9   Praseodymium

Three lines of Pr were found that were useful for modelling. The final model was computed using Pr III and Pr II at 6160 and 6161 Å respectively. These lines are blended with the redward wing of the O I triplet at 6155-56-58 Å, but are of sufficient strength to obtain a useful abundance. The model fits were then tested using Pr III at 7781 Å. A mean abundance was found for the two rings covering the negative magnetic pole and magnetic equator that is about 10^5 times overabundant compared to the solar ratio. At the positive magnetic pole, Pr is least abundant but still 10^4 times more abundant than in the Sun.

2.8.10   Neodymium

A possible useful line of Nd III is at 6145 Å, however the SNR is such that it is not unambiguously detected at all phases and rotational broadening causes this line to be strongly blended with Fe II at 6147 and 6149 Å. We therefore turn to Nd III at 4711-12-14 Å. These lines are relatively clean, providing useful abundance determinations that reveal a strong variation in the mean abundance of Nd between magnetic hemispheres. For both the negative magnetic pole and magnetic equator Nd is greater than 10^4 times more abundant than in the Sun, whereas at the positive pole this rare-earth is about 200 times the solar ratio.

2.9   Magnetosphere

Lim, Drake & Linsky (1996) demonstrated that the 3.5 cm and 6 cm radio flux and circular polarisation of HD 133880 vary significantly and coherently according to the ~ 0.877 d pe-

riod. They reported that the emission shows broad peaks near the phases of the longitudinal field extrema (corresponding, in Landstreet's model, to the phases at which the poles of the dipole contribution to the field curve pass closest to the line-of-sight), and narrower peaks at the predicted phases of quadrupole component pole passages (i.e. the quadrupole contribution to the field curve). They also reported that the strong extraordinary-mode circular polarisation varied in sign with phase, in agreement with the sign of the longitudinal field. As described in Sect. 2.2, we have re-reduced the ATCA radio data, but there are no significant differences in the reduced data compared to that described by Lim, Drake & Linsky (1996). Here we examine the radio emission in the context of a magnetospheric picture combining the dynamical concepts summarised by Owocki, Townsend & Ud-Doula (2006) and the radio magnetosphere model of Linsky, Drake & Bastian (1992).

Using the stellar wind parameters determined using the CAK formalism (Castor, Abbott & Klein (1975): values of $\dot{M} = 10^{-11}\ M_\odot$/yr and $v_\infty = 750$ km s^{-1}), we compute the wind magnetic confinement parameter $\eta_* = B_{\mathrm{eq}}^2\, R^2 / \dot{M} v_\infty \simeq 10^7$ (neglecting clumping, ud-Doula & Owocki 2002), where B_{eq} is the equatorial surface strength of the magnetic dipole component. The rotation parameter $W = v_{\mathrm{eq}}/v_{\mathrm{crit}} = 0.3$ (Ud-Doula, Owocki & Townsend 2008, where we have included a correction for the oblateness of the star due to its rapid rotation). This places the Alfvén radius at $R_{\mathrm{Alf}} = \eta_*^{1/4}\, R_* \simeq 60\, R_*$. In contrast, the Kepler (or corotation) radius is located relatively close to the star, at about $R_{\mathrm{Kep}} = W^{-2/3}\, R_* = 2.2\, R_*$. This geometry, in which $R_{\mathrm{Kep}} << R_{\mathrm{Alf}}$, results in a large spatial volume in which magnetospheric plasma is predicted to be maintained in rigid rotation with the star by the magnetic field, while simultaneously being dynamically supported against gravitational infall due to rapid rotation (Ud-Doula, Owocki & Townsend, 2008).

In principle, this situation provides conditions suitable for significant accumulation of rigidly-rotating stellar wind plasma (diagnosed from optical and UV line emission and variability; e.g. Petit et al. (2011)), as well as a large region over which electrons can be accelerated (thus producing the non-thermal radio emission; e.g. Linsky, Drake & Bastian (1992)).

The phased radio light curves, illustrated in Fig. 2.8, exhibit a number of interesting characteristics. First, it is clear that the radio measurements in Stokes I and V/I vary significantly, and are coherently phased with the rotational period derived from the photometric and magnetic measurements. Comparison of the 3.5 cm and 6 cm polarisation and light curves fully confirm the details of the variations. As described by Lim et al., the flux variation is complex, characterised by strong, broad maxima at phases 0.0 and 0.5 (i.e. the extrema of the longitudinal field), and sharper, somewhat weaker secondary extrema at quadrature phases (i.e. 0.25 and 0.75). The polarisation degree varies approximately sinusoidally, with extrema of ±16% and a mean of zero. The new rotational period derived in Sect. 2.3 brings the phases of the radio

flux and polarisation extrema into good agreement with the longitudinal field and photometric extrema, resolving the $\sim$ 0.05-cycle offset pointed out by Lim, Drake & Linsky (1996). The approximate reflectional symmetry of the light curve in both I and V/I (horizontally, relative to phase 0.0, as well as vertically for Stokes V/I, relative to the $V/I = 0$) is in good qualitative agreement with the derived stellar geometry, in particular the large value of the magnetic obliquity $\beta \simeq 90^{\circ}$, implying that we view geometrically similar regions of both (magnetic) hemispheres during a stellar rotation (see also Fig. 2.5).

Comparing the variations at 3.5 and 6 cm, we find that the amplitudes are nearly identical in both I and V/I. The Stokes I variations may display some small differences in shape, in particular with the central (phase 0.5) peak at 3.5 cm being somewhat shallower and broader than at 6 cm.

The presence of structures in the radio lightcurve attributable to the quadrupolar component of the field is very interesting. While the Alfvén radius for the dipole component falls off as $\eta_*^{1/4}$, for the quadrupole the fall-off is as $\eta_*^{1/6}$ (Ud Doula, Owocki and Townsend 2008). The "quadrupolar Alfvén radius" for HD 133880, computed assuming the magnetic model derived in Sect. 2.6.2, is $R_{\mathrm{Alf,q}} \simeq 21\ R_*$. This implies that the radio emission at both 3.5 and 6 cm forms significantly closer than 20 R_* from the star's surface, if the origin of the radio emission is charged particles in the outflowing stellar wind.

The ultraviolet C IV $\lambda\lambda$1548, 1550 and Si IV $\lambda\lambda$1394, 1402 UV resonance doublets are both sensitive indicators of the stellar wind and its structuring and modulation by the magnetic field (Schnerr & Henrichs, 2008, e.g.). A search of the MAST archive indicates that HD 133880 was unfortunately not observed by the IUE satellite, nor with any other instrument with coverage in this spectral region. On the other hand, our optical spectra contain Hα as well as a number of Paschen series H lines. An examination of Hα reveals weak variability in the inner $\pm$500 km/s of the profile.

In Fig. 2.9 we illustrate the line profile variations that are observed in Hα. Fig. 2.10 shows the phased equivalent width of Hα, along with that measured from the Pa 8590 Å line. A telluric line removal algorithm was applied to each profile before analysis to reduce the variations caused by such features. While particular care has been taken to keep the normalisation of the ESPaDOnS and FEROS spectra as consistent as possible, it is difficult to judge whether the small fluctuations that are found in the far wings are real or an artefact of the normalisation. At phases 0.0 to 0.35 we find that the line cores show excess absorption relative to the average profiles, reaching maximum absorption at phase 0.0. Between phases 0.35 to 0.8, the core region of the Hα profile shows emission relative to the average profile. Unfortunately, our phase sampling is not sufficient to distinguish if these features propagate through the profile, as would be expected from rigidly rotating magnetically confined plasma.
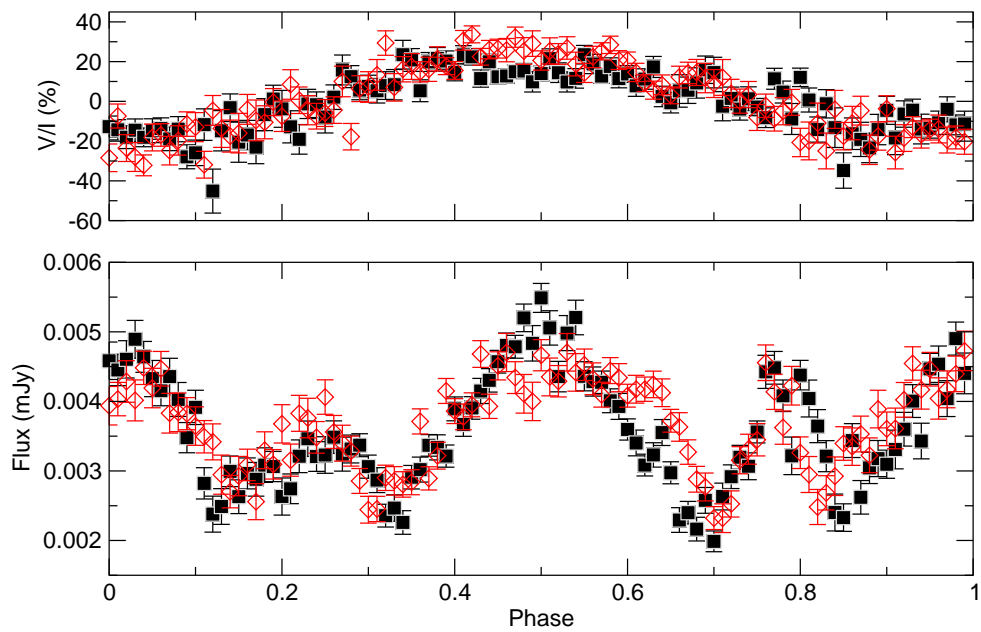
Figure 2.8: **Lower frame:** ATCA Stokes *I* flux variation at 6 cm (filled symbols) and 3 cm (open symbols). **Upper frame:** Stokes *V/I* polarisation at 6 cm (filled symbols) and 3 cm (open symbols).

The Hα profile variability of HD 133880 might be a consequence of modifications of the atmospheric structure due to the strong chemical non-uniformities we have determined to exist in its atmosphere. However, we know that the disc-integrated photospheric He abundance is constrained to be below 10% that of the Sun, i.e. less than 1% of hydrogen by number, at all phases. So even a significant variation of the He abundance could have no important effect on the atmospheric structure.

For the He star a Cen (which has a huge variation of He abundance over its surface and strongly variable metallic lines; Bohlender, Rice & Hechler 2010) Hα varies only in the core of the line (over a region perhaps 2 or 3 times the width of a typical metallic photospheric line) and the variations quite closely mimic the variations observed in the star's iron lines (i.e., the core of Hα gets stronger at the same time as Fe II lines are strong). This may be what we are seeing in HD 133880 as well, since the surface field and metal lines are weakest when Hα is also weakest and most of the variations occur within ±200 km/s of line centre. Given the dominance of the quadrupolar field component, it is possible that the contribution of magnetospheric material to the overall variability of Hα may be reduced somewhat, since material will be trapped in a more complex circumstellar geometry: likely four or more "clouds" rather than the two clouds seen in stars with dominant dipolar fields. For example, the Hα variability of HD 37776, a B-type star with a complex quadrupolar field, is quite modest compared to other stars with more dipolar fields (e.g., σ Ori E; Oksala et al., 2011) despite the fact that it has similar physical properties to the other stars. Therefore, at present we simply conclude that the origin of the H line variations is unclear.

2.10 Discussion

This chapter presents our continuing work in the study of chemical abundance evolution with time of magnetic Ap/Bp stars in open clusters. The goal of this project is to model the magnetic field structure, to derive an estimate of the surface abundance distribution of a number of elements and to provide a preliminary analysis to serve as a foundation for further more detailed modelling. In particular, more spectropolarimetric observations will allow for a more sophisticated interpretation of the surface abundance variations and magnetic field structure via Magnetic Doppler Imaging (MDI; Piskunov & Kochukhov (2002)).

HD 133880 is a very young, rapidly rotating Bp star ($v \sin i \simeq 103$ km s^{-1}) that hosts a strong magnetic field. The magnetic field variations were modelled using a co-linear axisymmetric multipole expansion with i=55° $\pm$ 10°, β=78° $\pm$ 10°, $B_d = -9600 \pm 1000$ G, $B_q = -23200 \pm 1000$ G, and $B_{oct} = 1900 \pm 1000$ G. We used Hipparcos photometric measurements together with our own $\langle B_z \rangle$ measurements, as well as photometric and radio emission data presented
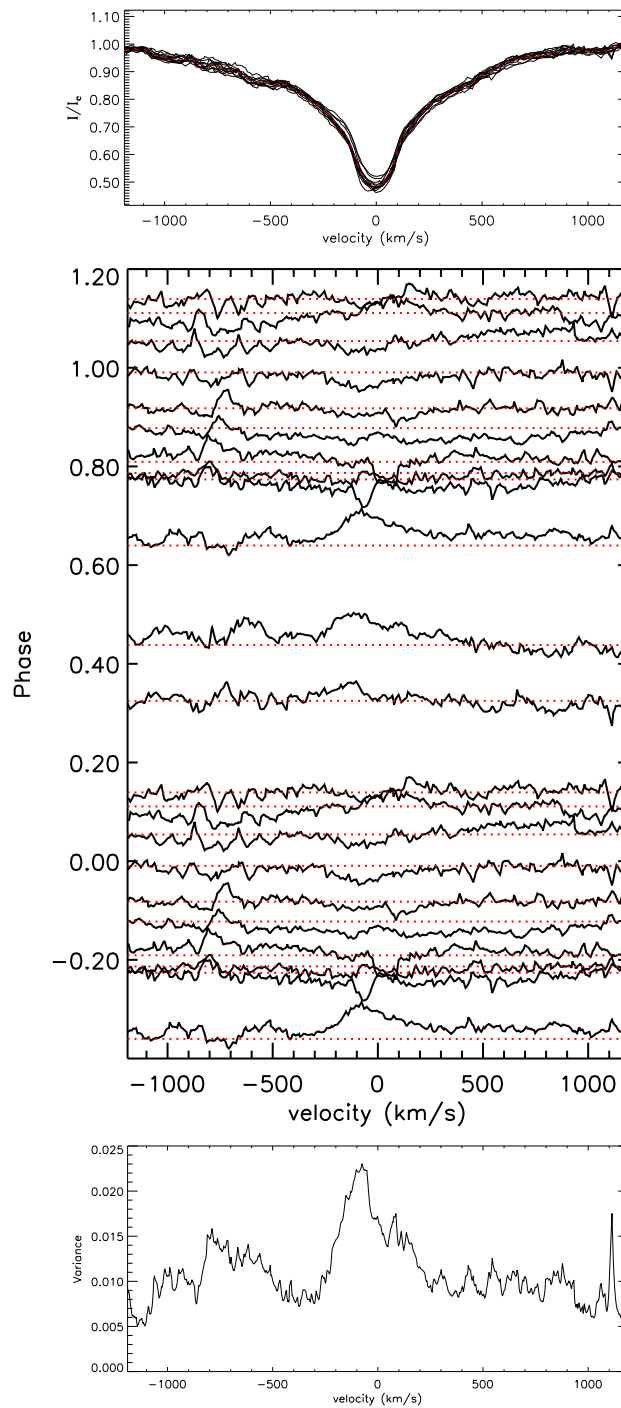
Figure 2.9: **Top:** Observed Hα line profiles with the mean profile indicated as dashed red. **Middle:** Shown are the continuum normalised spectra after subtracting the average of all the Hα line profiles, displayed in such a way that the profiles are plotted at a height that corresponds to the phase of the observation. Also included is a dotted line corresponding to a zero difference to highlight the line profile variations. **Bottom:** Shown is the variance of the continuum normalised spectra from the mean profile.
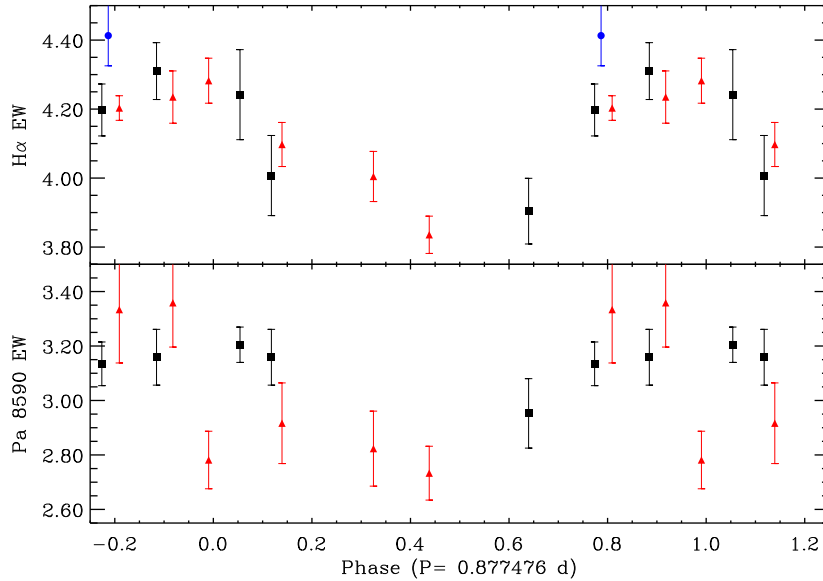
Figure 2.10: Phased equivalent widths measurements of the core region of Hα (top) and the total Paschen line at 8590 Å from the ESPaDOnS (black squares) and FEROS (red triangles) spectra.

by Waelkens (1985) and Lim, Drake & Linsky (1996) respectively, to refine the period to $P = 0.877476 \pm 0.000009$ days. The abundance distributions of He, O, Mg, Si, Ti, Cr, Fe, Ni, Pr, and Nd were modelled using three co-axial rings around the two magnetic poles and the magnetic equator. The Fe-peak elements are overabundant compared to the solar ratios with strong variations on a global scale observed between hemispheres.

We have twelve Stokes I spectra of HD 133880 spread well in phase that sample both magnetic poles and the magnetic equator. Our adopted magnetic field geometry, although an approximation to the actual field structure of HD 133880, and our three co-axial ringed abundance model provides the most detailed abundance analysis possible given the limitations of the model. Most elements studied appear to have a distinctly non-solar abundance in most rings. The abundance of Mg is slightly above solar at both magnetic poles but near solar abundance at the magnetic equator. Upper limits to the abundances of He and Ni were found. HD 133880 is clearly a He-weak star with an abundance at least a factor of 8 lower than the solar ratio. Ni is no more than 10 times overabundant compared to the Sun. All other elements studied (O, Si, Ti, Cr, Fe, Pr, Nd) are more abundant at the negative magnetic pole than the positive magnetic pole. Most interesting are the variations observed in O abundance. Most Ap/Bp stars show O abundances near or below the solar abundance ratios (Sargent & Searle, 1962; Roby & Lambert, 1990). However, a careful study of several O features reveal that oxygen is more abundant than solar at both magnetic poles (most notably at the negative

magnetic pole where O is 0.7 dex overabundant) but a solar abundance near the magnetic equator. This behaviour is certainly uncommon in Bp stars, but is unambiguously determined in this analysis.

In the context of the larger study of the time evolution of atmospheric abundances of Ap/Bp stars, it is interesting to compare to work done by Bailey et al. (2011) on the Ap star HD 318107 (=NGC 6405 77). This star is also hot ($T_{\mathrm{eff}} \simeq 11800$ K), young ($\log t \simeq 7.8$ (yrs)), of comparable mass ($2.95 \pm 0.15\ M_\odot$), and host to a large complex magnetic field ($\langle B_z \rangle$ varies from about 1 to 5 kG). In contrast to HD 133880, it is a slow rotator ($v \sin i \simeq 7$ km s^{-1}) and only one magnetic hemisphere is observed. The global properties of atmospheric abundances is similar between both stars: the mean abundances for Fe-peak (Ti, Cr, Fe) and rare-earth (Nd, Pr) elements are comparable within uncertainties and clearly overabundant compared to the solar ratios. There are, however, notable differences in the abundances of O and Si between both stars. For HD 318107, the O abundance is more typical of Ap stars, being about 0.3 dex lower than the solar value as compared to HD 133880 where O appears to be overabundant. Si is about 1 dex more abundant in HD 133880 compared to HD 318107 which is understandable in that the former has the Si $\lambda 4200$ peculiarity whereas the latter does not.

Folsom et al. (2007) studied the chemical abundances of stars in an older cluster NGC 6475 ($\log t \simeq 8.47$ (yrs)) that have similar masses to HD 133880. Mean abundances for multiple elements in the Ap stars HD 162576 (=NGC 6475 55; $3.0 \pm 0.4\ M_\odot$), HD 162725 (=HR 6663; $3.3 \pm 0.5\ M_\odot$) and HD 162305 (=NGC 6475 14; $2.7 \pm 0.3\ M_\odot$) were derived. As compared to HD 133880 and HD 318107, the abundances of Cr for all three stars are similar, being about 2 dex larger than in the Sun. However, the abundances of Ti and Fe appear to be slightly lower and only 0.5 dex larger than the solar ratios, respectively. This is in contrast to HD 133880 and HD 318107 where Ti and Fe are about 1.5 and 1 dex overabundant compared to the Sun, respectively. A larger dataset is required before any definitive conclusions can be made regarding the time evolution of abundances in Ap stars.

HD 133880 was previously modelled by Landstreet (1990) who characterised the magnetic field variations of this star with measurements of the longitudinal magnetic field from Hβ. Unlike most magnetic Ap/Bp stars whose magnetic field structure is predominantly dipolar, Landstreet (1990) found a magnetic field dominated by the quadrupole component. Despite the large $v \sin i$ of the star, we were able to further characterise the magnetic field of HD 133880. The higher SNR and spectral resolution of the ESPaDOnS spectra made it possible to compare spectral lines of the same element that have a large and small Landé z factor to characterise the surface magnetic field modulus variations, $\langle B \rangle$. By finding a model that characterises the observed $\langle B_z \rangle$ and $\langle B \rangle$ variations, we are able to find the inclination, i, of the line of sight to the rotation axis as well as the tilt angle of the magnetic field axis, β, to the rotation axis. This

Table 2.7: Measurements of $\langle B_z \rangle$ using LSD masks composed of lines of single elements (Si, Ti, Cr, and Fe) from the polarised ESPaDOnS and HARPS spectra (cf Table 2.2).

Phase	$\langle B_z \rangle$(Si) (G)	$\langle B_z \rangle$(Ti) (G)	$\langle B_z \rangle$(Cr) (G)	$\langle B_z \rangle$(Fe) (G)
0.111	-3419 ± 76	-5724 ± 535	-4773 ± 229	-3498 ± 50
0.640	1790 ± 66	2255 ± 304	2653 ± 196	1993 ± 44
0.787	1020 ± 93	-506 ± 308	1026 ± 208	975 ± 78
0.878	-1776 ± 63	-2883 ± 319	-2409 ± 175	-2010 ± 45

model is merely an approximation to the very complex field structure of HD 133880, but is sufficient to provide a meaningful first analysis to the atmospheric abundance distribution of elements.

Figure 2.4 shows clearly the qualitative nature of both the $\langle B_z \rangle$ and $\langle B \rangle$ variations. There is a rapid change in polarity in the $\langle B_z \rangle$ curve with a steep transition from the positive to negative hemisphere. The strong quadrupolar component of the magnetic field causes a distinct non-sinusoidal variation with the field structure flattening out near the positive magnetic pole. The fact that there is a clear pole reversal indicates that the sum of the inclination and magnetic field axis must be greater than 90°: $i + \beta > 90°$, and that the line-of-sight goes well into both magnetic hemispheres. The parameters of the adopted magnetic field geometry are presented in Sect. 2.6.2. $\langle B_z \rangle$ measurements using all metallic lines (see Table 2.2) agree well with the measurements by Landstreet (1990) using Hβ, suggesting that they sample the magnetic field in similar ways (see Fig. 2.4). Longitudinal field $\langle B_z \rangle$ measurements of spectral lines of only a single element provide clues to the inhomogeneous structure of the magnetic field and the surface distribution of elements. Using all four of our polarimetric observations, we have remeasured the longitudinal field $\langle B_z \rangle$ using spectral lines of Si, Ti, Cr, and Fe. The results are listed in Table 2.7.

It is clear from Table 2.7 that all four elements sample the field in different ways. The differences in measured field strengths can be attributed to the complex magnetic field (as reported by Landstreet (1990) and discussed in this thesis) and the inhomogeneous surface distribution of elements which is a common feature of Bp stars. Near the positive magnetic pole (phase 0.537) at phase 0.640, as well as phase 0.878, the measured $\langle B_z \rangle$ values for all four elements differ significantly. In the negative magnetic hemisphere (near phase 0.037) Si and Fe sample the field in similar ways, whereas Cr and Ti sample the magnetic field differently with $\langle B_z \rangle$ measurements approximately 1 and 2 kG stronger than Si and Fe. Along the sharp decline from the positive to negative magnetic pole (near phase 0.787; see Figure 2.4), it appears that only Ti differs greatly showing a polarity reversal as compared to the other elements at the

same phase.

The measurements of the longitudinal field using different elements reveal that particular elements at different phases sample the field in very distinctive ways, which suggests a truly complex magnetic field that cannot be accurately modelled by a simple axisymmetric magnetic field (such as the one adopted in this thesis and by Landstreet (1990)). It also strongly suggests an inhomogeneous distribution of various elements on the stellar surface that substantially affect the magnetic field measurements. We also compared the computed to the observed Stokes V profiles for the three polarimetric ESPaDOnS spectra for multiple lines (Mg, Si, Ti, Cr, and Fe). The agreement is poor, with the computed Stokes V profiles being much stronger than the observed, further suggesting that our adopted magnetic field model is only a rough approximation. This result is not unique. A recent paper by Kochukhov et al. (2011a) on HD 37776 (=HIP 26742) reveal that the complex multipole model derived from the longitudinal field predicts Stokes V signatures that are much too strong compared to the observed Stokes V profiles. In this case, the multipole magnetic field model (similar in structure to the one used for HD 133880) predicts a large surface field, whereas the Magnetic Doppler Imaging (MDI) results produce a much more modest surface field. This is also seen, although less severely, for σ Ori E (Oksala et al., 2011). For this star, detailed analysis using MDI produced a magnetic field model that closely resembled the observed Stokes V profiles. The acquisition of new, high SNR polarimetric observations of HD 133880 are necessary to characterise unambiguously the surface abundance variations and magnetic field structure using MDI.

The very strong field and rapid rotation of HD 133880 produce interesting magnetospheric characteristics. In our preliminary analysis, we were not able to conclude that the optical spectra contain detectable information about the magnetosphere. However, HD 133880 is one of only a few Bp stars for which radio flux variations have been noted. There are small but distinct differences between the 3 cm and 6 cm radio emission, such as the systematically lower 3 cm than 6 cm fluxes at phases 0.0 and 0.5. The 3 cm emission suggests a "bump" at about phase 0.6 and the peak at about phase 0.75 is narrower at 3 cm than at 6 cm. The fact that the radio spectrum is flat between 6 and 3 cm suggests that the emission is optically thick, and therefore we are observing the magnetosphere at two different radio surfaces rather than an integration throughout the entire volume. These subtle differences in the radio light curves at 6 and 3 cm then imply that these two surfaces cannot have exactly the same shapes and that, presumably, the magnetic field is not perfectly axisymmetric. HD 133880 is a very exciting target for more detailed magnetospheric modelling.

Bibliography

Asplund M., Grevesse N., Sauval A. J., Scott P., 2009, ARA&A, 47, 481

Bagnulo S., Landstreet J. D., Mason E., Andretta V., Silaj J., Wade G. A., 2006, A&A, 450, 777

Bailey J. D., Landstreet J. D., Bagnulo S., Fossati L., Kochukhov O., Paladini C., Silvester J., Wade G., 2011, A&A, 535, A25

Becker S. R., Butler K., 1990, A&A, 235, 326

Bohlender D. A., Rice J. B., Hechler P., 2010, A&A, 520, A44

Borra E. F., Landstreet J. D., 1975, PASP, 87, 961

Castor J. I., Abbott D. C., Klein R. I., 1975, ApJ, 195, 157

Donati J.-F., Semel M., Carter B. D., Rees D. E., Collier Cameron A., 1997, MNRAS, 291, 658

Folsom C. P., Wade G. A., Bagnulo S., Landstreet J. D., 2007, MNRAS, 376, 361

Harmanec P., 1998, A&A, 335, 173

Hauck B., Kunzli M., 1996, Baltic Astronomy, 5, 303

Hauck B., North P., 1993, A&A, 269, 403

Hill G. M., 1995, A&A, 294, 536

Kaufer A., Stahl O., Tubbesing S., Nørregaard P., Avila G., Francois P., Pasquini L., Pizzella A., 1999, The Messenger, 95, 8

Kochukhov O., Lundin A., Romanyuk I., Kudryavtsev D., 2011a, ApJ, 726, 24

Kochukhov O. et al., 2011b, A&A, 534, L13

Kunzli M., North P., Kurucz R. L., Nicolet B., 1997, A&AS, 122, 51

Kupka F., Piskunov N. E., Ryabchikova T. A., Stempels N. C., Weiss W. W., 1999, A&A, 138, 119

Kupka F. G., Ryabchikova T. A., Piskunov N. E., Stempels H. C., Weiss W. W., 2000, Baltic Astronomy, 9, 590

Kurucz R. L., 1979, ApJS, 40, 1

Landstreet J. D., 1988, ApJ, 326, 967

Landstreet J. D., 1990, ApJL, 352, L5

Landstreet J. D., Bagnulo S., Andretta V., Fossati L., Mason E., Silaj J., Wade G. A., 2007, A&A, 470, 685

Landstreet J. D., Barker P. K., Bohlender D. A., Jewison M. S., 1989, ApJ, 344, 876

Landstreet J. D., Mathys G., 2000, A&A, 359, 213

Landstreet J. D. et al., 2008, A&A, 481, 465

Lim J., Drake S. A., Linsky J. L., 1996, in Astronomical Society of the Pacific Conference Series, Vol. 93, Radio Emission from the Stars and the Sun, A. R. Taylor & J. M. Paredes, ed., pp. 324–+

Linsky J. L., Drake S. A., Bastian T. S., 1992, in Astronomical Society of the Pacific Conference Series, Vol. 26, Cool Stars, Stellar Systems, and the Sun, M. S. Giampapa & J. A. Bookbinder, ed., pp. 325–+

Makaganiuk V. et al., 2011, eprint arXiv:1111.6065

Moon T. T., Dworetsky M. M., 1985, MNRAS, 217, 305

Napiwotzki R., Schoenberner D., Wenske V., 1993, A&A, 268, 653

Netopil M., Paunzen E., Maitzen H. M., North P., Hubrig S., 2008, A&A, 491, 545

Oksala M. E., Wade G. A., Marcolino W. L. F., Grunhut J. H., Bohlender D., Manset N., Townsend R. H. D., Townsend, 2011, in IAU Symposium, Vol. 272, IAU Symposium, C. Neiner, G. Wade, G. Meynet, & G. Peters, ed., pp. 204–205

Owocki S., Townsend R., Ud-Doula A., 2006, in 36th COSPAR Scientific Assembly, Vol. 36,
    pp. 3548–+

Petit V., Wade G. A., Alecian E., Drissen L., Montmerle T., ud-Doula A., 2011, in IAU Sym-
    posium, Vol. 272, IAU Symposium, C. Neiner, G. Wade, G. Meynet, & G. Peters, ed., pp.
    208–209

Piskunov N., Kochukhov O., 2002, A&A, 381, 736

Piskunov N. E., Kupka F., Ryabchikova T. A., Weiss W. W., Jeffery C. S., 1995, A&A, 112,
    525

Piskunov N. E., Valenti J. A., 2002, A&A, 385, 1095

Press W. H., Flannery B. P., Teukolsky S. A., 1986, Numerical recipes. The art of scientific
    computing, Press, W. H., Flannery, B. P., & Teukolsky, S. A., ed.

Preston G. W., 1971, ApJ, 164, 309

Roby S. W., Lambert D. L., 1990, ApJS, 73, 67

Ryabchikova T. A., 1991, in IAU Symposium, Vol. 145, Evolution of Stars: the Photospheric
    Abundance Connection, G. Michaud & A. V. Tutukov, ed., pp. 149–+

Ryabchikova T. A., Piskunov N. E., Kupka F., Weiss W. W., 1997, Baltic Astronomy, 6, 244

Sargent W. L. W., Searle L., 1962, ApJ, 136, 408

Schnerr R. S., Henrichs H. F., 2008, in Clumping in Hot-Star Winds, W.-R. Hamann, A. Feld-
    meier, & L. M. Oskinova, ed., pp. 143–+

Stepien K., Dominiczak R., 1989, A&A, 219, 197

ud-Doula A., Owocki S. P., 2002, ApJ, 576, 413

Ud-Doula A., Owocki S. P., Townsend R. H. D., 2008, MNRAS, 385, 97

Wade, G. A., Donati, J. F., Landstreet, J. D., Shorlin, S. L. S. 2000, MNRAS, 313, 851

Wade G. A., Bagnulo S., Kochukhov O., Landstreet J. D., Piskunov N., Stift M. J., 2001, A&A,
    374, 265

Waelkens C., 1985, A&AS, 61, 127

Chapter 3

The surface chemistry of the magnetic Bp star HD 147010

3.1   Introduction

The classes of main sequence A- and B-type stars are hosts to a variety of atmospheric stellar phenomena. Perhaps the most striking sub-class are the magnetic peculiar A- and B-type stars (Ap/Bp). These stars became the focus of intense research when Babcock (1960) discovered a 34 kG magnetic field in HD 215441 (= Babcock's Star); however, the existence of these stars was evident prior to this discovery. The mAp/Bp stars are characterised by large, global magnetic fields (of order 1 kG or more) that are roughly dipolar in nature. These fields are long-lived and vary with the rotation period of the star, which is generally between about 1 and 10 days. This variability is described in the context of the oblique rigid rotator model: the rotation axis is tilted at an angle i to the line-of-sight and the magnetic field is at an angle β to the rotation axis. In this framework, as the star rotates, different portions of the magnetic field are observed. Spectroscopic studies indicate that magnetic Ap/Bp stars possess anomalous atmospheric abundances of Fe-peak and rare-earth elements. Specifically, Cr can be as much as 10^2 in excess of the solar abundance ratio and, more drastically, Pr and Nd are often times more than 10^4 times more abundant than in the Sun. The magnetic field serves to lock these elements in place on the surface of the star, which makes possible a long-lived patchy distribution that is often distributed non-axisymmetrically about the rotation axis. This results in variations in spectral line profiles that also vary with the rotation period of the star (Ryabchikova, 1991).

   HD 147010 (= HIP 80024) is a magnetic Bp star with an effective temperature $T_{\text{eff}} = 13000 \pm 500$ K (Bailey & Landstreet, 2013), luminosity log $L/L_\odot = 1.92$ and mass $M/M_\odot = 3.15 \pm$

0.20 (Landstreet et al., 2007). This star is a member of the Upper Scorpius-Centaurus Association, meaning it is a young star with an age of log $t = 6.70 \pm 0.10$ (Landstreet et al., 2007, 2008).

The rotation period of HD 147010 was measured using Geneva photometry by North (1984) who found a period of $P = 3.9210 \pm 0.0001$ days. This value was later refined by Lanz & Mathys (1991) to $P = 3.92076$ days.

Thompson, Brown & Landstreet (1987) obtained twelve line-of-sight magnetic field $\langle B_z \rangle$ measurements from Hβ for HD 147010. They found that the magnetic field varies from about -6 to -3 kG, noting that only the negative magnetic hemisphere is observed. They also deduced that the star rotates with $v \sin i \sim 20$ km s^{-1}. Later, Mathys & Lanz (1992) were able to resolve Zeeman splitting in Fe II at 6149 Å at some phases. They found the surface magnetic field $\langle B \rangle$ to be of the order of 13 or 14 kG. Mathys (1994, 1995) measured $\langle B_z \rangle$ variations from metal lines, finding that the magnetic field varies between about -2000 and -5000 G and that $v \sin i = 22.1 \pm 4$ km s^{-1}. A more recent study of B-type stars by Bailey & Landstreet (2013) provided a preliminary reconnaissance of the surface chemistry of the even-Z iron peak elements (Ti, Cr, Fe) finding they are between 10 to 10^2 times more abundant than in the Sun. They also refined the projected rotation velocity of the star, finding $v \sin i = 15 \pm 2$ km s^{-1}.

This chapter aims to characterise the magnetic field and surface chemistry of HD 147010 using recently obtained spectropolarimetric observations from CFHT's ESPaDOnS. Sect. 3.2 provides a brief overview of the observations used and discusses measurements of the magnetic field; Sect. 3.3 discusses the rotation period; Sect. 3.4 describes the adopted magnetic field geometry; Sect. 3.5 outlines the spectral synthesis technique; Sect. 3.6 describes the surface abundance distribution; and Sect. 3.7 discusses the results.

3.2   Observations

Seven new spectra of HD 147010 were obtained for this project using ESPaDOnS, a cross-dispersed echelle spectropolarimeter located at the Canada-France-Hawaii Telescope (CFHT). A total of five of the observations are polarimetric with observations of both Stokes I and V, obtained with a resolving power of R $\sim$ 65000. The remaining two spectra are unpolarised, with just Stokes I measurements and R $\sim$ 80000. All measurements cover a spectral range from about 3690 - 10481 Å.

The dataset is summarised in Table 3.1, which lists the heliocentric Julian Date (HJD) at the middle of the observation, spectral range and observed stellar radial velocity (RV). The

Table 3.1: Log of ESPaDOnS observations of HD 147010. For each spectra the HJD, derived phases, $\langle B_z \rangle$ measurements and $\langle B \rangle$ values measured from Fe II λ6149 and Nd III λ6145 are listed.

HJD	Phase	$\langle B_z \rangle$ (G)	$\langle B \rangle$ (G) Fe II λ6149	$\langle B \rangle$ (G) Nd III λ6145	Window (Å)	RV (km s^{-1})
2455411.792	0.387	-4906 ± 37	11100 ± 420	11600 ± 570	3690-10481	-5
2455412.743	0.629	–	14500 ± 630	15900 ± 280	3690-10481	-6
2455414.738	0.138	–	11700 ± 210	11300 ± 280	3690-10481	-5
2455961.094	0.489	-4647 ± 33	12200 ± 420	11900 ± 570	3690-10481	-5
2455967.113	0.025	-4540 ± 31	13400 ± 420	14200 ± 380	3690-10481	-4
2456099.960	0.908	-2917 ± 36	15700 ± 520	16400 ± 380	3690-10481	-4
2456100.860	0.138	-4980 ± 42	12000 ± 320	12500 ± 570	3690-10481	-5

remaining columns are discussed in more detail below. The RV is measured from fitting a model synthetic spectrum to the observations during the abundance analysis (see below). The uncertainty is estimated from the observed scatter of multiple ~30 Å windows to be of the order of 1 km s^{-1}.

3.2.1   Longitudinal magnetic field strength measurements

Measurements of $\langle B_z \rangle$ were obtained from the ESPaDOnS V spectra using Least Squares Deconvolution (LSD; see Donati et al., 1997). The technique involves obtaining a mean line profile by combining all metallic and He lines in the spectrum. The advantage to this technique is a much higher signal-to-noise ration (SNR), which improves the ability to detect Zeeman signatures due to magnetic fields. The atomic data is obtained from the Vienna Atomic Line Database (VALD; see Kupka et al., 2000; Ryabchikova et al., 1997; Piskunov et al., 1995; Kupka et al., 1999). The VALD line list chosen has the appropriate T_{eff} and $\log g$ as well as enhanced Fe-peak and rare-earth elements typical of magnetic Ap/Bp stars. The $\langle B_z \rangle$ value is then computed using the first-order moment of the V profile (e.g. Landstreet et al., 2008)

$$\langle B_z \rangle = -2.14 \times 10^{12} \frac{\int v V(v) \mathrm{d}v}{\lambda z c \int [I_{\text{c}} - I(v)] \mathrm{d}v}, \tag{3.1}$$

where $\langle B_z \rangle$ is in G, z is the mean Landé factor, and λ is the mean wavelength of the weighted LSD line in Å. The limits of integration were chosen by visual inspection of the mean LSD profile to ensure that the entire signal was measured with the introduction of minimal noise
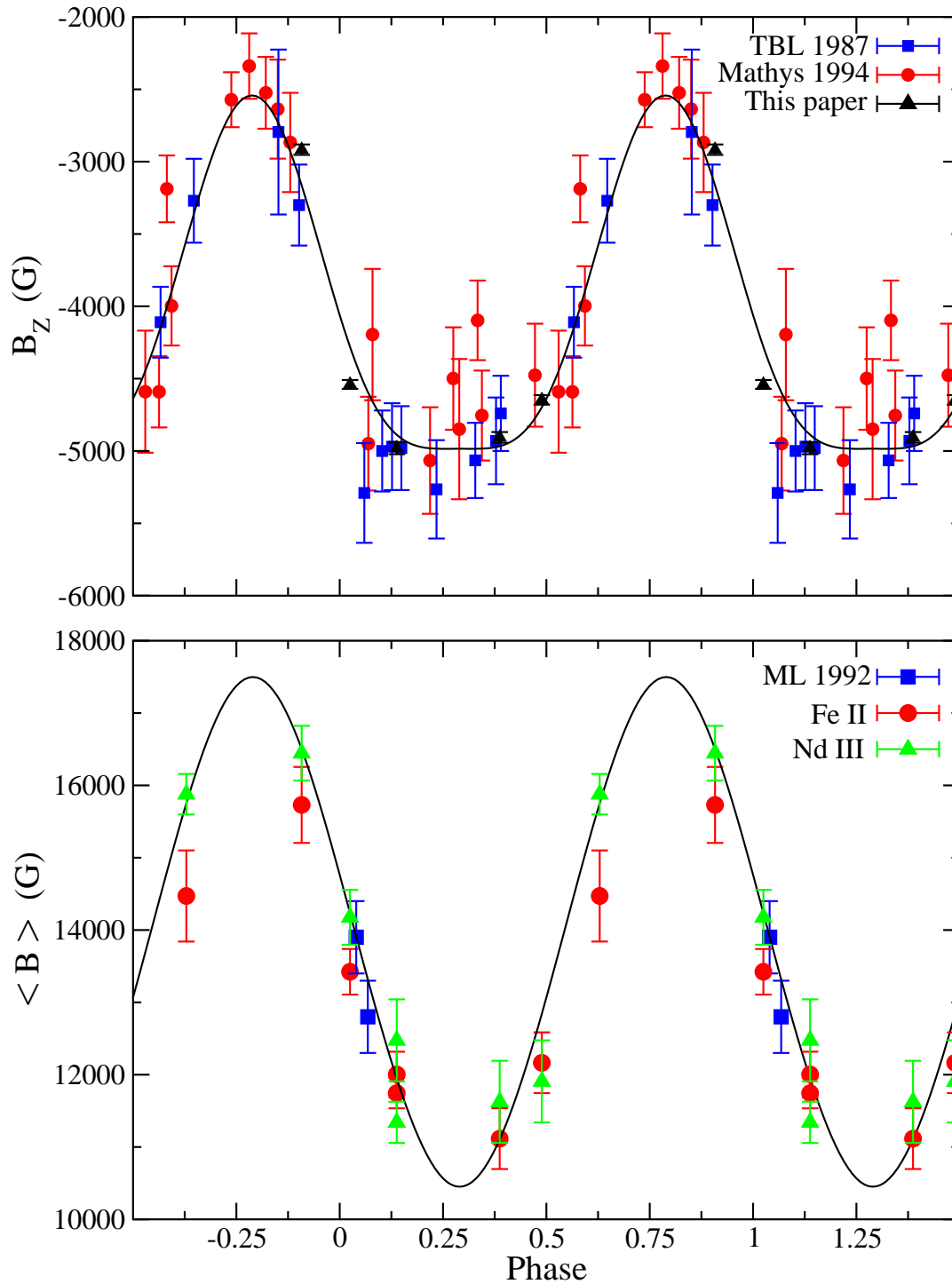
Figure 3.1: The top plot shows the $\langle B_z \rangle$ field variations in HD 147010. The data points in black (triangles) are the ESPaDOnS data from Table 3.1. The data points in blue (squares) and red (circles) are measurements from Thompson, Brown & Landstreet (1987) and Mathys (1994), respectively, translated vertically to align with the ESPaDOnS data. The bottom plot depicts the $\langle B \rangle$ field variations. The data points in blue (squares) are from Mathys & Lanz (1992) shifted to the current phase system. The points in red (circles) and green (triangles) are measurements from the ESPaDOnS data from Table 3.1 for both Fe II λ 6149 and Nd III λ 6145, respectively. In both panels, the solid black curve denotes the $\langle B_z \rangle$ (top) and $\langle B \rangle$ (bottom) rotational variations predicted by our adopted field geometry.

from the continuum. Formal errors were computed by propagating the uncertainties through equation 3.1. The $\langle B_z \rangle$ measurements are listed in Table 3.1.

3.2.2 Surface magnetic field strength measurements

The large magnetic field and small $v \sin i$ in combination with the high resolving power of ESPaDOnS make it possible to resolve Zeeman split components in many spectral lines. We have made $\langle B \rangle$ measurements using the split components observed in Fe II λ6149 and Nd III λ6145. The value of $\langle B \rangle$ was evaluated using the expression

$$\langle B \rangle \; = \; \frac{\Delta\lambda}{4.67 \times 10^{-13} \lambda_o^2 z}, \tag{3.2}$$

where $\Delta\lambda$ is the shift of the σ component from the zero field wavelength, λ_o is the rest wavelength and z is the mean Landé factor. To measure these values, we employed the same techniques as discussed by Bailey et al. (2011). In summary, for each split component, multiple measurements of the location of the split components were made by repeatedly fitting Gaussians to each split component to determine $\Delta\lambda$. In all cases, the corresponding $\Delta\lambda$ was determined to within ± 0.02 Å or less. As noted by Bailey et al. (2011), the measurements of $\langle B \rangle$ are extremely sensitive to changes in $\Delta\lambda$. Therefore, for phases in which the components were not resolved well enough to obtain an unambiguous measurement of $\langle B \rangle$, the measured values were compared to the computed field $\langle B \rangle$ necessary to produce the observed splitting via the Fortran program ZEEMAN (see Sect. 3.5). In all cases, the modelled $\langle B \rangle$ values agreed with the measured values from both lines within the estimated uncertainties. Therefore, we are confident that the observed measurements are accurate. The $\langle B \rangle$ values measured from both Fe II and Nd III lines are listed in Table 3.1.

3.3 Rotation period

North (1984) used Geneva photometry taken between April and June of 1983 to refine the period of HD 147010 to 3.9210 ± 0.0001 days. Measurements of the $\langle B_z \rangle$ variations from Hβ by Thompson, Brown & Landstreet (1987) were shown to be fit well by the photometric ephemeris of North (1984). Later photometric data taken by Lanz & Mathys (1991) allowed the period of HD 147010 to be further refined to $P = 3.92076$ days. Mathys (1994) made $\langle B_z \rangle$ measurements from metallic lines which revealed no obvious inconsistencies with the measurements by Thompson, Brown & Landstreet (1987). However, he noted that the $\langle B_z \rangle$ measurements from Mathys (1994) and Thompson, Brown & Landstreet (1987) were systematically offset

from one another with the former varying from about -4.3 to -1.9 kG and the latter from -5.8 to -3.2 kG. Our recent data, which consists of five new polarimetric observations, are further offset to both the data from Mathys (1994) and Thompson, Brown & Landstreet (1987). This is not surprising given the different techniques used for measuring the magnetic field. Regardless of this offset, we note that the recent data have a phase uncertainty of about 0.14 relative to the older data. Therefore, our new $\langle B_z \rangle$ and $\langle B \rangle$ data, as well as the I spectra we wish to use to model abundances, need to be accurately phased with the older measurements.

Fortunately, we have $\langle B_z \rangle$ measurements spanning 25 years that we can use to try and improve the period. Our new data only consists of five measurements, but may sample a sufficient range in phase to re-analyse the period by comparison to the older field measurements. As noted above, the historic data is offset to the newer ESPaDOnS measurements. Since the qualitative behaviour of the field is consistent between different epochs, we decided to renormalise both the $\langle B_z \rangle$ measurements from Mathys (1994) (-500 G) and Thompson, Brown & Landstreet (1987) ($+850$ G) to match the newer ESPaDOnS data. Regrettably, the choice of the best-fit period from the magnetic data is not entirely straightforward because of the poor spacing of observations. Utilising the period found by North (1984) as a starting point, we iteratively searched for the best-fit period in a reasonable range around this value. The best fit is judged by the reduced χ^2 fit to the $\langle B_z \rangle$ variations comparing the older to newer data. Given the inherent difficulty in deriving this value from the $\langle B_z \rangle$ data, we adopt an uncertainty that appears to fit all the data reasonably well. In this fashion, we prefer a period of P = 3.9207 $\pm$ 0.0003 days using the same zero point from Mathys (1994) of JD 2446894.515. Apparently, the present dataset is not sufficient to improve the precision of the period of HD 147010. However, it is clear that minor adjustments to the period deduced by North (1984) fit the magnetic data well. All the phases are reported in this new phase system.

Fig. 3.1 shows the $\langle B_z \rangle$ variations in the top panel with the measurements by Thompson, Brown & Landstreet (1987) and Mathys (1994) shifted vertically to coincide with the ESPaDOnS data. It is clear from this figure that the variations reported for previous $\langle B_z \rangle$ measurements are in satisfactory agreement with our data. In the bottom panel, the $\langle B \rangle$ measurements made from both Fe II and Nd III are shown using the new period. Also shown are two $\langle B \rangle$ measurements made by Mathys & Lanz (1992). It is clear that the older measurements are consistent with the newer ones. Further, $\langle B \rangle$ measurements made from both lines agree within their respective uncertainties with one exception at phase 0.629.

3.4   Adopted magnetic field geometry

Based on the observed variations of $\langle B_z \rangle$ and $\langle B \rangle$, we can derive an appropriate magnetic field model to use that can adequately reproduce the observed variations, as well as produce, reasonably well, the observed Zeeman splitting at all phases such that the computed spectral line profiles match well the observed Stokes I profiles. We note that the field model was determined using the $\langle B_z \rangle$ scale from the ESPaDOnS data.

From the observed variations of $\langle B_z \rangle$ it is clear that only the negative magnetic hemisphere of HD 147010 is observed. Therefore the sum of i, the angle of the line-of-sight to the rotation axis, and β, the angle of the magnetic field axis to the rotation axis, must be less than about 90°: $i + \beta < 90°$. The detailed magnetic field geometry was obtained using the Fortran program FLDSRCH (see Bailey et al., 2011, 2012). The program allows, as input, values of $\langle B_z \rangle$ and $\langle B \rangle$ at four observational phases and provides as output the reduced χ^2 fit for various combinations of values of i, β, magnetic dipole (B_d) , quadrupole (B_q), and octupole (B_{oct}).

The best-fit model for the magnetic field geometry was found to be $i = \beta = 39°$, $B_d = -21300$ G, $B_q = 30300$ G, and $B_{oct} = -800$ G. The predicted $\langle B_z \rangle$ and $\langle B \rangle$ variations using this model are plotted in Fig. 3.1 and are in very good agreement with both the measured $\langle B_z \rangle$ and $\langle B \rangle$ variations. The abundance analysis presented below is performed using this field geometry.

3.5   Spectrum Synthesis

To perform abundance analysis, the spectrum synthesis program ZEEMAN was used (Landstreet, 1988; Bailey et al., 2011, 2012). ZEEMAN allows as input an assumed magnetic field geometry for stars with magnetic fields, such as the magnetic Ap/Bp stars. The program assumes LTE line formation and uses the ATLAS 9 models to interpolate an appropriate stellar atmospheric model based on the T_{eff} and $\log g$ provided by the user. Emergent spectra are computed for all four Stokes' parameters and up to 10 phases of observed Stokes I spectra can be fit simultaneously, but only one element can be varied at a time. For each iteration, ZEEMAN optimises the $v \sin i$ and radial velocity. Up to 6 rings of uniform abundance can be specified on the surface of the star that have equal spans in co-latitude, which effectively provides a simple map of abundance variations from one magnetic pole to another.

In the case of HD 147010, only one magnetic hemisphere is observed with a span in magnetic latitude of about 80°. The strength of the spectral lines for some elements vary visibly over this range, while others only modestly. After some experimentation, it was determined that a four ring model that each span 45° in co-latitude, with only the two rings in the observed magnetic hemisphere (ranging from 0 to 90°) being varied, provides convergent results that
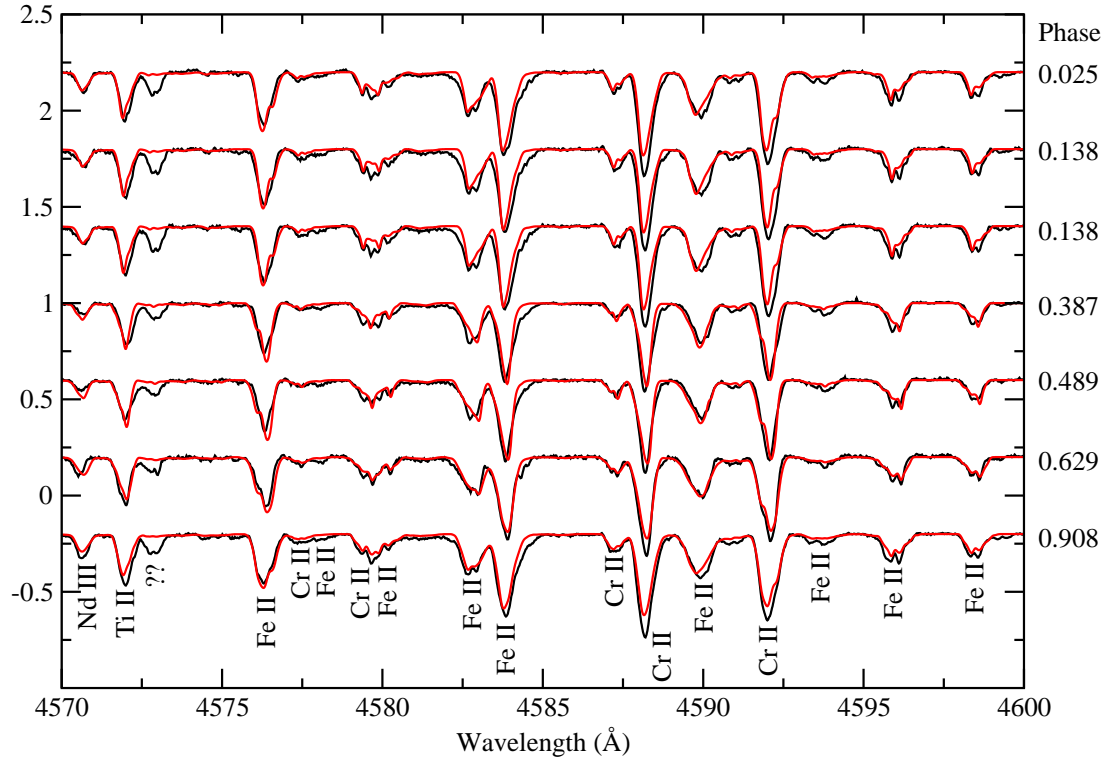
Figure 3.2: Spectrum synthesis of the region 4570 - 4600 Å using the four ring model. The observed spectra are in black and the model fits are in red. The phases are listed beside each spectrum. The line-of-sight is closest to the negative magnetic pole and magnetic equator at about phase 0.3 and 0.8, respectively.

adequately describe the observed variations. Unfortunately, our dataset does not include spectra directly around the magnetic equator (about phase 0.7 to 0.9), however the I spectra that we have are spaced well enough in phase such that we have multiple spectra in each ring. No abundances can be constrained in the positive magnetic hemisphere; therefore, the rings in that hemisphere were set to the average abundance of the first two rings and were determined to not influence the abundances derived in the negative magnetic hemisphere. For the abundance analysis, we use $T_{\text{eff}} = 13000$ K and $\log g = 4.4$ as determined from photometry by Bailey & Landstreet (2013)

3.6 Derived abundances

The large wavelength coverage of the ESPaDOnS data made it possible to achieve a first approximation to the abundance distribution of fifteen elements including He, O, Mg, Al, Si, Ca,
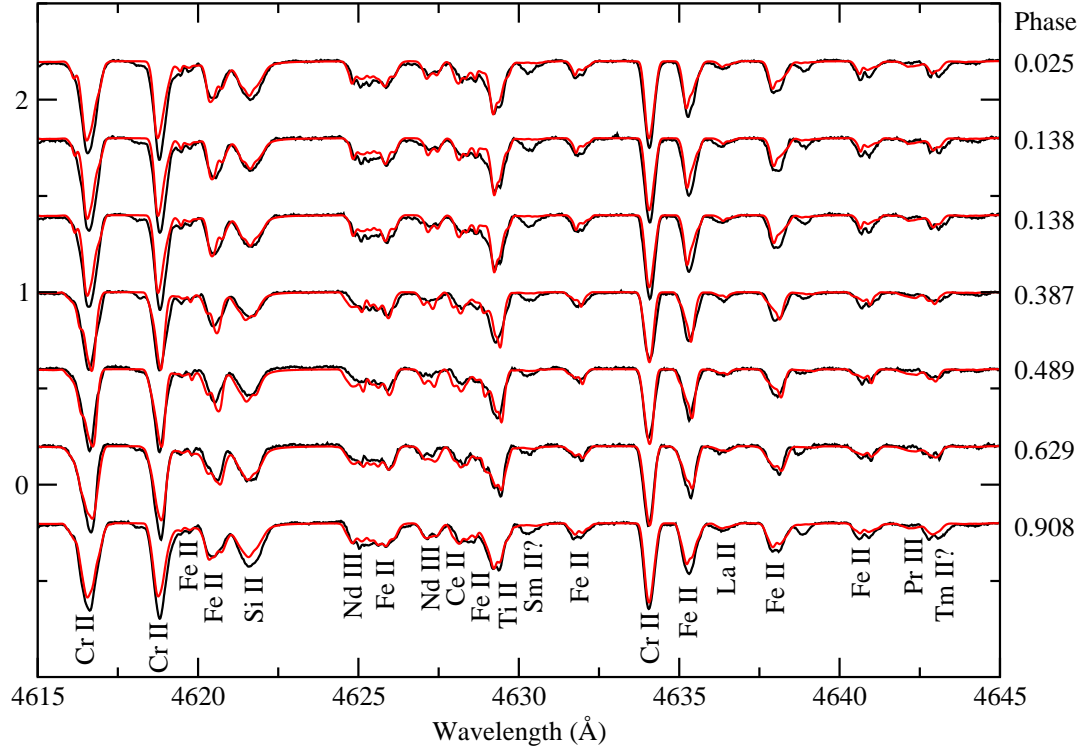
Figure 3.3: Same as Fig. 3.2 for the region 4615 - 4645 Å.

Ti, Cr, Fe, Ni, Sr, La, Ce, Pr, and Nd, as well as an upper limit for Sm. For the majority of the elements studied, multiple lines with a variety of strengths were found.

The abundances for each element in each ring are recorded in Table 3.2. Inaccuracies in the adopted magnetic field geometry forced ZEEMAN to deduce abundance variations at the magnetic pole and equator that were not realistic for three elements: He, Al and Ni. Only one weak line for these elements was adequate to model (except for Al which has two weak lines) and a convergent result was not possible using the multi-ring model. Therefore, a uniform abundance over the entire hemisphere was adopted. This is indicated in Table 3.2 by an asterix. The second to last and last columns list the estimated uncertainties in the derived abundances and the solar abundance ratios as determined by Asplund et al. (2009), respectively. For elements for which more than one spectral line is available, the deviation in the derived abundances between spectral lines was used as the estimated uncertainty. For those in which only one spectral line was available, we changed the abundance until an unsatisfactory fit was achieved and adopted that deviation as our uncertainty. The quality of fits are demonstrated in Fig. 3.2 and Fig. 3.3 with a comparison of the model fits to the seven observed Stokes I spectra. Each individual element is discussed in detail below.

Table 3.2: Abundance distribution of elements studied.

Element	$0 - 45°$	$45 - 90°$	σ	Solar
		$\mathrm{Log}(n_X/n_H)$		
He*	-3.22	-3.22	±0.30	-1.07
O	-4.75	-4.29	±0.20	-3.31
Mg	-5.87	-5.60	±0.15	-4.40
Al*	-5.24	-5.24	±0.20	-5.55
Si	-4.50	-3.01	±0.30	-4.49
Ca	-6.22	-6.24	±0.20	-5.66
Ti	-6.13	-5.40	±0.15	-7.05
Cr	-4.58	-3.93	±0.15	-6.36
Fe	-3.72	-3.19	±0.20	-4.50
Ni*	-5.65	-5.65	±0.20	-5.78
Sr	-7.97	-5.98	±0.30	-9.13
La	-6.14	-5.68	±0.20	-10.90
Ce	-6.25	-6.17	±0.30	-10.42
Pr	-6.85	-5.95	±0.20	-11.28
Nd	-7.88	-5.82	±0.25	-10.58
Sm	< -6.40	$-$	$-$	-11.04

Notes. (*) indicates that a uniform abundance
over the observed stellar surface was adopted.

3.6.1 Distribution of helium

Multiple lines of He I are observable in the available spectra such as the lines at 4471, 4713 and 5876 Å. Of these lines, only upper limits could be determined from $\lambda\lambda$ 4471 and 4713. The cleanest and strongest of these lines was He I at 5876 Å, which therefore was used to determine the helium abundance distribution. The derived values were then tested using the other two lines and found to be in good agreement. At all phases, He is at least 2 dex less than the solar value, confirming that HD 147010 is a He-weak star.

3.6.2 Distribution of oxygen

The oxygen lines at 6155-56-58 Å are very weak and not unambiguously detected. Therefore, we turn to the triplet at 7771-74-75 Å. All the lines are well modelled and, assuming no non-LTE effects in these lines, the oxygen abundance is unambiguously determined. Studies done by Gerbaldi et al. (1989) and Przybilla et al. (2000) clearly indicate that non-LTE effects are present in this triplet; however, the extent of the non-LTE corrections necessary are still very uncertain. We note that the abundance distribution derived from the 7771-74-75 Å triplet fit well the upper limit that can be derived from the 6155-56-58 Å lines, but point out that the actual abundance is likely more underabundant compared to the Sun than what Table 3.2 suggests. The abundance of oxygen varies modestly over the stellar surface possibly being slightly more abundant at the magnetic equator compared to the magnetic pole. However, the abundance does not deviate drastically from a fairly uniform abundance distribution (about 3 times more abundant at the magnetic equator) and is at least 1 dex less than the solar abundance ratio.

3.6.3 Distribution of magnesium

Magnesium was modelled using the line at 4481 Å. At all phases, this line is well fit with a roughly uniform abundance distribution (within estimated uncertainties) implying that Mg is about 1.2 dex less abundant than in the Sun.

3.6.4 Distribution of aluminum

The abundance of Al was derived from two clean lines of Al II at 6226 and 6230 Å. Other lines of Al II were found at 3900 and 5953 Å. The abundance distribution is approximately uniform

over the observed stellar surface and about 0.3 dex more abundant than in the Sun. The line is modelled reasonably well at all phases.

3.6.5　Distribution of silicon

Several lines of Si ɪɪ are observable in the spectra including 4128, 4130, 4621, 5041, 5056, 5957, and 5978 Å. Three lines of Si ɪɪɪ are also detected at 4552, 4567 and 4574 Å. However, the lines of Si ɪɪɪ are not modelled because of the documented discrepancy in the derived abundances between lines of Si ɪɪ and Si ɪɪɪ by Bailey & Landstreet (2013). The final abundance was determined using two separate sets of Si ɪɪ lines: 4128 and 4130 Å fit simultaneously and an individual fit to the single line at 4621 Å. The adopted abundance in each ring was the average between the derived abundances in each window. This abundance was then tested using the remaining lines of Si ɪɪ with consistent model fits observed at all phases. The model fails to correctly model the observed line strength near the magnetic equator (near phase 0.908) as well as producing wings that are too strong for saturated lines such as 4130 and 5056 Å, but otherwise reproduces the line profiles well (see Fig. 3.3).

The distribution of Si appears to vary, with abundance variations of the order of 1.5 dex. Near the observable magnetic pole, Si is about as abundant as in the Sun whereas nearer the magnetic equator it is about 1.5 dex more abundant than the solar value.

3.6.6　Distribution of calcium

Just one line of calcium was found to be useful for abundance determination: 3933 Å. At all phases this line is fit well with a uniform abundance that is about 0.6 dex less than the solar abundance ratio.

3.6.7　Distribution of titanium

The abundance distribution of titanium was determined by fitting Ti ɪɪ at 4563 and 4572 Å simultaneously. At all phases, the lines are reasonably well modelled. Ti is more abundant nearer the magnetic equator where it is about 1.6 dex more abundant than in the Sun. Near the magnetic pole, Ti is at least 0.9 dex more abundant than the solar value.

3.6.8　Distribution of chromium

The final abundance for chromium was derived from three lines of Cr ɪɪ at 4558, 4565 and 4588 Å fit simultaneously. The model is decent at reproducing the observed line profiles for

the weaker Cr lines such as 4565 Å but is noticeably too weak for stronger lines such as 4588 Å at most phases (see Fig. 3.2). Cr also exhibits latitudinal abundance distribution variations by as much as 0.6 dex, and it appears to be more abundant at the magnetic equator as compared to the magnetic pole. In general, Cr is at least 2 dex (peaking at about 2.4 dex near the magnetic equator) more abundant than in the Sun.

3.6.9 Distribution of iron

The abundance of iron was deduced by fitting Fe II lines at 5030, 5032, and 5035 Å simultaneously. The derived abundance was then tested using lines at 4541 and 4583 Å. All lines of Fe are modelled well. The abundance distribution of Fe mirrors that of Cr, with latitudinal abundance variations of the order of 0.5 dex. Compared to the solar abundance ratio, Fe is between 0.8 and 1.3 dex overabundant near the magnetic pole and equator, respectively.

3.6.10 Distribution of nickel

Two lines of Ni II at 3849 and 4067 Å were found with the final abundance being derived from the latter. All lines are fit reasonably well at all phases and the abundance distribution is approximately uniform over the stellar surface at roughly the solar abundance ratio.

3.6.11 Distribution of strontium

Two lines of Sr II are found in the spectra at 4077 and 4215 Å. Special care must be taken to deduce the abundances from these two lines because, with the strong overabundance of Cr, they are blended with Cr II in their wings. We are confident that we have an accurate abundance distribution of Cr and therefore Sr is unambiguously detected. To derive the abundance distribution, each line was fit separately and the adopted abundance is the average between the two lines. The Sr distribution appears to vary strongly with latitude being more abundant, by about 2 dex, near the magnetic equator as compared to the observed magnetic pole. Near the magnetic pole and equator, Sr is nearly 1 and 3 dex more abundant than in the Sun, respectively.

3.6.12 Distribution of lanthanum

Two lines of La II at 4605 and 4636 Å were fit simultaneously to deduce the abundance distribution. The line at 4605 Å is blended with lines of Cr II and possibly Fe II and assuming we have accurate abundances for these Fe-peak elements, this line is useful to derive an abundance. The quality of fit is good at all phases (see Fig. 3.3). A modest variation between the

magnetic pole and equator (~0.5 dex) is observed with a higher abundance near the equator. Globally La is about 10^5 times more abundant than in the Sun.

3.6.13   Distribution of cerium

Ce II at 4628 Å is present in the spectrum but is blended with lines of Fe II and Ti II. Two other pairs of relatively clean Ce II lines were found at 4560-62 and 4133-37 Å. Both sets of lines were fit separately and the final abundance was taken to be the average of the two sets of lines. This abundance was then tested using Ce II at 4628 Å and produces adequate fits to the observed spectrum at all phases (see Fig. 3.3). It is important to note that the adopted abundance produces a model fit to the observed spectrum at 4560 and 4562 Å that is noticeably too strong for these weak lines. A change in the adopted abundance by about −0.3 dex is necessary to fit these lines well. The low excitation potential of all the Ce II lines makes vertical stratification an unlikely solution and we suspect this discrepancy is most likely explained by inaccurate gf values for one or more of the Ce II lines. The model suggests an approximately uniform abundance distribution over the observed stellar surface with cerium being 10^4 times overabundant compared to the solar abundance ratio.

3.6.14   Distribution of praseodymium

The final abundance distribution was derived from lines of Pr III at 6160 and 6161 Å. The derived value was then tested using Pr III at 7781 Å. Variations in abundance by as much as about 1 dex are observed, with the magnetic equator being more abundant than the magnetic pole. Depending upon the phase, Pr is enhanced by between about 4.5 to 5.4 dex compared to the Sun.

3.6.15   Distribution of neodymium

Five clean lines of Nd III at 4570, 4625, 4627, 5050 and 6145 Å are observed in the spectra. The final abundance was deduced from 6145 Å and tested using 4570 and 5050 Å. The abundance of Nd is of the order of 2.5 dex higher than the solar abundance ratio, but the largest abundance appears to be near the magnetic equator where it is about 4.5 dex more abundant than in the Sun.

3.6.16   Distribution of samarium

Two very weak lines of Sm II may be detected at 4674 and 4676 Å, but only at phases near the magnetic equator. Therefore, only an upper limit to the abundance of Sm is deduced that

is $\leq 10^5$ times the solar composition. We possibly detect a single weak line of Sm II at 4630 Å (see Fig. 3.3); however, we remark that this line would require an abundance that is at least 10 times more abundant than the derived upper limit.

3.6.17 Distribution of thulium

A feature at 4643 Å exists that does not correspond to any Fe-peak elements, but is in the exact location of Tm II. We note that if this is due to the rare-earth that an abundance greater than 10^4 times the solar abundance ratio is necessary to adequately model the line. The model fit in Fig. 3.3 assumes this enhanced abundance.

3.7 Conclusions

This chapter is a continuation of our ongoing modelling of hot magnetic Ap/Bp stars in open clusters of known age. The aim of this study is to establish a preliminary magnetic field model and to deduce the atmospheric chemical abundance distribution of many elements.

HD 147010 is a magnetic Bp star ($T_{\text{eff}} \sim 13000$ K) that rotates with a $v \sin i$ of about 15 km s^{-1}. It has $\log L/L_\odot = 1.92$ and mass $M/M_\odot = 3.15$. A member of the Upper Scorpius-Centaurus Association (Sco OB2), HD 147010 is a star with a well-known age of $\log t = 6.70$. The line-of-sight magnetic field strength varies from about -2000 to -5000 G with a surface field of the order of 10 to 18 kG.

A preferred period of $P = 3.9207 \pm 0.0003$ days was adopted for HD 147010 based on previous published measurements of the line-of-sight magnetic field ($\langle B_z \rangle$) by Thompson, Brown & Landstreet (1987) and Mathys (1994) together with our own new measurements as well as photometric observations by North (1984).

The magnetic field of the star is sufficiently large and the rotation rate moderately slow for a Bp star such that Zeeman splitting is clearly observed in at least two spectral lines: Nd III at 6145 Å and Fe II at 6149 Å. These two lines were used to characterise the surface magnetic field ($\langle B \rangle$) variations. By fitting the observed variations in the $\langle B_z \rangle$ and $\langle B \rangle$ data, it was possible to derive a magnetic field model that is a simple, low-order axisymmetric multipole expansion consisting of dipole, quadrupole and octupole components, with the inclination i of the rotation axis to the line-of-sight and the angle β of the magnetic field to the rotation axis specified. The qualitative nature of the magnetic field can be seen in Fig. 3.1. From the figure it is evident that only one magnetic hemisphere is observable, indicating that $i + \beta < 90°$. The adopted field geometry was $i = \beta = 39°$, $B_d = -21300$ G, $B_q = 30300$ G, and $B_{\text{oct}} = -800$ G. The model is a first approximation to the magnetic field variations; however, it is successful at reproducing

the observed variations in both $\langle B_z \rangle$ and $\langle B \rangle$ with phase, as well as adequately reproducing the observed Zeeman broadening in the spectral lines.

We have at our disposal seven Stokes I spectra with which to study the chemical abundance distribution of HD 147010. With the current dataset and available programmes it is not feasible to perform a detailed abundance mapping of the stellar surface; however, we can obtain a first approximation using the simple magnetic field model and ZEEMAN, a program which performs spectral synthesis and takes into account the effects of the magnetic field. Even with only one hemisphere observable, there exist moderate to strong variations over the stellar surface from the magnetic pole to equator in some elements. Therefore, assuming a uniform abundance over the stellar surface was inadequate for the majority of elements studied. After some experimen-tation, a model which employs four co-axial rings (each with a uniform abundance) with two rings in both magnetic hemispheres that each span 45° worked best at describing the observed abundance variations. In this case, only the two rings in the visible hemisphere were varied and the other two rings had their abundances fixed and were found to not influence the derived abundances in the two most visible rings.

The surface chemistry of HD 147010 is very complex and reveals a remarkable number of rare-earth elements. The majority of elements studied have decidedly non-solar abundances. He, O, and Mg are at least 1 dex and Ca about 0.6 dex less abundant than in the Sun and described roughly by a uniform distribution. Both Al and Ni are approximately the same as the solar ratio and uniformly distributed over the stellar surface. The remaining elements (Si, Ti, Cr, Fe, Sr, La, Ce, Pr, and Nd) all have abundances that are higher than in the Sun. Furthermore, all these elements exhibit variations such that they are more abundant near the magnetic equator than the magnetic pole, with the exception of Ce which is uniformly distributed. For the Fe-peak elements (Ti, Cr, Fe) the variations are modest and of the order of 0.6 - 0.7 dex. At their peak abundances, all three elements are at least 1.2 dex overabundant compared to the Sun, with Cr being remarkably 2.5 dex more abundant. Si appears to have a roughly solar abundance near the magnetic pole, but is 1.5 dex more abundant than in the Sun near the magnetic equator. The largest overabundances are seen in Sr and the rare-earth elements (La, Ce, Pr, Nd, and Sm). Respectively, they are as much as 10^2 and $>10^4$ or $>10^5$ times more abundant than compared to the solar ratios. More striking is the fact that Sr and Nd both show variability of the order of 2 dex and La and Pr of the order of 1 dex between the magnetic pole and equator. All of these elements are more abundant at the magnetic equator. Only an upper limit for Sm was found which suggests an abundance that is less than about 10^5 times the solar ratio.

HD 147010 is a rare-earth rich star which is not common for hot magnetic Ap/Bp stars. HD 144897 is another rare-earth rich star with $T_{eff} \sim 12000$ K and $v \sin i \sim 4$ km s^{-1}(see Ryabchikova et al., 2006). HD 144897 has a moderately strong surface field ($\langle B \rangle \sim 9$ kG) for a

magnetic Ap/Bp star, but a sufficiently slow rotation that Zeeman splitting is observed in many spectral lines. The sharp-lined features made it possible to derive abundances for all the rare-earth elements except Pm. On average, all the rare-earth elements were found to be about 10^4 times more abundant than in the Sun. In contrast, HD 318107 is a star of similar temperature (T_{eff} = 11800 K) that has a sufficiently slow rotation rate ($v \sin i \sim 7$ km s^{-1}) and large enough surface field (of the order of 15 kG) that Zeeman splitting is also seen in many spectral lines, but does not appear to have any lines of rare-earth elements beyond Pr and Nd (see Bailey et al., 2011). It is presently unclear why two magnetic Ap stars of comparable characteristics exhibit such drastic differences in the number of rare-earth elements detected. Another rare-earth rich star is HD 66318 (= NGC 2516 24), which is cooler (T_{eff} = 9200 K), and has a plethora of rare-earth elements in the observed spectrum (see Bagnulo et al., 2003). However, the overabundances in HD 147010 are more remarkable, with most rare-earth elements being about 10^4 or 10^5 times enhanced compared to the Sun. Whereas HD 66318 suffered greatly with the quality of model fits to the observed spectrum due most likely to vertical abundance stratification, HD 147010, in general, shows no obvious signs of this when fitting elements of the same ion state (except for Cr II line cores). However, Bailey & Landstreet (2013) point out that a discrepancy in the abundances derived from Si II and Si III exist in all magnetic Ap/Bp stars, including HD 147010. Although abundances of Si III are not presented in this chapter, we remark that a value of at least 0.6 dex higher than is deduced from Si II lines is necessary to adequately fit the Si III lines at 4552, 4567 and 4574 Å.

The model we use is very schematic and does not reproduce exactly the observed line shapes and strengths; however, our model is successful at characterising line profile variations and satisfactorily reproducing Zeeman broadening from using a simple low-order multipole magnetic field geometry. This type of modelling is important to ascertain which stars warrant the time investment of future more detailed studies, such as Magnetic Doppler Imaging (MDI) that require observations in all four Stokes' parameters (e.g. Kochukhov et al., 2004; Kochukhov & Wade, 2010). HD 147010 would seem to be a star that merits further study because it has a complex abundance distribution that includes a plethora of rare-earth elements. In the immediate future, further spectropolarimetric observations nearer the magnetic equator would allow for a better characterisation of the abundance distribution over the entire observable hemisphere.

Bibliography

Asplund M., Grevesse N., Sauval A. J., Scott P., 2009, ARA&A, 47, 481

Babcock H. W., 1960, ApJ, 132, 521

Bagnulo S., Landstreet J. D., Lo Curto G., Szeifert T., Wade G. A., 2003, A&A, 403, 645

Bailey J. D. et al., 2012, MNRAS, 423, 328

Bailey J. D., Landstreet J. D., 2013, A&A, 551, A30

Bailey J. D., Landstreet J. D., Bagnulo S., Fossati L., Kochukhov O., Paladini C., Silvester J., Wade G., 2011, A&A, 535, A25

Donati J.-F., Semel M., Carter B. D., Rees D. E., Collier Cameron A., 1997, MNRAS, 291, 658

Gerbaldi M., Floquet M., Faraggiana R., van't Veer-Menneret C., 1989, A&AS, 81, 127

Kochukhov O., Bagnulo S., Wade G. A., Sangalli L., Piskunov N., Landstreet J. D., Petit P., Sigut T. A. A., 2004, A&A, 414, 613

Kochukhov O., Wade G. A., 2010, A&A, 513, A13

Kupka F., Piskunov N. E., Ryabchikova T. A., Stempels N. C., Weiss W. W., 1999, A&A, 138, 119

Kupka F. G., Ryabchikova T. A., Piskunov N. E., Stempels H. C., Weiss W. W., 2000, Baltic Astronomy, 9, 590

Landstreet J. D., 1988, ApJ, 326, 967

Landstreet J. D., Bagnulo S., Andretta V., Fossati L., Mason E., Silaj J., Wade G. A., 2007, A&A, 470, 685

Landstreet J. D. et al., 2008, A&A, 481, 465

Lanz T., Mathys G., 1991, A&AS, 90, 365

Mathys G., 1994, A&AS, 108, 547

Mathys G., 1995, A&A, 293, 746

Mathys G., Lanz T., 1992, A&A, 256, 169

North P., 1984, A&AS, 55, 259

Piskunov N. E., Kupka F., Ryabchikova T. A., Weiss W. W., Jeffery C. S., 1995, A&A, 112, 525

Przybilla N., Butler K., Becker S. R., Kudritzki R. P., Venn K. A., 2000, A&A, 359, 1085

Ryabchikova T., Ryabtsev A., Kochukhov O., Bagnulo S., 2006, A&A, 456, 329

Ryabchikova T. A., 1991, in IAU Symposium, Vol. 145, Evolution of Stars: the Photospheric Abundance Connection, G. Michaud & A. V. Tutukov, ed., pp. 149–+

Ryabchikova T. A., Piskunov N. E., Kupka F., Weiss W. W., 1997, Baltic Astronomy, 6, 244

Thompson I. B., Brown D. N., Landstreet J. D., 1987, ApJS, 64, 219

Chapter 4

Abundances determined using Si II and Si III in B-type stars

4.1 Introduction

The magnetic peculiar A and B-type stars (Ap/Bp) are characterized by large overabundances of Fe-peak and rare-earth elements. They possess strong, non-axisymmetric magnetic fields. The observed line-of-sight magnetic field component, $\langle B_z \rangle$, is typically of the order of 1 kG or more in strength, and usually varies as the star rotates. The abundance ratios of the chemical elements are often variable over the stellar surface ("patchy"), leading to line strength and shape variations with stellar rotation. This situation is possible because the magnetic field inhibits any convective or turbulent mixing.

In addition to this, Wade et al. (2001b) argued that most magnetic stars exhibit vertical abundance variations (chemical stratification), an idea first explored by Babel (1992). The phenomenon was further studied by Ryabchikova et al. (2001), who compared the chemical abundances derived from the singly- and doubly-ionised forms of Pr and Nd in magnetic and non-magnetic A-type stars. In pulsating ("roAp") magnetic stars, abundances derived from the second ions were found to be 1-1.7 dex larger than abundances from the first ions. In contrast, they found no significant discrepancies between the abundances derived from the first and second ionisation states of Pr and Nd in the non-magnetic and non-pulsating stars. Lines of Pr III and Nd III would normally be formed deeper in the atmospheres of A stars than the lines of the singly-ionised rare earths, because of the higher local temperature deep in the atmosphere. However, as Ryabchikova et al. (2001) pointed out, since electron number density decreases outward, the second ionisation state can also dominate in the very uppermost atmo-

---

[1]A version of this chapter is published as Bailey & Landstreet 2013, A&A, 551, A30

spheric layers. Because of this effect, they were able to understand the discrepancy between ion states as being due to large rare earth overabundances concentrated in a thin layer high in the atmosphere.

A related discrepancy has been observed for abundances of Si derived from two ion states. Semenko et al. (2008) studied the magnetic Bp star HD 45583, which has effective temperature $T_{\rm eff}$ = 13000 K, $\log g$ = 4.0 and a strong magnetic field, with $\langle B_z \rangle$ varying from about -3500 to $+4000$ G. Different abundances must be assumed for Si II and Si III to adequately fit the theoretical to the observed line profiles. They interpret this discrepancy as being due to vertical stratification of silicon in the atmosphere, but point out that increasing $T_{\rm eff}$ from the assumed value also brings the abundances derived from lines of Si II and Si III into better agreement. Bailey et al. (2012) found a similar discordance in the derived abundances of the first and second ionisation states of Si in HD 133880, another strongly magnetic Bp star ($\langle B_z \rangle$ varies from about -4000 to $+2000$ G) having $T_{\rm eff}$ = 13000 K and $\log g$ = 4.34. They find that an enhancement of about 1 dex above the Si II abundance is necessary to adequately fit the Si III lines. Since non-LTE effects in the silicon lines are expected to be small below a $T_{\rm eff}$ of about 15000 K, they suggest that the most probable cause is strong stratification of Si in the atmosphere.

The study of vertical abundance stratification in magnetic Ap stars has considerably expanded in the past few years, with work led by Kochukhov and Ryabchikova (e.g. Kochukhov et al., 2006, 2009; Shulyak et al., 2009; Pandey et al., 2011). This group has developed refined methods of recovering the vertical distribution of several elements in a stellar atmosphere by simultaneous fits to a number of spectral lines of different strengths, excitation potentials, and ionisation states. They have studied several cool magnetic Ap stars in detail, and mapped the vertical distribution of a number of elements in each, in several cases including Si. Typically, it is found that Si has high abundance deep in the atmosphere, and an abundance that declines strongly towards low optical depths, sometimes by as much as 3 dex overall.

Up to now, the study of discrepancies among different ion states, and of stratification as a probable explanation, has mainly been confined to cool magnetic Ap stars. It is time for a first survey of higher effective temperatures. In this paper, we report an empirical study of abundances derived from lines of Si II and Si III in various classes of B-type stars including magnetic Bp, HgMn, and normal B stars. Stars were selected from the ESO, CFHT, and ELODIE archives (as well as from our own data from previous CFHT and ESO programmes). The stars studied have $T_{\rm eff}$ values that range from about 10500 to 15000 K, and have low enough projected rotational velocity $v \sin i$ (less than about 100 km s^{-1}) that lines of Si III can be unambiguously detected. The following section discusses the spectroscopic observations used. Sect. 4.3 outlines the modelling technique and the spectrum synthesis program used.

Sect. 4.4 presents the abundances we derive from lines of Si ii and Si iii. Sect. 4.5 investigates the possible effects of non-LTE in deriving abundances of Si ii and Si iii with increasing T_{eff} and we test whether the observed discrepancies can be accounted for using stratified abundance models. Sect. 4.6 summarises and discusses the work we present.

4.2   Stellar sample

We wish to study the extent to which the abundance of Si as derived from Si ii and Si iii is concordant or discordant. With the tools readily available to us, this can only be done in a limited range of T_{eff} values or spectral range. Our low-temperature limit is set by the fact that no Si iii lines are visible in optical spectra for T_{eff} less than about 11000 K. The high-temperature limit is set by the gradual onset of non-LTE effects at about 15000 K (Przybilla et al., 2011). This upper limit to our study, which is not well-defined, is imposed by two main factors. First, the non-LTE codes developed up to now do not incorporate radiative transfer in the presence of a magnetic field. Thus, they cannot be used directly to study magnetic stars, which are an important class of objects for this study. Furthermore, as we will show below, the published grid of non-LTE equivalent widths for Si ii and iii lines of Becker & Butler (1990) do not even approximately reproduce the line ratios in the normal B3 IV star ι Her = HD 160762, and recent non-LTE abundance studies of early B stars appear to systematically reject use of the Si ii lines. It is not at all clear that current non-LTE codes are able to correctly compute line ratios for Si ii lines. Therefore we try to limit our study to effective temperatures low enough that strong non-LTE effects are not expected; this limiting temperature is conventionally set at T_{eff} = 15000 K (e.g. Nieva et al., 2012). We have included one hotter star, HD 160762, in order to address non-LTE questions later in the paper.

The spectra for this study were obtained from a variety of sources. A large portion of the stars studied were acquired from previous observing runs using the ESPaDOnS spectropolarimeter (with resolving power R = 65000) at the Canada-France-Hawaii Telescope (CFHT), and the FEROS spectrograph (R = 48000) at the European Southern Observatory's (ESO) La Silla Observatory. The remaining spectra used were acquired from the ESO, CFHT and ELODIE (Observatoire de Haute Provence) archives. We required that each individual spectrum have a signal-to-noise ratio (S/N) greater than about 100 and spectral resolution no less than about 40000. As discussed above, we selected stars of T_{eff} between about 10500 and 15000 K, requiring also that they have sufficiently slow rotation ($v \sin i$ less than about 100 km s^{-1}) that at least some individual lines are not strongly blended.

In the effective temperature range of interest for this study, there are (at least) three major classes of main sequence stars. In addition to normal late B stars (which generally do not

Table 4.1: Stars analyzed in this study. Listed are the star designations, instrument used, spectral resolution, spectral range and the S/N.

Star	Instrument	R	λ (Å)	S/N
normal stars				
HD 22136	ESPaDOnS	65000	3690-10481	504
HD 160762	ESPaDOnS	65000	3690-10481	600
HD 162586	UVES	110000	3070-10398	655
HD 170054	ESPaDOnS	65000	3690-10481	283
HD 179761	ELODIE	42000	4000-6800	125
HD 195810	ESPaDOnS	65000	3690-10481	774
HD 222173	ELODIE	42000	4000-6800	159
HgMn stars				
HD 27295	UVES	110000	3750-6800	218
HD 57608	FEROS	48000	3528-9217	142
HD 78316	UVES	110000	3750-6800	265
HD 175640	UVES	110000	3750-5800	439
HD 178065	UVES	110000	3750-5800	461
HD 186122	ESPaDOnS	65000	3690-10481	662
HD 193452	CF4	120000	4630-5478	556
magnetic Bp stars				
HD 10840	UVES	110000	3070-10398	824
HD 45583	FEROS	48000	3528-9217	231
HD 47116	UVES	110000	3070-10398	527
HD 49333	UVES	110000	3070-10398	791
HD 61045	ESPaDOnS	65000	3690-10481	298
HD 74168	UVES	110000	3070-10398	334
HD 74535	FEROS	48000	3528-9217	310
HD 133880	ESPaDOnS	65000	3690-10481	365
HD 137509	UVES	110000	3690-10481	430
HD 147010	ESPaDOnS	65000	3690-10481	587
HD 199728	UVES	110000	3070-10398	593
HD 223640	UVES	110000	3070-10398	560
HD 304842	FEROS	48000	3528-9217	262
HD 318107	ESPaDOnS	65000	3690-10481	320
BD+00 1659	ESPaDOnS	65000	3690-10481	475
BD-19 5044L	ESPaDOnS	65000	3690-10481	358
BD+49 3789	ESPaDOnS	65000	3690-10481	191

have detectable magnetic fields, and have approximately solar surface abundances), we also find magnetic Bp stars, which usually show quite marked abundance differences compared to the Sun, and the non-magnetic HgMn stars, which are typically found in fairly close binary systems and show quite non-solar over-abundances of several low-abundance elements such as P, Mn, Ga, and Hg. We have included several examples of each of these classes in our sample. The sample of stars utilised in this study is summarised in Table 4.1.

The fundamental parameters T_{eff} and $\log g$ were derived for each star using Geneva and *uvbyβ* photometry. For the Geneva photometry, we use the FORTRAN program described by Kunzli et al. (1997) and for stars with Strömgren *uvbyβ* photometry, the FORTRAN program "UVBYBETANEW" of Napiwotzki et al. (1993). Our version of this program corrects the T_{eff} of the magnetic Ap/Bp stars to a suitable Ap temperature scale (see Landstreet et al., 2007). For stars for which both sets of photometry were available, the average value was taken. We were able to compare our T_{eff} values with those of Netopil et al. (2008) in a few cases; our values agree with theirs except for HD 133880, for which T_{eff} is somewhat more uncertain, as discussed by Bailey et al. (2012). Finally, we have estimated the uncertainty in T_{eff} to be about 500 K, following the discussion of Landstreet et al. (2007). The uncertainty in $\log g$ is estimated from the level of agreement between values derived from Geneva and Strömgren photometry to be about 0.2 dex. The physical parameters for HD 160762 were taken from Nieva et al. (2012), and have uncertainties that are about half as large as those of the other normal stars. Table 4.2 summarises all the physical parameters of the stars modelled in this study, including parameters discussed later in this chapter.

4.3   Modelling spectra

4.3.1   Modelling with the spectrum synthesis code ZEEMAN

Modelling and abundance determination was carried out using the FORTRAN spectrum synthesis code ZEEMAN (see Landstreet, 1988; Landstreet et al., 1989; Wade et al., 2001a; Bailey et al., 2012). ZEEMAN accepts as input an assumed magnetic field geometry for stars with magnetic fields (such as the magnetic Ap/Bp stars), but functions as a conventional line synthesis program for modelling of non-magnetic stars (e.g. Landstreet et al., 2009). The program assumes LTE atmospheric structure and line formation. An appropriate stellar atmosphere model is interpolated from a grid of ATLAS 9 solar abundance models. For this study, a uniform abundance is assumed over the stellar atmosphere even for stars such as magnetic Bp stars for which this may be only a rough first approximation.

Table 4.2: Physical parameters for the stars in this study. We adopt a uniform uncertainty of ±500 K in $T_{\rm eff}$ and ±0.2 in log g.

Star	$T_{\rm eff}$ (K)	log g	$v \sin i$ (km s^{-1})	i (°)	β (°)	B_d (G)	B_q (G)	B_{oct} (G)	ξ (km s^{-1})
normal stars									
HD 222173	11800	3.4	67 ± 5	–	–	–	–	–	0 ± 1
HD 22136	12700	4.2	15 ± 2	–	–	–	–	–	1.1 ± 0.3
HD 162586	12700	4.0	28 ± 2	–	–	–	–	–	0 ± 1
HD 179761	12900	3.4	14 ± 2	–	–	–	–	–	0 ± 1
HD 195810	13700	3.7	52 ± 4	–	–	–	–	–	0 ± 1
HD 170054	14500	4.3	25 ± 2	–	–	–	–	–	0 ± 1
HD 160762	17500	3.8	6 ± 1	–	–	–	–	–	1 ± 1
HgMn stars									
HD 193452	10600	4.1	1.4 ± 1	–	–	–	–	–	0 ± 1
HD 57608	10900	3.1	5.0 ± 1	–	–	–	–	–	1.3 ± 0.4
HD 27295	11800	4.2	4.9 ± 0.3	–	–	–	–	–	1.8 ± 0.5
HD 175640	12000	4.0	1.5 ± 1	–	–	–	–	–	0 ± 1
HD 178065	12300	3.6	2.0 ± 1	–	–	–	–	–	0 ± 1
HD 186122	12900	3.7	1.0 ± 0.5	–	–	–	–	–	0 ± 1
HD 78316	13400	3.9	6.8 ± 0.5	–	–	–	–	–	0 ± 1
magnetic Bp stars									
HD 47116	11000	4.1	30 ± 2	–	–	500	–	–	0
HD 10840	11600	3.6	35 ± 5	–	–	500	–	–	0
HD 318107	11800	4.2	7 ± 1	22	65	25600	−12800	900	0
HD 199728	12200	3.7	62 ± 6	–	–	800	–	–	0
HD 223640	12300	4.4	31 ± 3	–	–	500	–	–	0
BD+00 1659	12500	4.0	7.0 ± 1	–	–	1200	–	–	0
HD 304842	12500	3.9	65 ± 5	–	–	100	–	–	0
HD 45583	12700	4.2	70 ± 6	–	–	8000	–	–	0
BD-19 5044L	12800	4.5	15 ± 3	–	–	800	–	–	0
BD+49 3789	12900	4.2	85 ± 5	–	–	1700	–	–	0
HD 74168	12900	4.5	63 ± 4	–	–	200	–	–	0
HD 61045	13000	4.1	64 ± 3	–	–	1300	–	–	0
HD 147010	13000	4.4	15 ± 2	–	–	15000	–	–	0
HD 133880	13000	4.3	103 ± 10	55	78	−9600	−23000	1900	0
HD 137509	13100	4.3	20 ± 2	81	64	3100	41900	−500	0
HD 74535	13600	4.3	45 ± 4	–	–	300	–	–	0
HD 49333	15100	3.9	68 ± 3	–	–	800	–	–	0
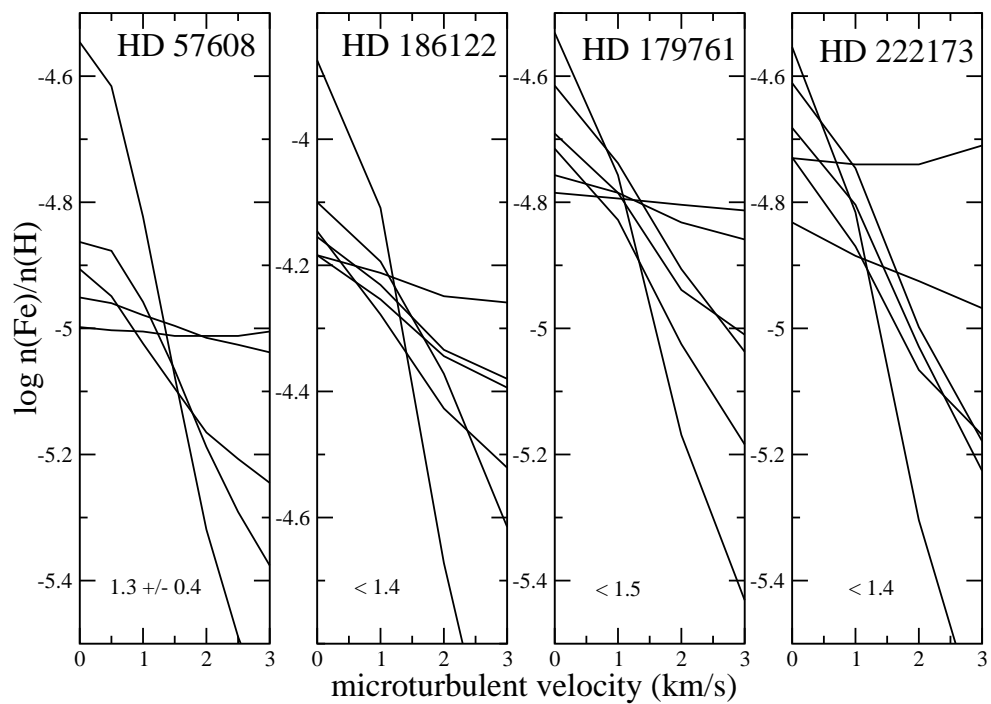
Figure 4.1: Blackwell diagrams (from left to right) for HD 57608, HD 186122, HD 179761 and HD 222173. Shown are lines for Fe II $\lambda\lambda$ 4541, 4555, 4576, 4583, 5018 and sometimes 6120 and/or 6129. Each panel spans 1.0 dex.

zeeman functions by comparing a synthesised spectrum to an observed one in one or more selected wavelength windows. By iteratively minimising the mean square difference between the computed and observed spectrum, zeeman automatically determines the best fit radial velocity v_R and the best value of $v \sin i$ for the spectral windows modelled. It optimises the fit to all the lines of a single chemical element within the selected window(s), determining the value of the abundance of that element relative to H. This process is repeated for other elements until most of the lines in each spectral window studied are modelled as well as possible with the limitations imposed by the assumptions built into the model. The adopted abundances are obtained from the average of two ~100 Å windows, with the uncertainty estimated from the observed scatter of the computed values in the modelled spectral windows.

For non-magnetic stars, the microturbulence parameter ξ was determined using the method described by Landstreet et al. (1998). The abundance is iteratively deduced for a number of individual lines of Fe for a small grid of assumed ξ values. The resulting abundance values are plotted in a Blackwell diagram for each line as a function of ξ. The value of ξ for which the abundance values from the lines studied agree best is accepted as the optimal value, and the corresponding value of Fe/H abundance is adopted. Examination of the dispersion of the abundance values as a function of ξ yields estimates of the uncertainties of both Fe abundance and ξ. Several examples of this procedure are shown in Figure 4.1.

In most cases, the microturbulence parameter does not seem to be significantly different from zero, but we think that we detect a non-zero value in three stars: the normal star HD 22136, and the two HgMn stars HD 57608 and HD 27295. All three of these stars are near the low temperature limit of our sample, and all three have rather sharp lines, making abundance analysis more precise and perhaps making detection of non-zero ξ easier. Detection of non-zero microturbulence is quite interesting, as it suggests the presence of convective mixing in at least part of the atmosphere (e.g. Landstreet et al., 1998, 2009). This would in turn suggest that the atmosphere is at least partly mixed, so that a stratified abundance distribution could be destroyed by rapid mixing, if the mixing extends through enough of the atmosphere.

For magnetic stars, the microturbulence parameter ξ was set to 0, as the magnetic field is thought to suppress convective motions.

For the magnetic stars HD 137509, HD 318107, and HD 133880, detailed colinear multipole magnetic field geometries have been reported in the literature that could be used for modelling: (see Kochukhov, 2006; Bailey et al., 2011, 2012, respectively). For other stars, the line-of-sight magnetic field measurements, $\langle B_z \rangle$, of Bagnulo et al. (2006); Kochukhov & Bagnulo (2006); Landstreet et al. (2008) and available unpublished data were used to estimate the polar field strength of a simple dipole field model. In these cases, a dipolar field of about three times the root-mean square of the available $\langle B_z \rangle$ measurements was used in computing the

synthetic spectra. For stars for which abundances of Fe-peak and rare earth elements clearly indicate a Bp nature, but for which no $\langle B_z \rangle$ measurements are available, a generic polar field of ~500 G was used. For all stars for which no previous magnetic modelling was available, we set the inclination of the rotation axis to the line of sight, i, and the obliquity of the magnetic field axis to the rotation axis, β, to zero ($i=\beta=0$).

4.3.2   Atomic data

The atomic data (energy levels, oscillator strengths, damping constants, and Landé factors) used for this analysis were taken from the Vienna Atomic Line Database (VALD) (Piskunov et al., 1995; Ryabchikova et al., 1997; Kupka et al., 1999, 2000). When Landé factors were not available from this source, they were computed assuming LS coupling.

Since it is clear that this study depends sensitively on the accuracy of the atomic line data, particularly oscillator strengths, we have endeavoured to test the VALD gf values extensively.

One test of the Si II gf values is to use them for determination of the abundance of silicon in the star Sirius = HD 48915, for which very accurate fundamental and other parameters (e.g. the value of ξ) are available, and for which a number of excellent UVES high-resolution spectra are available from the ESO archive (Landstreet, 2011). Abundances of Si II were determined from the lines $\lambda\lambda$ 4621, 5041 & 5056, 5957 & 5978, and 6347 & 6371. The derived abundances have a mean of $\log N_{Si} / \log N_H = -4.25 \pm 0.07$ dex, where the uncertainty is the dispersion of the four values. The value, about 0.2 dex larger than the solar abundance, is not unexpected in this hot Am star, and the dispersion indicates that the gf values used are closely compatible.

This test has also been carried out on several of the stars in our sample, to see how consistently the VALD data give the same abundances with different spectral lines and line groups. To obtain a realistic idea of the uncertainties in deriving abundances for Si II, we select a sample of magnetic, normal, and HgMn stars that are well spread in T_{eff} (within the limitations of the data at hand). For these stars we derive abundances from λ4621 individually, $\lambda\lambda$5041, 5055 and 5056 simultaneously, and $\lambda\lambda$5957 and 5978 simultaneously. Table 4.3 presents our results, line-by-line, and with the computed dispersion of the three abundance values for each star. In general, the abundances we derive from the various lines of Si II show dispersion which is only slightly greater than that found for Sirius. The magnetic stars show the greatest tendency for the dispersion of abundances derived from different lines of Si II to be larger than we found for Sirius; however, this result is expected, as the magnetic stars typically have horizontally non-uniform abundances and may also have vertically stratified abundance distributions (Wade et al., 2001b). Nevertheless, we note that, in general, assuming a uniform abundance of Si fits all lines of Si II in all stars analysed within a fitting uncertainty of about ±0.15 dex or better.

Table 4.3: Derived abundances from individual lines of Si II for a selection of stars in our sample.

	HgMn stars				Normal stars				Magnetic stars			
	HD				HD				HD			
Line (Å)	178065	27295	57608	78316	222173	22136	170054	162586	74168	49333	223640	47116
4621	−4.67	−4.52	−4.89	−4.34	−4.66	−4.67	−4.64	−4.67	−4.00	−3.90	−3.09	−3.21
5041-55-56	−4.56	−4.58	−4.78	−4.44	−4.63	−4.64	−4.81	−4.82	−4.11	−4.15	−3.20	−3.48
5957-78	−	−4.54	−4.66	−4.26	−4.48	−4.59	−4.70	−4.72	−3.93	−3.91	−2.98	−3.27
Dispersion	−	0.03	0.12	0.09	0.10	0.04	0.09	0.08	0.09	0.14	0.11	0.14

A further test of the atomic data is to compare the VALD gf values with the data in the comprehensive NIST compilation of atomic data for Si by Kelleher & Podobedova (2008). In this data set, the recommended atomic data are selected on a line-by-line basis from available experiments and computations, without consideration of internal homogeneity. Most of the log gf values of Si ii needed for our work are estimated by those authors to have uncertainties of around ±0.1 dex. Overall, for the lines studied by us, there is only a very small difference (NIST − VALD) in the mean of all required log gf values of about −0.04 dex for Si ii, and +0.1 dex for Si iii. As we shall see below, this is not a large enough difference to play an important role in measurements of the difference in abundances found in some stars between Si ii and Si iii, although if we used the NIST gf values instead of VALD data, this would tend to decrease the abundance differences found by ∼ 0.15 dex.

We have repeated the Si abundance determinations for Sirius with the NIST Si ii data. The average abundance found is in this way is −4.20 ± 0.14. The change in the mean is thus very small, but the dispersion from line group to line group is doubled with respect to the results found using the VALD data. This kind of difference has been found in earlier comparisons of NIST and other, more homogenized, data (e.g. Sigut & Landstreet, 1990), and appears to arise from the NIST preference for data selection for individual lines from single data sources. In particular, the NIST gf value for the Si ii line at 5041 Å is quite discrepant with the VALD value, and when the NIST values are used for synthesis of the spectral region containing the $\lambda\lambda$ 5041 and 5056 lines, the best fits are clearly not concordant between the two lines. It is because of this larger dispersion that we prefer to use the VALD atomic data.

For Si iii we are able to determine the Si abundance using only the lines of multiplet (2) at 4552, 4567, and 4574 Å. The log gf values adopted by VALD, and by us, for these three lines are all about 0.1 dex smaller than those in the NIST compilation. The relative strengths of the lines are closely identical in both datasets. For consistency with our Si ii analyses, we use the VALD values.

We have also double-checked that our assumed ionisation potentials are very closely the same as those of Kelleher & Podobedova (2008). In summary, there is no obvious reason to think that the results we find below are due to some major defect in the available spectral line data.

4.3.3   Si abundance uncertainties resulting from errors in stellar parameters

The uncertainty in log g and especially in T_{eff} introduces significant uncertainty in the derived abundances, especially of Si iii. This issue has been explored for the different classes of stars in

this study by repeating the determination of the best fitting abundance of several stars with values of T_{eff} or $\log g$ altered by the adopted uncertainties, and comparing the resulting abundance values with those derived with the adopted stellar parameters.

Over most of the temperature range studied, Si ii is the dominant form of Si throughout much of the atmosphere. Therefore, changing the value of T_{eff} by 500 K typically results in a fairly small change in the abundance of Si ii which best fits the observed lines. Generally, the change in derived abundance is of the order of 0.05 dex, with the derived abundance decreasing slightly if the adopted T_{eff} value is increased. Apparently the increased population of the high excitation lower levels of the Si ii lines (at around 10 eV) more than compensates for the effect of the Saha equation in decreasing the fraction of Si in the form of Si ii. The changes to the abundance derived from lines of Si ii for a change in $\log g$ of 0.2 dex is also of order 0.05 dex, with an increase in $\log g$ resulting in a decrease in the abundance deduced from Si ii, as the Saha equation forces more Si from the doubly into the singly ionised state.

In the temperature range studied, the fraction of Si iii increases strongly from a very small fraction at the low temperature end to about half of the total Si near 15000 K. Furthermore, the lower levels of the lines of multiplet (2) are at almost 19 eV. As a result, the abundance of Si derived from lines of Si iii is a much stronger function of T_{eff}. With a change of T_{eff} of +500 K, the deduced Si abundance can change by as much as roughly −0.3 dex, decreasing somewhat towards the high end of the temperature range studied. The deduced abundance also changes more with a change in $\log g$ of 0.2 dex than is the case for Si ii; the derived abundance can change by an amount of order 0.1 dex.

4.4 Measured Si ii and iii abundances in the B star sample

In this Section we tabulate and discuss the results of our abundance analysis of the stars of the sample discussed above.

Table 4.4 presents the final mean abundances we find for each star. The first four columns list the star name (generally an HD Number), and recall the T_{eff}, $v \sin i$, and ξ values from Table 4.2. Next we tabulate abundance values found for Ti, Cr, and Fe. The abundances of these three elements had to be determined in order to evaluate and test the microturbulence parameter independently of the Si lines (for the non-magnetic stars only), to correctly include the effects of weak blends with the Si lines modelled, and to allow a precise determination of v_{R} and $v \sin i$. For all stars, the abundance of iron was found from simultaneously fitting three lines of Fe ii: 4541, 4555, and 4583 Å. Similarly, where possible we derived the abundance of chromium from lines of Cr ii at 4558, 4588, and 4592 Å and titanium from lines of Ti ii at 4565 and 4572 Å. The abundance of Fe and the value of ξ for HD 160762 were taken from Nieva
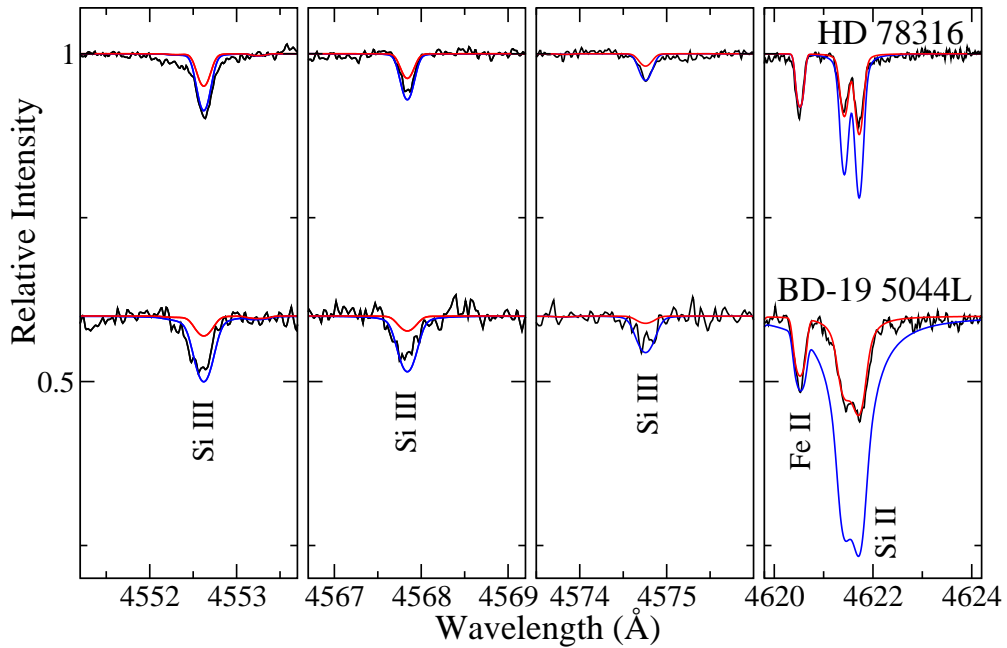
Figure 4.2: Model fits to lines of Si II (right) and Si III (left three panels) to the non-magnetic HgMn Star HD 78316 (upper spectrum) and the magnetic Bp star BD-19 5044L (lower spectrum). The black lines are the observed spectra, red lines are the best fit model using the abundance derived from Si II and the blue lines are the best fit model using the abundance derived from Si III.

Table 4.4: Abundances derived for Ti, Cr, Fe, and the first and second ionization states of Si. Uncertainties are estimated to be about ±0.2 dex for the magnetic Bp stars and ±0.1 dex for the non-magnetic normal and HgMn stars with exceptional values in parentheses.

Star	T_{eff} (K)	$v \sin i$ (km s^{-1})	ξ (km s^{-1})	log(Ti/H)	log(Cr/H)	log(Fe/H)	log(Si/H) Si ii	Si iii	ΔSi	σ_D
					normal stars					
HD 222173	11800	67 ± 5	0 ± 1	−7.80	−6.64	−4.96	−4.59(0.15)	−4.03(0.2)	0.56	2.2
HD 22136	12700	15 ± 2	1.1 ± 0.3	−7.32	−6.34	−4.82	−4.63	−4.41	0.22	1.4
HD 162586	12700	28 ± 2	0 ± 1	−6.95	−6.26	−4.84	−4.74	−3.90	0.84	5.9
HD 179761	12900	14 ± 2	0 ± 1	−7.43	−6.38	−4.75	−4.23	−4.72	0.49	3.5
HD 195810	13700	52 ± 4	0 ± 1	−7.41	−6.35	−4.58	−4.24	−4.65	0.41	2.9
HD 170054	14500	25 ± 2	0 ± 1	−7.46	−6.67	−4.95	−4.72	−4.21	0.51	3.6
HD 160762	17500	6 ± 1	1 ± 1	−	−	−4.49	−5.34	−4.10	1.24	8.9
					HgMn stars					
HD 193452	10600	1.4 ± 1	0 ± 1	−6.50	−5.73	−4.22	−4.20	−	−	−
HD 57608	10900	5.0 ± 1	1.3 ± 0.4	−8.08	−6.81	−5.31	−4.78	−4.82	−0.04	0.28
HD 27295	11800	4.9 ± 0.3	1.8 ± 0.5	−5.83	−6.03	−5.31	−4.58	−4.41	0.17	1.2
HD 175640	12000	1.5 ± 1	0 ± 1	−6.54	−5.79	−4.83	−4.46	−3.76	0.70	5.0
HD 178065	12300	2.0 ± 1	0 ± 1	−6.49	−6.04	−4.65	−4.61	−4.29	0.32	2.3
HD 186122	12900	1.0 ± 0.5	0 ± 1	−6.68	−7.38	−4.09	−5.54	−4.90	0.64	4.5
HD 78316	13400	6.8 ± 0.5	0 ± 1	−6.79	−6.06	−4.45	−4.35	−3.91	0.44	3.2
					magnetic Bp stars					
HD 47116	11000	30 ± 2	0	−4.65	−4.93	−3.65	−3.32	−2.39	0.93	3.3
HD 10840	11600	35 ± 5	0	−6.68	−5.56	−3.49	−3.48	−2.71	0.77	2.7
HD 318107	11800	7 ± 1	0	−5.05(0.1)	−4.50(0.15)	−3.00(0.2)	−3.65(0.15)	−2.73	0.92	3.7
HD 199728	12200	62 ± 6	0	−7.38	−5.33	−4.07	−3.09	−2.46(0.25)	0.63	2.0
HD 223640	12300	31 ± 3	0	−6.89	−4.65	−3.42	−3.42	−2.17	1.25	4.4
BD+00 1659	12500	7.0 ± 1	0	−6.69	−5.02	−3.79	−3.53	−2.51	1.02	3.6
HD 304842	12500	65 ± 5	0	−6.82	−6.16	−4.34	−3.65	−2.91(0.25)	0.74	2.3
HD 45583	12700	70 ± 6	0	−5.67	−4.68	−3.40	−3.33	−2.10(0.25)	1.23	3.8
BD-19 5044L	12800	15 ± 3	0	−6.70	−5.80	−4.15	−3.99	−2.76	1.23	4.3
BD+49 3789	12900	85 ± 5	0	−6.23	−5.48	−4.09	−3.44	−2.59(0.3)	0.85	2.4
HD 74168	12900	63 ± 4	0	−6.77	−6.30	−4.81	−4.01	−2.95(0.25)	1.06	3.3
HD 61045	13000	64 ± 3	0	−5.96	−5.24	−3.90	−3.79	−2.56(0.25)	1.23	3.8
HD 147010	13000	15 ± 2	0	−5.81	−4.18	−3.46	−4.03	−3.46	0.57	2.0
HD 133880	13000	103 ± 10	0	−4.86	−4.49	−3.30	−2.68	−1.23(0.3)	1.45	4.0
HD 137509	13100	20 ± 2	0	−4.62	−4.20	−3.19	−3.52	−2.02	1.50	5.3
HD 74535	13600	45 ± 4	0	−6.25	−5.60	−3.98	−4.25	−2.53	1.72	6.1
HD 49333	15100	68 ± 3	0	−5.97	−5.66	−4.18	−3.99	−2.50(0.3)	1.49	4.1

et al. (2012), but the Si abundances were determined by us in the usual way.

For the magnetic Bp stars, we estimate the uncertainties of the abundances of the Fe-peak elements to be ±0.2 dex, a typical deviation from the derived abundance necessary to produce an unsatisfactory fit of the model to the observed spectra. The uncertainty derived in the same manner for the non-magnetic stars suggests a smaller uncertainty of ±0.1 dex. Uncertainties that differ from the aforementioned values are noted in parentheses. This is the case for stars with $v \sin i$ greater than about 60 km s^{-1} where line blending makes the derived abundances somewhat less certain.

Following the Fe-peak elements, two columns list abundances derived from lines of Si ii and Si iii separately, for each star in our sample. The next column gives the difference of the two Si abundance determinations, in the sense Si iii – Si ii, and the final column gives the difference divided by the estimated uncertainty of the difference, including only the fitting uncertainties discussed in this section. (Recall that the uncertainty in T_{eff} substantially increases the uncertainty in the abundance derived from Si iii, to at least ±0.3 dex.)

It will immediately be seen that the values of $\log(N_{\text{Si}}/N_{\text{H}})$ are quite discordant as derived from the two different ionisation states of Si. The reader may wonder how robust these large differences are. Figure 4.2 illustrates the type of fits we obtain with magnetic and non-magnetic stars using abundances derived from lines of Si ii and Si iii. The situation for the lines of these two ions is mostly quite different than the fits found for the Fe-peak elements Ti, Cr and Fe, for which all lines of the elements are generally fit well with a single value of the abundance. In both the HgMn star (upper spectrum) and the magnetic star (lower spectrum), the abundance that best fits the lines of multiplet (2) of Si iii at 4552-67-74 Å (model fit in blue) predicts a Si ii line at 4621 Å that is far too strong. Conversely, the abundance that fits the Si ii line at 4621 Å, and the other Si ii lines modelled, leads to model lines for the Si iii lines that are much too weak. This discrepancy is really striking for the magnetic Bp star. It is present but at a less spectacular level for most of the HgMn stars, and even seems to be present for some of the normal stars.

The sharp-lined HgMn stars, which have a roughly solar abundance of Si, allow us to establish the lower limit of T_{eff} for which Si iii is observable. This was done by searching for the presence of $\lambda 4552$, the strongest Si iii line of multiplet (2), which also includes $\lambda\lambda 4567$, and 4574. We are able to detect a very weak line of Si iii in HD 57608 ($T_{\text{eff}} = 10900$ K), however, in a slightly cooler star, HD 192452 ($T_{\text{eff}} = 10600$ K) we are unable to unambiguously detect any lines of Si iii. This threshold also depends somewhat on $\log g$, but for a solar abundance of Si, we can begin to detect Si iii in main sequence stars at $T_{\text{eff}} \approx 11\,000$ K.

4.5 Possible explanations of the Si II-III anomaly

The results presented in the previous section show that the abundances derived from the singly and doubly ionised states of Si are in general different. This difference is always of the order of one dex for the magnetic stars in our sample, and apparently varies from near zero to almost one dex for the normal and HgMn stars. The difference is always in the same sense: if the abundance is chosen to have a value consistent with the Si II lines, the predicted strengths of the Si III lines are always too small.

It is first worth noticing that there are three stars for which no hint of discrepancy between the abundance of Si derived from the two ionisation states. These are exactly the three stars for which we believe that we detect a non-zero microturbulence parameter ξ, and thus presumably the presence of atmospheric convection. It is not obvious what makes these stars different from other normal or HgMn stars of similar fundamental parameters, since we expect the presence or absence of atmospheric convective zones to vary smoothly with T_{eff}, $\log g$, and perhaps abundance. Thus our initial expectation was that at low T_{eff} values, where we expect weak convective mixing (but do not usually securely detect it), all the stars might be reasonably mixed, or all not mixed.

We also recall (Sec. 3.3) that the discrepancy between abundances deduced from Si II and III decreases as T_{eff} increases. Thus, a possible explanation of the discrepancy we find is a systematic underestimate of T_{eff} for almost all the stars of our sample. To explain the discrepancies found among normal and HgMn stars, the values of T_{eff} would have to be systematically underestimated by an amount of the order of 1000 K, which would reduce the discrepancy by about 0.5 dex. For the magnetic stars, the systematic error in T_{eff} needed would be of order 2000 K. Although such large errors are possible, they seem unlikely to us, and so we look for other explanations of the observed differences.

We next consider two further possible explanations of the abundance discrepancy that we do detect in almost all the stars in our sample: non-LTE effects, and Si abundance stratification.

4.5.1 Non-LTE effects in B-type stars

Recent studies of non-LTE effects in the atmosphere of O and early B-type stars have been carried out (e.g. Przybilla et al., 2011; Nieva et al., 2012) testing the predictions of LTE and non-LTE line synthesis codes for main sequence stars with T_{eff} between about 15000 and 35000 K. They show that a hybrid method, combining LTE model atmospheres with non-LTE line synthesis, is capable of yielding very accurate basic stellar parameters, and very satisfactory fit to most spectral lines. From comparisons of their non-LTE results to fully LTE synthesis, they conclude that pure LTE modelling yields meaningful results up to about a T_{eff} of 22000 K for a

Table 4.5: Silicon abundances deduced for HD 160762 from lines of Si ii and iii using the non-LTE equivalent width calculations of Becker & Butler (1990), and LTE models computed with zeeman.

| | | | $\log(N_{Si}/N_H)$ | | |
| | | | Becker & Butler | | Zeeman |
Ion	Line (Å)	W_λ (Å)	$\xi = 0$ km s^{-1}	$\xi = 3$ km s^{-1}	$\xi = 1$ km s^{-1}
Si ii	4128	57.3	< -5.0	< -5.0	-5.13[1]
	4130	63.2	< -5.0	< -5.0	
	5041	40.1	< -5.0	< -5.0	-5.34[2]
	5055	49.1	< -5.0	< -5.0	
	5056	21.9	< -5.0	< -5.0	
Si iii	4552	70.1	-4.1	-4.3	-4.10[3]
	4567	47.5	-4.3	-4.5	
	4574	28.2	-4.2	-4.5	

NOTES. (1) $\lambda\lambda 4128$ and 4130 simultaneously. (2) $\lambda\lambda 5041$, 5055, and 5056 simultaneously. (3) $\lambda\lambda 4552$, 4567, and 4574 simultaneously.

large number of spectral lines. However, lines with this behaviour must be carefully identified. Neiner et al. (2012) have been able to determine abundances of a number of elements for the star HD 96446 ($T_{eff} = 21600 \pm 800$ K) by using only spectral lines that are approximately the right strength when computed with LTE synthesis and non-LTE abundances for standard stars such as α Pyx.

Unfortunately, Neiner et al. (2012) find that lines of Si ii and iii mostly are not among the lines that are predicted to have the observed strength in standard stars by LTE synthesis. Thus, it appears that among early B type stars, non-LTE effects are probably important for Si. These results are consistent with comments by Przybilla et al. (2011) who suggest that lines of silicon are strongly influenced by non-LTE effects above about 15000 K.

We do not have the tools to carry out non-LTE synthesis for this project. However, we have included the star HD 160762 ($T_{eff} = 17500$ K) in our sample in order to explore the onset of non-LTE just above the temperature range of the stars we are studying. For this star, Nieva et al. (2012) find that the abundance of Si is essentially solar, with $\log N_{Si}/N_H = -4.49 \pm 0.05$. From our LTE analysis, it is found that the values of Si abundance, as measured with lines of Si ii (-5.34) and Si iii (-4.10), are inconsistent with one another, and with the value found by Nieva et al. (2012). The fact that with suitable choice of lines and appropriate non-LTE synthesis computations, the abundance of Si, like the other elements in this star that were measured by Nieva et al. (2012), have solar abundances indicate that stratification is probably not significant in this star. Instead, the problems in this star with the lines we are using are probably non-LTE effects.

We could try to test this conclusion by showing that non-LTE computation of our favoured lines in HD 160762 lead to an essentially solar, and consistent, abundance of Si. While we do not have the correct tools for this computation, we can try to use the non-LTE calculations of Becker & Butler (1990), who have computed non-LTE equivalent widths of a number of Si II and III lines over a large grid of T_{eff}, $\log g$, and ξ. We have measured the equivalent widths of a number of spectral lines in HD 160762, and used the tables of Becker & Butler (1990) to deduce corresponding Si abundances. The results of this exercise are shown in Table 4.5, together with our own LTE abundances from the same lines.

Assuming the correctness of the Si abundance of -4.49, we find that the Si abundance determined from lines of Si III, using the computations of Becker & Butler (1990) and interpolating to $\xi = 1$ km s^{-1}, is about -4.25, somewhat closer to the correct value than the LTE abundance of -4.10. In contrast, the non-LTE abundance deduced from lines of Si II appears to be nearly one dex low, as is the LTE Si II value. It thus seems that the computations of Becker & Butler (1990) for Si III multiplet (2) do not fully correct for non-LTE effects, and those for the optical lines of Si II do not even come close to correctly describing the non-LTE effects. (Note that the non-LTE treatment of Si II is still apparently unsatisfactory today; the model non-LTE spectra for early B stars shown by Nieva et al. (2012) in their Figs. 8 and 9 do not include any of the strong optical Si II lines.)

Our conclusion is that, by an effective temperature of about 17500 K, non-LTE effects almost certainly do undermine Si abundance determinations from LTE spectrum synthesis, especially for lines of Si II, but we are not at present able to quantify this effect, or even say how far down in effective temperature it reaches. The fact that Mashonkina et al. (2005, 2009) find important non-LTE effects in formation of lines of Pr and Nd II and III in magnetic Ap stars with T_{eff} as low as 7250 K suggests that non-LTE effects in Si could potentially be important well below the conventional limit of $T_{\mathrm{eff}} \approx 15000$ K.

4.5.2   Stratification

A rather different possible explanation for the Si II – Si III abundance discrepancies is the possibility that Si is not uniformly abundant with height in the atmosphere of the stars studied here. We have already mentioned this possibility earlier when we pointed out that the stars without the abundance discrepancy all show evidence of non-zero ξ values, and hence are presumed to have convective mixing present in the atmosphere, suggesting that these stars at least may have atmospheres that are too well mixed to support any kind of vertical non-uniform abundances. However, for most of the stars in this survey, we have no strong evidence of vertical mixing, and in the case of the magnetic stars, the large energy density in the magnetic fields almost

certainly quenches any convective turnover, so that vertical abundance stratification is quite possible.

As discussed above, vertical stratification has already been detected in rare earths in cool magnetic Ap stars by Ryabchikova et al. (2001), who found that Pr and Nd have substantially larger abundance relative to H in the upper atmospheres of pulsating magnetic (roAp) stars. This effect has been further studied by Kochukhov et al. (2009) and others cited in the Introduction. It now seems quite clear that stratification does occur to a very important extent in the cool magnetic Ap stars, and that it affects many chemical elements, including Si. Is there any evidence that stratification can explain the abundance discrepancies documented in this thesis?

We have carried out a series of simple experiments in which we introduce a simple smoothed step function of specified amplitude and at a specified optical depth τ_{5000} at 5000 Å. This was done using a slightly modified version of ZEEMAN that, given the optical depth and abundance change of the step, can optimise the fit to one or several spectral lines by adjusting the abundance below the step in the atmosphere. We mainly experimented on the two magnetic Bp stars BD+00 1659 and BD–19 5044L, both of which have T_{eff} values in the middle of our sample, around 12 500 K, and such low values of $v \sin i$ that we can study the fit to line profiles, not merely to equivalent widths. This is a far simpler scheme than the detailed modelling described, for example, by Kochukhov et al. (2006). However, it enables us to explore simply the plausibility of stratification as an explanation of the Si II–III discrepancy.

We have explored mainly step functions in which the abundance decreases outwards. The few experiments with Si concentrated high in the atmosphere lead to even larger discrepancies between the abundances determined from the two ionisation states than with an assumed uniform abundance. We have roughly explored abundance decreases of 1 or 2 dex, located typically between $\tau_{5000} = 0.2$ and 0.8. It is found that most such models substantially reduce the discrepancy between the abundances deduced from the two ion states, often to below 0.5 dex. With a decrease of 1 dex in Si abundance at $\tau_{5000} \sim 0.4$ the discrepancy can be reduced to as low as 0.3 dex. Larger steps of 2 dex lead to nominal agreement between the two ionisation stages, but also lead to wings on the Si II lines that are unacceptably broad (a problem that is only visible because we are studying stars of low $v \sin i$).

The conclusion of our limited experiments is that vertically non-uniform Si abundance, with a substantially lower abundance high in the atmosphere relative to $\tau_{5000} = 1$, can explain at least a large part of the discrepancy between abundances of Si deduced from the two ion states for magnetic Bp stars, and may entirely explain the Si II–III differences for normal and HgMn stars. Clearly more detailed stratification modelling of individual stars would be very illuminating. Similarly, further study of the non-LTE behaviour of the Si ions in the T_{eff} range of 10000 to 15000 K would be very valuable.

4.6   Summary

The results of our abundance analysis of the singly and doubly-ionised states of silicon in B-type stars are summarised as follows:

1. For a solar abundance of Si, we begin to detect Si III in main sequence stars at $T_{\text{eff}} \sim$ 11000 K.

2. All magnetic Bp stars have a discrepancy between the abundances derived from lines of Si II and Si III, with the latter being between 0.6 - 1.7 dex higher. The same discrepancy is observed in the non-magnetic stars, but to a much lesser extent, with an enhancement of the Si III abundance by between 0.3 - 0.8 dex.

3. Only three non-magnetic stars do not exhibit a discrepancy between the abundance of Si derived from both ionisation states. These are exactly the stars where we detect a non-zero microturbulence parameter: HD 22136 (normal), HD 57608 (HgMn), HD 27295 (HgMn). This suggests the presence of convective mixing in the atmospheres of these stars, inhibiting the development of any stratified abundance distribution.

4. Possible errors in the atomic data (of the order of ±0.1 dex) cannot explain this discrepancy. Although non-LTE effects in Si lines may be important, it is unclear to what extent these will influence the derived abundances below $T_{\text{eff}} \sim$ 15000 K.

5. Simple stratification models with a lower abundance high in the atmosphere relative to $\tau_{5000} = 1$ can explain a large part of the discrepancy between the derived abundances of Si II and Si III in the magnetic Bp stars, and may completely explain the phenomenon in the normal and HgMn stars.

   To fully understand the discrepancy noted between the abundances derived from the first and second ions of Si, more detailed stratification models are warranted. Further, studies of the non-LTE behaviour of Si below $T_{\text{eff}} = 15000$ K would reveal to what extent the observed discrepancy is influenced by non-LTE effects.

Bibliography

Babel, J. 1992, A&A, 258, 449

Bagnulo, S., Landstreet, J. D., Mason, E., et al. 2006, A&A, 450, 777

Bailey, J. D., Grunhut, J., Shultz, M., et al. 2012, MNRAS, 2947

Bailey, J. D., Landstreet, J. D., Bagnulo, S., et al. 2011, A&A, 535, A25

Becker, S. R. & Butler, K. 1990, A&A, 235, 326

Kelleher, D. E. & Podobedova, L. I. 2008, J. Phys. Chem. Ref. Data, 37, 1285

Kochukhov, O. 2006, A&A, 454, 321

Kochukhov, O., Tsymbal, V., Ryabchikova, T., Makaganyk, V., & Bagnulo, S. 2006, A&A, 460, 831

Kochukhov, O., Shulyak, D., & Ryabchikova, T. 2009, A&A, 499, 851

Kochukhov, O. & Bagnulo, S. 2006, A&A, 450, 763

Kunzli, M., North, P., Kurucz, R. L., & Nicolet, B. 1997, A&AS, 122, 51

Kupka, F., Piskunov, N. E., Ryabchikova, T. A., Stempels, N. C., & Weiss, W. W. 1999, A&A, 138, 119

Kupka, F. G., Ryabchikova, T. A., Piskunov, N. E., Stempels, H. C., & Weiss, W. W. 2000, Baltic Astronomy, 9, 590

Landstreet, J. D. 1988, ApJ, 326, 967

Landstreet, J. D. 1998, A&A, 338, 1041

Landstreet, J. D. 2011, A&A, 528, A132

Landstreet, J. D., Bagnulo, S., Andretta, V., et al. 2007, A&A, 470, 685

Landstreet, J. D., Barker, P. K., Bohlender, D. A., & Jewison, M. S. 1989, ApJ, 344, 876

Landstreet, J. D., Kupka, F., Ford, H. A., et al. 2009, A&A, 503, 973

Landstreet, J. D., Silaj, J., Andretta, V. et al. 2008, A&A, 481, 465

Mashonkina, L., Ryabchikova, T., & Ryabtsev, A. 2005, A&A, 441, 309

Mashonkina, L., Ryabchikova, T., Ryabtsev, A., & Kildiyarova, R. 2009, A&A. 495, 297

Napiwotzki, R., Schönberner, D., & Wenske, V. 1993, A&A, 268, 653

Neiner, C., Landstreet, J. D., Alecian, E. et al. 2012, A&A, 546, 44

Netopil, M., Paunzen, E., Maitzen, H. M., North, P., & Hubrig, S. 2008, A&A, 491, 545

Nieva, M.-F. & Przybilla, N. 2012, A&A, 539, A143

Pandey, C. P., Shulyak, D. V., Ryabchikova, T., & Kochukhov, O. 2011, MNRAS, 417, 444

Piskunov, N. E., Kupka, F., Ryabchikova, T. A., Weiss, W. W., & Jeffery, C. S. 1995, A&A, 112, 525

Przybilla, N., Nieva, M.-F., & Butler, K. 2011, Journal of Physics Conference Series, 328, 012015

Ryabchikova, T. A., Piskunov, N. E., Kupka, F., & Weiss, W. W. 1997, Baltic Astronomy, 6, 244

Ryabchikova, T. A., Savanov, I. S., Malanushenko, V. P., & Kudryavtsev, D. O. 2001, Astronomy Reports, 45, 382

Semenko, E. A., Kudryavtsev, D. O., Ryabchikova, T. A., & Romanyuk, I. I. 2008, Astrophysical Bulletin, 63, 128

Shulyak, D., Ryabchikova, T., Mashonkina, L., & Kochukhov, O. 2009, A&A, 499, 879

Sigut, T. A. A. & Landstreet, J. D. 1990, MNRAS, 247, 611

Wade, G. A., Bagnulo, S., Kochukhov, O., et al. 2001a, A&A, 374, 265

Wade, G. A., Ryabchikova, T. A., Bagnulo, S., & Piskunov, N. 2001b, in Astronomical Society of the Pacific Conference Series, Vol. 248, Magnetic Fields Across the Hertzsprung-Russell Diagram, ed. G. Mathys, S. K. Solanki, & D. T. Wickramasinghe, 373

Chapter 5

Time evolution of abundances in magnetic Bp stars

5.1 Introduction

The magnetic peculiar B-type (Bp) stars possess the strongest magnetic fields of main sequence stars, with the line-of-sight magnetic field $\langle B_z \rangle$ often of the order of 1 kG in strength or more. They host anomalous atmospheric abundances in their stellar spectra. The atmospheric chemistry compared to the Sun can be quite strikingly different, with the Fe-peak and rare-earth elements of the order of 10^2 and 10^5 times overabundant, respectively, whereas He is always underabundant. The mechanisms thought to be responsible for establishing these abundance anomalies are diffusion (the interplay between the gravitational settling and radiative levitation of elements into and out of the atmosphere) and chemical separation in the stellar wind driving mass loss (Michaud et al., 1976; Richer et al., 2000; Michaud, 2004; Krticka & Kubát, 2004).

The magnetic field structures of the magnetic Bp stars are approximately dipolar. Typically, magnetic Bp stars exhibit periodic variability (of the order of 1 to 10 days) in their spectra and magnetic field. These variations are explained by the oblique rigid rotator model, in which the magnetic field and line-of-sight are inclined at angles β and i to the rotation axis, respectively. The magnetic field sustains an inhomogeneous (or "patchy") distribution of chemical elements that are distributed non-axisymmetrically over the stellar surface. Therefore, as the star's framework rotates distinct portions of the surface are observed, resulting in changes in the line shapes and profiles, as well as different measurements in the magnetic field strengths.

Within the last decade, there has been substantial effort to characterise the evolution of magnetic field strengths during the main sequence lifetime of magnetic Bp stars. A systematic study of magnetic Bp stars that are members of open clusters (and therefore have known ages)

was made using ESO's FORS1 and CFHT's ESPaDOnS spectropolarimeters (Bagnulo et al., 2006; Landstreet et al., 2007, 2008). They were able to show that stars with masses between 2 - 5 $M_\odot$ have root-mean-square magnetic field strengths (B_{rms}) larger than about 1 kG near the zero-age main sequence (ZAMS) that decrease secularly towards the terminal-age main sequence (TAMS). The decay of the magnetic field is a function of stellar mass, with more massive stars (between 4 - 5 $M_\odot$) decreasing on shorter timescales. The less massive stars (2 - 3 $M_\odot$) appear to retain larger fields for a larger fraction of their main sequence lifetime.

This discovery leads naturally to questions about how the atmospheric chemistry of magnetic Bp stars may evolve during the main sequence lifetime. The ability to follow observationally the evolution of stars in a limited mass range with time also allows us to address fundamental questions, such as whether a link exists between magnetic field strength and chemical abundances and if these abundances are strongly sensitive to evolving stellar properties. The evolution of chemistry with time can provide useful observational constraints to advance studies of diffusion and mass loss from the surface of these stars. Understanding the impact of these processes in the atmospheres of magnetic Bp stars will provide insight into stars where these same mechanisms are at work in a much less pronounced way.

Until now, the study of atmospheric abundances of magnetic Bp stars has been restricted to mainly individual studies of specific stars. The detail of these studies vary from coarse models that roughly describe the magnetic field geometry and abundance variations over the stellar surface (e.g. Landstreet, 1988; Bailey et al., 2011, 2012) to more detailed maps of both the magnetic field structure and abundance distributions using spectroscopic observations in all four Stokes parameters (e.g. Kochukhov et al., 2004; Kochukhov & Wade, 2010). In this paper, we aim to broaden the scope of this research by performing an empirical study of atmospheric abundances of multiple elements for a larger collection of magnetic Bp stars. We selected stars from our own ESO and CFHT observing programmes (with one target taken from the ESO archive) that are confirmed to have magnetic fields and to be at least probable members of open clusters. The latter criterion ensures that each target has a well-known age with which to analyse any possible time evolution in abundances. We restricted our study to stars between about 3 - 4 $M_\odot$ because results may depend on mass and we did not wish to obscure any relationship that may be present in the data. Further, the main sequence lifetime is a strong function of mass, and we do not wish to confuse effects that depend in some fashion on physical time with ones that depend on the fraction of the main sequence lifetime completed. The following section discusses the stellar sample. Sect. 5.3 describes the modelling technique. Sect. 5.4 details the scientific results. Sect. 5.5 explores possible mechanisms to explain the observed trends and Sect. 5.6 outlines the main conclusions.

Table 5.1: Stars analysed in this study. Listed are the star designations, instrument used (with the number of spectra indicated in parentheses), spectral resolution, and spectral range.

Star	Instrument	R	λ (Å)
HD 45583	FEROS (2)	48000	3528-9217
HD 61045	ESPaDOnS (2)	65000	3690-10481
HD 63401	FEROS (2)	48000	3528-9217
HD 74535	FEROS (2)	48000	3528-9217
HD 133652	ESPaDOnS (1)	65000	3690-10481
	FEROS (1)	48000	3528-9217
HD 133880	ESPaDOnS (2)	65000	3690-10481
HD 147010	ESPaDOnS (2)	65000	3690-10481
HD 162576	ESPaDOnS (2)	65000	3690-10481
HD 162725	ESPaDOnS (2)	65000	3690-10481
HD 304842	FEROS (2)	48000	3528-9217
NGC 2169 12	UVES (1)	110000	3070-10398
BD+00 1659	ESPaDOnS (1)	65000	3690-10481
BD-19 5044L	ESPaDOnS (2)	65000	3690-10481
BD+49 3789	ESPaDOnS (2)	65000	3690-10481
HIP 109911	ESPaDOnS (2)	65000	3690-10481

5.2 Stellar data

This study aims to address the time evolution of atmospheric chemistry in magnetic Bp stars. To achieve this goal, our sample is limited to Bp stars that are members of clusters or associations and thus have a well-determined age. To a first approximation, each cluster has the same initial chemical composition. We further restrict the mass range of our study to stars between about 3 to 4 $M_\odot$, which is the best alternative to evolving one magnetic Bp star in time.

The spectra used for this study were largely taken from our own observing runs using the ESPaDOnS spectropolarimeter ($R = 65000$) at the Canada-France-Hawaii Telescope (CFHT) and the FEROS spectrograph ($R = 48000$) at the European Southern Observatory's (ESO) La Silla Observatory. The remaining spectrum of NGC 2169 12 was acquired from the ESO archive. The list of stars utilised is summarised in Table 5.1.

Landstreet et al. (2007) derived accurate effective temperatures T_{eff}, $\log t$ and evolutionary masses for our stellar sample, and determined their associated B_{rms} values. Further, Bailey & Landstreet (2013b) also derived accurate fundamental parameters of T_{eff} and $\log g$ using Geneva and $uvby\beta$ photometry for a large portion of our stellar sample. When no information was available in the literature, we also derived T_{eff} and $\log g$ from Geneva and $uvby\beta$ photometry. For the Geneva photometry, the FORTRAN program described by Kunzli et al. (1997) was

used. For the Strömgren *uvbyβ* photometry, we used a version of the FORTRAN program "UVBY-BETANEW" (see Napiwotzki et al., 1993) that corrects the $T_{\rm eff}$ of the magnetic Bp stars to the appropriate temperature scale (see Landstreet et al., 2007). When both sets of photometry were available, the average value was adopted. As discussed by Landstreet et al. (2007) and Bailey & Landstreet (2013b), the uncertainties in $T_{\rm eff}$ and $\log g$ were taken to be about ±500 K and 0.2 dex, respectively.

Table 5.2 lists the properties of each star including its designation, associated cluster, age, mass, $T_{\rm eff}$, $\log g$, $v \sin i$, and $B_{\rm rms}$. Where applicable, the appropriate reference is given for each parameter and when not listed, are derived from this study. The determination of $v \sin i$ is discussed later in this chapter. We note that the *photometrically* determined values of $T_{\rm eff}$ and $\log g$ vary systematically with age from about 13500 K/4.4 to 10000 K/3.5, which is as expected for the evolution of a single star of about 3.5 $M_{\odot}$ from ZAMS to TAMS.

5.3 Modelling technique

5.3.1 Spectrum synthesis

To model the atmospheric abundances of the magnetic Bp stars, the FORTRAN program ZEEMAN was used (see Landstreet, 1988; Wade et al., 2001a; Bailey et al., 2011). ZEEMAN is a spectral synthesis program for stars with magnetic fields that allows as input a magnetic field geometry which is modelled as a simple co-linear multipole expansion, with the angles between the rotation axis and the line-of-sight i and the magnetic field axis and the rotation axis β specified. ZEEMAN interpolates from a grid of ATLAS 9 atmospheric models an appropriate stellar atmospheric structure based upon the $T_{\rm eff}$ and $\log g$ provided. The atomic data are taken from the Vienna Atomic Line Database (VALD; see Kupka et al., 2000; Ryabchikova et al., 1997; Piskunov et al., 1995; Kupka et al., 1999). For all stars, a uniform atmospheric abundance distribution is assumed over the stellar surface. The microturbulence parameter ξ was set to 0 because the magnetic field suppresses any convective motion (no convection is expected or observed for magnetic stars between about 11000 to 14000 K).

ZEEMAN searches for an optimal fit between the synthetic and observed spectra by means of a reduced χ^2 fit. Multiple spectral windows can by synthesised simultaneously and ZEEMAN automatically provides as output the best values for the radial velocity v_R and $v \sin i$. Only one chemical element can be fit at a time, with the best abundance being found relative to H ($\log N_{\rm X}/N_{\rm H}$). The stars modelled vary in $T_{\rm eff}$ from about 10000 to 14000 K and therefore

Table 5.2: Physical properties of the stars studied.

Star	Cluster	$\log t$	M/M$_\odot$	T_{eff} (K)	$\log g$	$v \sin i$ (km s^{-1})	B$_{\text{rms}}$ (G)
HD 147010	Upper Sco	6.70 ± 0.10^a	3.15 ± 0.20^a	13000 ± 500^b	4.40 ± 0.20^b	15 ± 2^b	4825^a
NGC 2169 12	NGC 2169	6.97 ± 0.10^a	3.65 ± 0.15^a	13800 ± 500^a	4.30 ± 0.20	56 ± 5	3410^a
HD 133652	Upper Cen Lup	7.20 ± 0.10^a	3.35 ± 0.15^a	13000 ± 500	4.30 ± 0.20	48 ± 2	1120^a
HD 133880			3.20 ± 0.15^a	13000 ± 600^c	4.34 ± 0.16^c	103 ± 10^c	2300^a
HD 45583	NGC 2232	7.55 ± 0.10^a	3.30 ± 0.15^a	12700 ± 500^b	4.20 ± 0.20^b	70 ± 6^b	2730^a
HD 63401	NGC 2451	7.70 ± 0.10^a	3.70 ± 0.20^a	13500 ± 500^a	4.20 ± 0.20	52 ± 4	365^a
HD 74535	IC 2391	7.70 ± 0.15^a	3.85 ± 0.15^a	13600 ± 500^a	4.30 ± 0.20	45 ± 4	95^a
BD-19 5044L	IC 4725	8.02 ± 0.08^a	3.55 ± 0.15^a	12800 ± 500^b	4.50 ± 0.20^b	15 ± 3^b	235^a
BD+49 3789	NGC 7243	$8.06 \pm 0.10^*$	$3.55 \pm 0.15^*$	12900 ± 500^b	4.20 ± 0.20^b	85 ± 5^b	561^*
HIP 109911			$3.65 \pm 0.15^*$	13000 ± 500	4.30 ± 0.20	60 ± 2	348^*
HD 61045	NGC 2422	8.08 ± 0.11^a	3.85 ± 0.20^a	13000 ± 500^b	4.10 ± 0.20^b	64 ± 3^b	430^a
HD 304842	NGC 3114	8.13 ± 0.15^a	3.55 ± 0.15^a	12500 ± 500^b	3.90 ± 0.20^b	65 ± 5^b	20^a
BD+00 1659	NGC 2301	$8.22 \pm 0.10^*$	$3.65 \pm 0.15^*$	12500 ± 500^b	4.00 ± 0.20^b	7.0 ± 1^b	394^*
HD 162576	NGC 6475	8.41 ± 0.13^a	$3.10 \pm 0.15^*$	10300 ± 500	3.70 ± 0.20	28 ± 3	15^*
HD 162725			3.30 ± 0.20^a	10000 ± 500	3.50 ± 0.20	31 ± 3	69^*

REFERENCES – (a) Landstreet et al. (2007); (b) Bailey & Landstreet (2013b); (c) Bailey et al. (2012); (*) unpublished results

Table 5.3: List of spectral lines modelled.

Element	$\lambda(\text{Å})$	Comments
He I	4437	very weak, reliable
	4713	$v \sin i \lesssim 50$ km s^{-1}
	5015	$v \sin i \lesssim 20$ km s^{-1}
	5047	$v \sin i \lesssim 20$ km s^{-1}
	5876	clean, weak
O I	6155	reliable
	6156	reliable
	6158	reliable
	7771	possible nLTE
	7774	possible nLTE
	7775	possible nLTE
Mg II	4481	always present
Si II	4621	weak, all T_{eff}
	5041	$T_{\text{eff}} \lesssim$ 13-14000 K
	5055	$T_{\text{eff}} \lesssim$ 13-14000 K
	5056	$T_{\text{eff}} \lesssim$ 13-14000 K
Ti II	4533	slight Fe II blend
	4563	weaker
	4571	$v \sin i > 50$ km s^{-1}
Cr II	4558	
	4565	weak $\gtrsim 14000$ K
	4588	weak $\gtrsim 14000$ K
	4592	weak $\gtrsim 14000$ K
Fe II	4541	
	4555-56	near Cr II 4554
	4583	strong, clean
	5029	weak
	5030	$v \sin i \lesssim 60$ km s^{-1}
	5032	$v \sin i \lesssim 60$ km s^{-1}
	5035	$v \sin i \lesssim 70$ km s^{-1}
Pr III	6160	$v \sin i \lesssim 80$ km s^{-1}
	6161	$v \sin i \lesssim 80$ km s^{-1}
	7781	reliable for higher $v \sin i$
Nd III	4911	always reliable
	4912	always reliable
	4914	always reliable
	5050	$v \sin i \lesssim 30$ km s^{-1}
	6145	$v \sin i \lesssim 60$-70 km s^{-1}

share many spectral lines in common. Table 5.3 lists the lines used for modelling all the stars with our comments on the reliability of each line. For consistency, we endeavoured to deduce elemental abundances from the same sets of lines for all stars. Ideally, lines with a range of strengths in the same spectral window were used to deduce the final abundances, with uncertainties being estimated by manually changing the abundance in a spectral window until an unsatisfactory fit was achieved (determined by visual inspection). Unfortunately, ZEEMAN cannot model simultaneously spectral lines that are widely separated. In these instances, at least two lines (in different spectral windows) were fit separately and the average abundance between the lines was adopted. The uncertainty in this case was estimated from the observed scatter between the computed values of the different spectral lines.

We adopted the same modelling technique for the magnetic Bp stars as outlined by Bailey & Landstreet (2013b). All our stars have measurements of the line-of-sight magnetic field $\langle B_z \rangle$ either in the literature (see Bagnulo et al., 2006; Kochukhov & Bagnulo, 2006; Landstreet et al., 2008) or from our own unpublished results. For two of the stars in our sample (HD 133880 and HD 147010) magnetic field models were available from detailed studies performed by Bailey et al. (2012); Bailey & Landstreet (2013a), respectively. We therefore adopted their geometries. When no detailed magnetic field model was available, we simply adopted a dipolar magnetic field that was approximately three times B_{rms} and set i and β to zero.

The majority of the stars in our sample had multiple observations. In the cases where more than two spectra were available we chose the two that exhibited the greatest difference. In all cases the derived abundances are the average between the two modelled spectra with the associated uncertainties propagated accordingly.

5.3.2　Measured abundances

A total of 15 cluster magnetic Bp stars between 3-4 $M_\odot$ were studied for their atmospheric abundances of He, O, Mg, Si, Ti, Cr, Fe, Pr and Nd. In Tables 5.4 and 5.5 we tabulate the mean abundances for each star. The first three columns recall the star designation, age ($\log t$) and T_{eff} from Table 5.2. The subsequent columns list the average abundance values, with their associated uncertainties, for He, O, Mg, and Si II (Table 5.4), as well as Ti, Cr, Fe, Pr and Nd (Table 5.5). We note that we did not derive abundances for lines of Si III due to the discrepancies in the derived abundances between their first and second ionisation states (Bailey & Landstreet, 2013b). For reference, the solar abundance ratios of Asplund et al. (2009) are also shown. Fig. 5.1 provides an example of the quality of fits we achieved for each star.
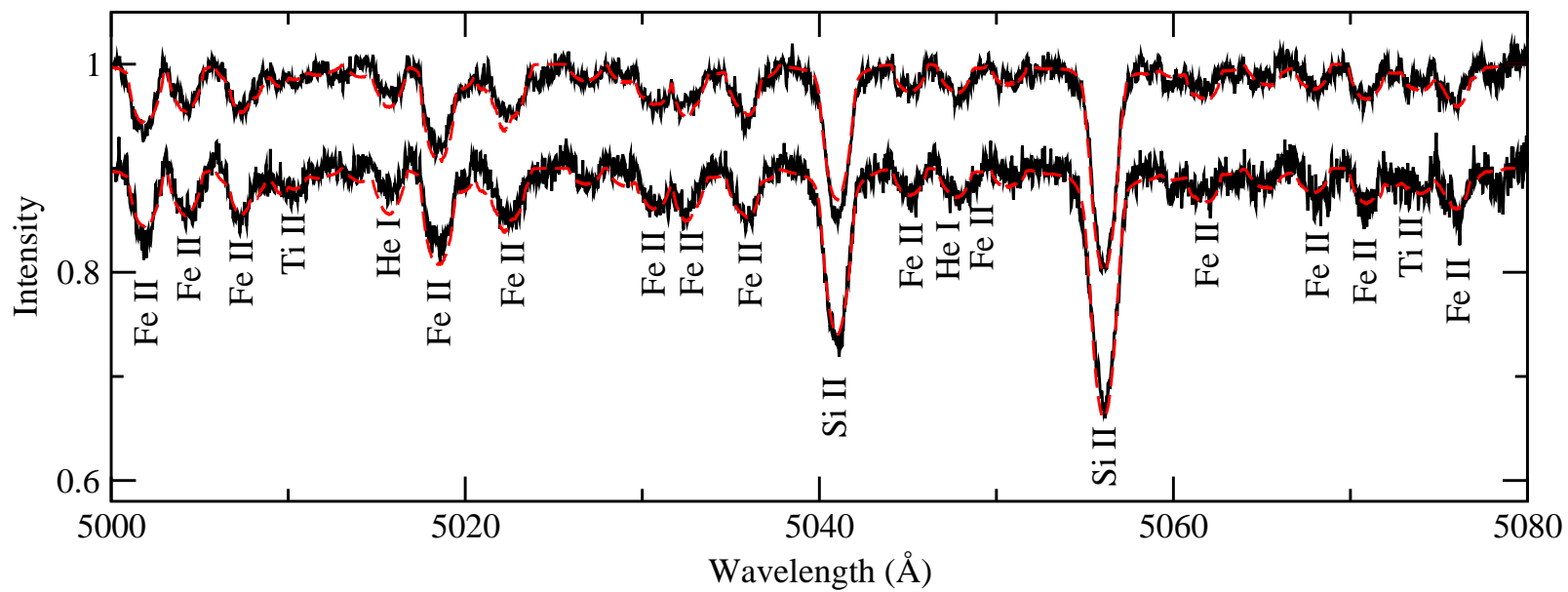
Figure 5.1: Spectrum synthesis of the region 5000 - 5080 Å for two spectra of HIP 109911. The observed spectra are in black and the model fits are in red.

Table 5.4: Average derived abundances for the stars studied.

Star	log t	T_{eff} (K)	log(He/H)	log(O/H)	log(Mg/H)	log(Si ɪɪ/H)
Sun						
			−1.07	−3.31	−4.40	−4.49
magnetic Bp stars						
HD 147010	6.70 ± 0.10[a]	13000 ± 500[b]	−3.11 ± 0.28	−4.49 ± 0.28	−5.67 ± 0.14	−3.72 ± 0.14
NGC 2169 12	6.97 ± 0.10[a]	13800 ± 500[a]	−3.09 ± 0.30	−3.88 ± 0.15	−5.56 ± 0.15	−3.87 ± 0.15
HD 133652	7.20 ± 0.10[a]	13000 ± 500	−3.16 ± 0.28	−3.87 ± 0.28	−5.18 ± 0.14	−3.36 ± 0.28
HD 133880		13000 ± 600[c]	≤ −2.00	−2.90 ± 0.42	−4.12 ± 0.28	−2.94 ± 0.28
HD 45583	7.55 ± 0.10[a]	12700 ± 500[b]	≤ −2.40	−3.61 ± 0.42	−4.19 ± 0.28	−3.34 ± 0.28
HD 63401	7.70 ± 0.10[a]	13500 ± 500[a]	−2.64 ± 0.28	−3.73 ± 0.21	−5.86 ± 0.14	−3.96 ± 0.14
HD 74535	7.70 ± 0.15[a]	13600 ± 500[a]	−2.52 ± 0.28	−4.26 ± 0.28	−5.44 ± 0.28	−4.28 ± 0.14
BD-19 5044L	8.02 ± 0.08[a]	12800 ± 500[b]	−2.16 ± 0.21	−3.99 ± 0.28	−5.44 ± 0.21	−3.94 ± 0.28
BD+49 3789	8.06 ± 0.10*	12900 ± 500[b]	−2.52 ± 0.35	−3.60 ± 0.22	−5.25 ± 0.25	−3.54 ± 0.14
HIP 109911		13000 ± 500	−2.34 ± 0.28	−3.69 ± 0.21	−5.38 ± 0.14	−3.49 ± 0.14
HD 61045	8.08 ± 0.11[a]	13000 ± 500[b]	−2.06 ± 0.28	−3.72 ± 0.28	−5.10 ± 0.14	−3.94 ± 0.28
HD 304842	8.13 ± 0.15[a]	12500 ± 500[b]	−1.54 ± 0.28	−3.78 ± 0.25	−5.76 ± 0.21	−3.64 ± 0.28
BD+00 1659	8.22 ± 0.10*	12500 ± 500[b]	−2.34 ± 0.15	−3.58 ± 0.10	−5.62 ± 0.10	−3.53 ± 0.20
HD 162576	8.41 ± 0.13[a]	10300 ± 500	−1.51 ± 0.28	−3.77 ± 0.28	−5.34 ± 0.14	−4.44 ± 0.14
HD 162725		10000 ± 500	−1.74 ± 0.36	−3.77 ± 0.28	−5.23 ± 0.14	−3.54 ± 0.28

REFERENCES – (a) Landstreet et al. (2007); (b) Bailey & Landstreet (2013b); (c) Bailey et al. (2012);
(*) unpublished results

Table 5.5: Average derived abundances for the stars studied continued.

Star	$\log t$	T_{eff} (K)	log(Ti/H)	log(Cr/H)	log(Fe/H)	log(Pr/H)	log(Nd/H)
Sun							
			−7.05	−6.36	−4.50	−11.28	−10.58
magnetic Bp stars							
HD 147010	6.70 ± 0.10[a]	13000 ± 500[b]	−5.68 ± 0.21	−4.04 ± 0.14	−3.33 ± 0.14	−6.15 ± 0.28	−6.50 ± 0.28
NGC 2169 12	6.97 ± 0.10[a]	13800 ± 500[a]	−5.90 ± 0.20	−4.80 ± 0.20	−3.76 ± 0.10	−7.31 ± 0.20	−7.21 ± 0.20
HD 133652	7.20 ± 0.10[a]	13000 ± 500	−5.01 ± 0.21	−4.17 ± 0.21	−2.90 ± 0.14	−6.98 ± 0.28	−6.42 ± 0.28
HD 133880		13000 ± 600[c]	−5.44 ± 0.28	−4.65 ± 0.21	−3.56 ± 0.14	−6.96 ± 0.28	−7.04 ± 0.42
HD 45583	7.55 ± 0.10[a]	12700 ± 500[b]	−5.68 ± 0.28	−4.74 ± 0.21	−3.43 ± 0.21	−7.49 ± 0.42	−7.04 ± 0.42
HD 63401	7.70 ± 0.10[a]	13500 ± 500[a]	−6.44 ± 0.28	−5.32 ± 0.28	−3.84 ± 0.14	−7.14 ± 0.28	−7.44 ± 0.28
HD 74535	7.70 ± 0.15[a]	13600 ± 500[a]	−6.29 ± 0.28	−5.65 ± 0.14	−4.02 ± 0.28	−8.15 ± 0.21	−7.52 ± 0.28
BD-19 5044L	8.02 ± 0.08[a]	12800 ± 500[b]	−6.82 ± 0.28	−5.88 ± 0.28	−4.24 ± 0.28	−8.12 ± 0.28	−7.88 ± 0.42
BD+49 3789	8.06 ± 0.10[*]	12900 ± 500[b]	−6.33 ± 0.35	−5.44 ± 0.28	−4.06 ± 0.28	−7.72 ± 0.28	−7.72 ± 0.25
HIP 109911		13000 ± 500	−5.90 ± 0.28	−5.35 ± 0.28	−3.59 ± 0.28	−7.70 ± 0.28	−7.37 ± 0.28
HD 61045	8.08 ± 0.11[a]	13000 ± 500[b]	−6.24 ± 0.28	−5.47 ± 0.28	−3.98 ± 0.28	−7.74 ± 0.28	−7.77 ± 0.42
HD 304842	8.13 ± 0.15[a]	12500 ± 500[b]	−6.83 ± 0.14	−6.05 ± 0.32	−4.35 ± 0.32	−7.65 ± 0.36	−7.04 ± 0.28
BD+00 1659	8.22 ± 0.10[*]	12500 ± 500[b]	−6.69 ± 0.10	−5.02 ± 0.10	−3.79 ± 0.10	−8.11 ± 0.20	−7.34 ± 0.20
HD 162576	8.41 ± 0.13[a]	10300 ± 500	−7.72 ± 0.14	−5.12 ± 0.14	−3.95 ± 0.14	−10.15 ± 0.42	−9.10 ± 0.42
HD 162725		10000 ± 500	−7.30 ± 0.28	−4.64 ± 0.22	−3.66 ± 0.28	−8.32 ± 0.42	−7.44 ± 0.28

REFERENCES − (a) Landstreet et al. (2007); (b) Bailey & Landstreet (2013b); (c) Bailey et al. (2012); (*) unpublished results

From the study of Bailey & Landstreet (2013b), we know that serious discrepancies (of the order of 1 dex) are found between abundances derived from lines of Si ɪɪ compared to those derived using lines of Si ɪɪɪ, and that this situation exists in most or all magnetic stars in the T_{eff} range of this study. That study suggests that this discrepancy is mostly due to strong stratification of Si, rather like the stratification profiles computed by Leblanc et al. (2009) and shown in their Fig 9. Stratification has also been detected in the vertical distribution of Fe (e.g. Wade et al., 2001b; Ryabchikova et al., 2005), and in the distribution of other elements, mainly in cool magnetic Ap stars. However, we expect this phenomenon to occur in the T_{eff} range discussed in this chapter as well. Because both observation (e.g. Ryabchikova et al., 2004a) and theory (e.g. Leblanc et al., 2009) suggest that the vertical abundance variations may be of the order of 1 dex or more, this phenomenon raises quite serious doubt about the meaning of atmospheric chemical abundances derived assuming that the elements are uniformly distributed in the vertical direction. (This is similar to the ambiguity of meaning of abundances derived for patchy stars with models assuming uniform horizontal abundance.)

Up to now, chemical stratification in magnetic Bp stars hotter than about 10000 K has not been studied in detail. In the absence of established methods that would enable us to derive well-defined mean abundance values for the atmospheres studied here, for the present study we fall back on an operational abundance measurement method. The typical symptom of abundance stratification is that a model spectrum that fits lines of intermediate strength of an element predicts lines that are too strong for the strongest lines, and too weak for the weakest lines (see e.g. Figs. 2 and 3 of Ryabchikova et al., 2004a). Thus, by simply fitting, on average, the spectral lines of the element under study, we hypothesise that we are deriving a fairly stable mean abundance, which has a similar meaning in stars that do not differ greatly in T_{eff}. However, the ambiguity due to probable vertical stratification must be kept in mind in evaluating our results.

5.4   Results

Having acquired a substantial set of magnetic Bp stars with measured abundances of 9 elements, we aimed to determine if any trends could be seen with various stellar parameters. We explored the possibilities of trends of atmospheric abundances with rotation period, $v \sin i$, T_{eff}, mass, $\log t$, and B_{rms}. Within the limitations of our sample, no obvious trends were found with rotation period, $v \sin i$, T_{eff} or mass. We discuss in further detail below results for $\log t$ and B_{rms}.

Table 5.6: Linear fit parameters.

y-axis	x-axis	Slope	σ_D
log(He/H)	$\log t$	0.76 ± 0.18	4.2
	$\log B_{\mathrm{rms}}$	-0.48 ± 0.11	4.4
log(O/H)	$\log t$	0.13 ± 0.17	0.76
	$\log B_{\mathrm{rms}}$	0.04 ± 0.13	0.31
log(Mg/H)	$\log t$	-0.15 ± 0.26	0.58
	$\log B_{\mathrm{rms}}$	0.20 ± 0.18	1.1
log(Si/H)	$\log t$	-0.13 ± 0.20	0.65
	$\log B_{\mathrm{rms}}$	0.19 ± 0.13	1.5
log(Ti/H)	$\log t$	-1.07 ± 0.27	4.0
	$\log B_{\mathrm{rms}}$	0.69 ± 0.12	5.8
log(Cr/H)	$\log t$	-0.97 ± 0.24	4.0
	$\log B_{\mathrm{rms}}$	0.40 ± 0.16	2.5
log(Fe/H)	$\log t$	-0.41 ± 0.16	2.6
	$\log B_{\mathrm{rms}}$	0.24 ± 0.08	3.0
log(Pr/H)	$\log t$	-1.29 ± 0.29	4.4
	$\log B_{\mathrm{rms}}$	0.88 ± 0.20	4.4
log(Nd/H)	$\log t$	-0.81 ± 0.24	3.4
	$\log B_{\mathrm{rms}}$	0.46 ± 0.17	2.7

5.4.1   Variations with age of abundances during the main sequence

All of our stars have well-determined ages. Figure 5.2 plots the abundances of each star for the 9 elements studied in this chapter versus $\log t$. Shown are the solar abundance ratios (solid red line) and the best-fit linear regression to the data (dashed blue line). Table 5.6 tabulates the slope of the best-fit line with its respective uncertainty, as well as the significance of the slope. We discuss individual elements below.

Helium

One of the defining properties of magnetic Bp stars is the fact that they are underabundant in He compared to the Sun. This is true of all of the magnetic Bp stars in our sample. Interestingly, we observe a clear evolutionary increase in the abundance of He with time. Substantial underabundances (of the order of 2 dex compared to the Sun) are only seen in stars near the ZAMS. The oldest stars in our sample (nearer the TAMS) show only modest underabundances of He that are about 0.5 dex less than in the solar ratio.

Oxygen, magnesium and silicon

No apparent trend in chemistry with age is seen in oxygen, magnesium or silicon. In general, both oxygen and magnesium are underabundant compared to the solar abundance ratios with few exceptions. For oxygen, only HD 133880 is overabundant compared to the Sun as well-documented by Bailey et al. (2012). HD 133880 and HD 45583 have nearly solar abundances of magnesium. These two stars have very similar stellar parameters which may influence the measured abundances. Of note are the fact that they have comparable masses, $v \sin i$, $\log g$, and B_{rms}. In general, silicon appears to be overabundant compared to the solar abundance ratio, regardless of age. The strong Si overabundance is common for magnetic Bp stars between effective temperatures of about 10000 and 15000 K. The peak values (around -3 dex) appear to occur in stars with relatively large magnetic fields ($B_{\mathrm{rms}} \gtrsim 1000$ G).

Fe-peak and rare-earth elements

With the Fe-peak (Ti, Cr, and Fe) and rare-earth elements (Pr and Nd) a distinct decrease in atmospheric abundances are observed with time. In all cases, younger magnetic Bp stars have higher abundances of Fe-peak elements that decrease with age. For the Fe-peak elements, the older stars apparently approach solar values, whereas the rare-earth elements remain overabundant by at least about 2 dex.

5.4.2   Trends in atmospheric abundances with magnetic field strength

Landstreet et al. (2008) discovered that magnetic field strength decreases during the main sequence lifetime of magnetic Bp stars. Since we see trends in abundance with time for He, Ti, Cr, Fe, Pr and Nd, it is logical to assume that these trends should also be apparent with magnetic field strength. Fig. 5.3 plots abundances versus $\log B_{\mathrm{rms}}$ in the same manner as for $\log t$. In all the elements for which a trend was observed versus time (He, Ti, Cr, Fe, Pr and Nd), one is also seen versus $\log B_{\mathrm{rms}}$, but in the opposite sense: helium abundance decreases with increasing magnetic field strength and the Fe-peak and rare-earth elements increase in abundance with increasing magnetic field strength. This is consistent with the results of Landstreet et al. (2007, 2008). We note that this seems to be the explanation of the correlation between the Geneva photometric measurements of the 5200 Å depression (using the Z index) and field strength, as discussed by Cramer & Maeder (1980). This effect has also been exploited recently by the Special Astrophysical Observatory (SAO) group (e.g. Kudryavtsev et al., 2006; Kudryavtsev & Romanyuk, 2008; Kudryavtsev et al., 2011) to search for particularly large magnetic fields in Ap/Bp stars.
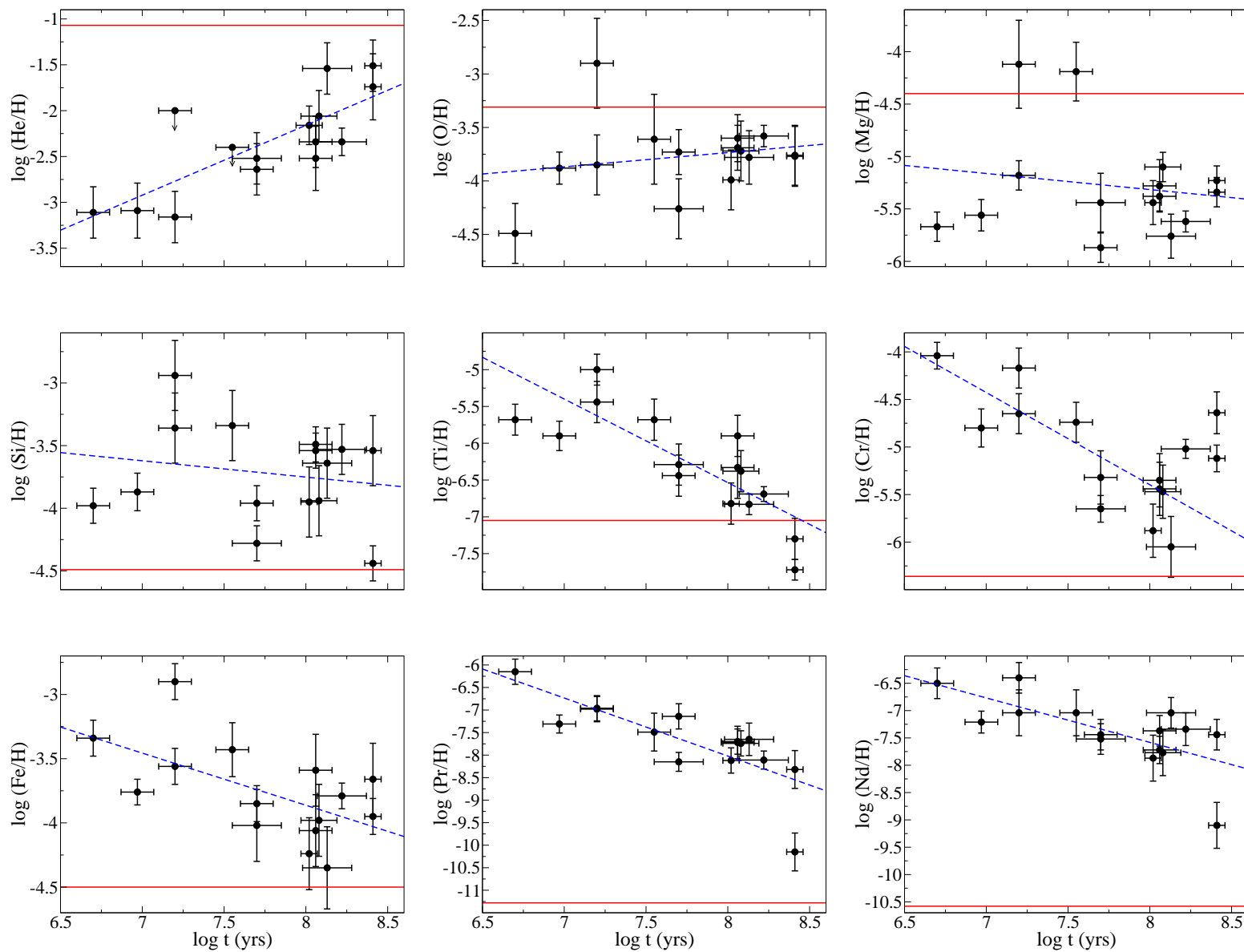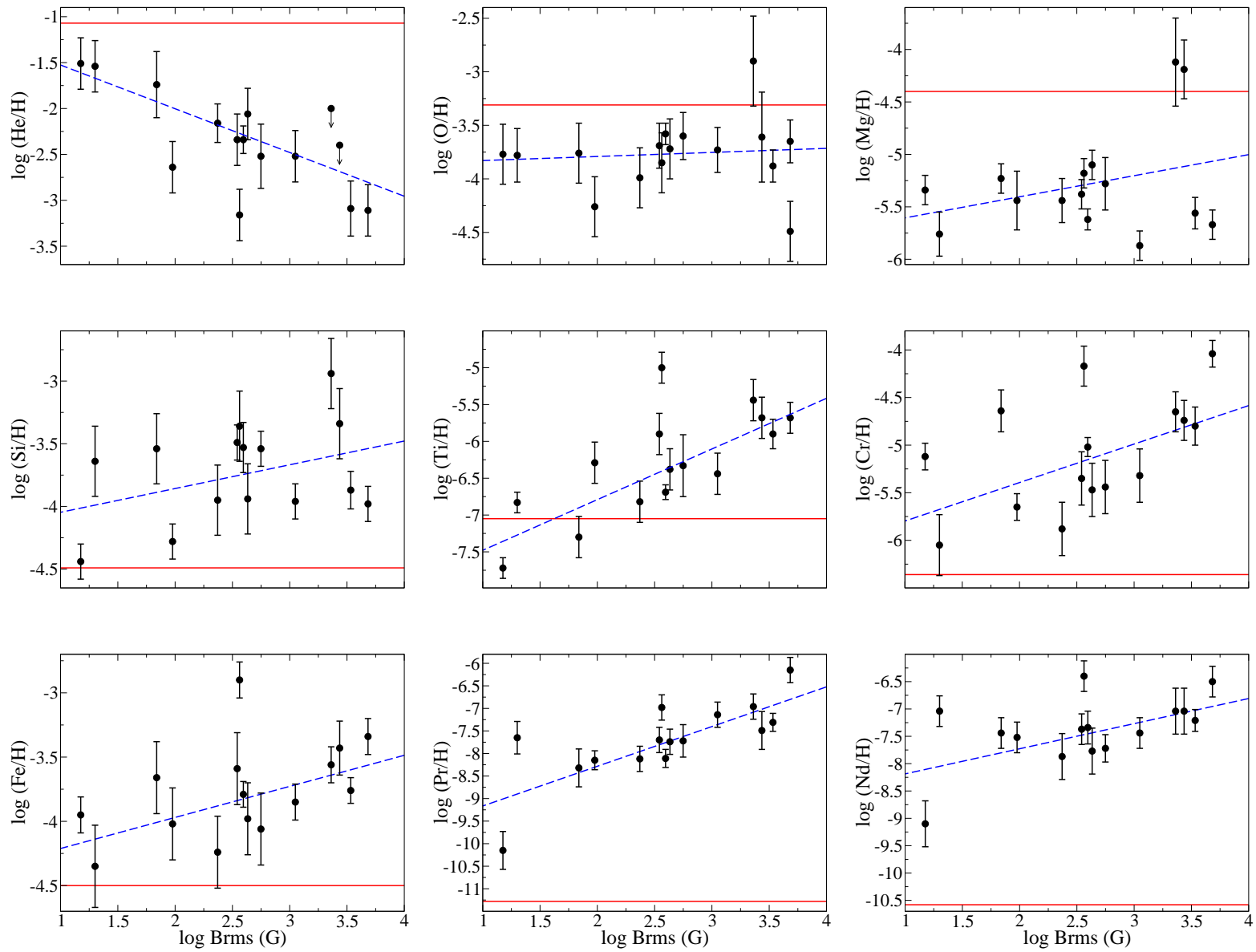
Figure 5.2: Shown are the atmospheric abundances of He, O, Mg, Si, Ti, Cr, Fe, Pr, and Nd plotted against $\log t$. Each plot contains the solar abundance ratio for that element (solid red line) and the best-fit linear regression (dashed blue line).

Figure 5.3: Same as Fig. 5.2 but for B_{rms}.
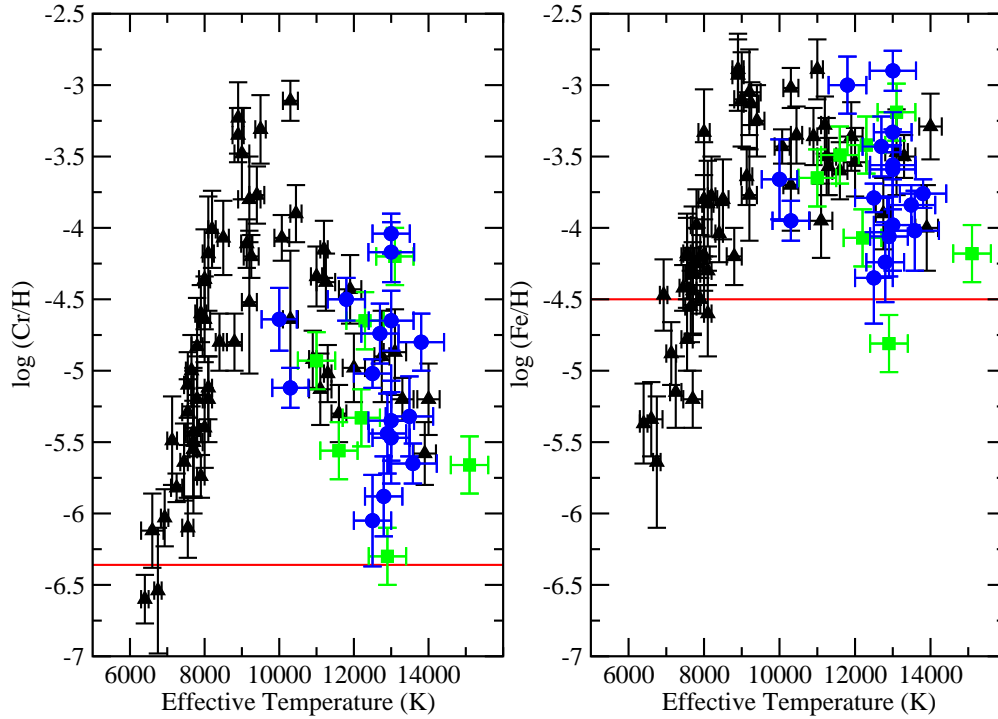
Figure 5.4: Shown are Cr (left) and Fe (right) abundances verses T_{eff}. The black triangles are data taken from Ryabchikova et al. (2004b) and Ryabchikova (2005), the green squares are from Bailey & Landstreet (2013b) and the blue circles are data from this chapter.

5.4.3 Cr and Fe abundances versus effective temperature

In addition to the goals of this chapter, our results can be used to compare to previous studies of magnetic Bp stars. Ryabchikova et al. (2004b) presented a comprehensive comparison of Cr and Fe abundances in roAp (rapidly oscillating Ap) stars versus effective temperature. However, their study was mostly restricted to stars at or below around 10000 K. Ryabchikova (2005) added stars between about 10000 and 15000 K and our current study, as well as a previous study by Bailey & Landstreet (2013a), add 23 stars in that same temperature range. The results are shown in Fig. 5.4. The hotter temperature regime (above about 10000 K) exhibits marginally larger scatter than the cooler temperatures (below about 10000 K). This may be in part due to the larger uncertainties in the temperature determinations of the hotter stars. Regardless, it appears that for Cr the largest observed abundances peak at around 10500 K and decline with increasing effective temperature. A similar trend is seen with Fe, but to a lesser extent. There is no obvious peak in the abundance of Fe with T_{eff} however the abundance does seem to decrease with increasing T_{eff} towards the solar ratio. These results support the conclusions of Ryabchikova et al. (2004b) that the maximum abundance for Cr and Fe both approach the same value of about -3 dex (perhaps closer to -4 dex in the case of Cr).

5.5   Discussion

5.5.1   General ideas

It is generally believed that the peculiar chemical abundances found in the atmospheres of magnetic Ap and Bp stars are the result of microscopic diffusion, possibly in competition with other processes such as turbulent diffusion, convection, meridional circulation, well-mixed mass loss, accretion, and the effects of a magnetic field.

The basic ideas of how diffusion can lead to anomalous atmospheric abundances are discussed, for example, by Michaud et al. (1976) and by Vauclair (1983). Essentially, in a quiescent stellar plasma in a gravitational field but having an isotropic radiation field, the trace atoms will tend to diffuse downward relative to the dominant hydrogen gas. However, in a star, the outward flow of radiation from centre to surface leads to a radiation pressure on these trace atoms which, if these trace atoms absorb at many wavelengths and are not too numerous, can levitate trace atoms into and through the atmosphere.

The average upward acceleration per ion of a particular species depends on the intensity of the radiation (which increases with effective temperature T_{eff}), on the specific atomic transitions that the ion can undergo (especially those arising from low-lying energy levels), and on the number density of the trace ion. In general, as the fractional number density of the trace ion increases, the acceleration per ion decreases. For many trace ions of low abundance (having, say, number density less than about 10^{-6} that of H) in stars of T_{eff} above about 7000 K, the upward acceleration g_{R} due to the radiation field is larger than the local acceleration of gravity g, and the ion diffuses upwards rather than downward. In slowly rotating middle main sequence stars, which have relatively weak mixing near the surface, this phenomenon can lead to anomalous chemical abundances in the stellar atmospheres.

The actual vertical variation of radiative acceleration for various ions in specific stellar models has been calculated by a number of groups. The calculations fall into two general types. Because the acceleration per ion decreases as the fractional abundance of the ion increases (due to saturation of the spectral lines that the ion absorbs), an ion which is levitated at low abundance can become locally abundant enough that $g_{\text{R}} = g$, a situation in which the tendency of that trace ion to diffuse upwards or downwards vanishes. It is possible to determine the fractional abundance for a specific atom as a function of position in a region (e.g. with height in the stellar atmosphere) for which this condition is satisfied everywhere in the region, and diffusion of this atom ceases. The run of abundance through the region satisfying this condition is known as the "equilibrium abundance distribution". Some recent computations of equilibrium abundance distributions in the atmospheres of the late B stars discussed in this chapter are reported by LeBlanc (2003), Leblanc et al. (2009) and Stift & Alecian (2012).

Recent work in this field has focussed on re-computing the structure of atmospheres in which equilibrium abundance distribution computations suggest the presence of strong vertical variations in abundance, in order to have the atmospheric structure be consistent with the abundance stratification (LeBlanc, 2003; Leblanc & Monin, 2004; Shulyak et al., 2009; Leblanc et al., 2009; Stift & Alecian, 2012). It is found that when large variations in abundances of abundant elements with altitude are present, the atmospheric structure is substantially perturbed.

However, an equilibrium abundance distribution may not be achievable in a region if not enough atoms of the species is available from below. In this second case, atoms may diffuse slowly up into the region from below and at the same time be removed from the top. This situation could settle into a stationary state in which the flux of atoms through the region is constant with height, and the abundance distribution is unchanging but not the equilibrium abundance. In principle, if a large enough volume of the star is considered, the evolution of abundance of an atom with radius, including through the atmosphere, could be computed as a function of time. Because the time-scale for evolution varies strongly with density, this is a stiff problem. Solutions on the scale of a stellar envelope, to try to explain the chemical abundances in the atmospheres of metallic-line (Am) stars, including either a (mixed) stellar wind or deep, but weak, turbulent mixing have been reported by Vick et al. (2010, earlier work on abundance evolution is cited there).

The time variation with height of abundance of a very unabundant element diffusing up through a stellar atmosphere has recently been studied by Alecian et al. (2011), who find that a stationary state of constant particle flux with height is generally achieved after a few hundred years, provided that the atoms continue to diffuse out of the top of the atmosphere. The actual value of the flux, and the run of abundance with height, is set by the abundance of the atom supplied at the bottom of the atmosphere from the reservoir below. We will refer to this situation as "stationary flow-through".

We now apply these general ideas to the elements studied here, in stellar atmospheres of $\log g \sim 4$ and $T_{\text{eff}} \sim 10 - 13\,000$ K. In the panels of Figure 5.2, it appears that we can identify several rather different cases.

5.5.2 Abundant light elements: He, O

The general behaviour of these elements was already predicted by Michaud et al. (1976). For the very abundant light elements He and O, the radiative acceleration for $T_{\text{eff}} \sim 12000$ K is much too weak to support a solar abundance of these elements (cf g_{rad} calculations for $T_{\text{eff}} = 12000$ K by Hui-Bon-Hoa et al. 2002). These two elements are expected to diffuse downward

into the stellar envelope below the atmosphere until the relative abundance has fallen enough that radiative acceleration can support them in the atmosphere. Consequently, He and O are expected to have abundances well below the solar values, and this is observed.

The diffusion of He in stellar atmospheres with well-mixed winds (including H) has been studied in more detail by Vauclair et al. (1991), Krticka & Kubát (2004) and Théado et al. (2005); all groups confirm that without a mixed wind from the star, that He should diffuse downward until quite low relative abundance is reached. However, we know of no published predictions of how low the He abundance should drop before an equilibrium distribution is achieved. It may well be that some degree of turbulent mixing with sub-atmospheric layers is required to keep the abundance of He as large as is observed (Figure 5.2).

The *increase* in He abundance with stellar age that we observe is particularly unexpected. Radiative levitation is so weak (due to the shadowing of resonance lines of He I by the very strong H continuum bound-free absorption below the Lyman limit) that it is not expected to play a significant role in the observed He abundance, and especially not in its increase with decreasing T_{eff}. The observed increase of He abundance towards the solar mixing ratio suggests either that there is significant and increasing mixing upward of envelope He by some process unrelated to diffusion, or that there is accretion of (He-rich) interstellar gas.

Landstreet et al. (1998) have studied the diffusion of O in stars in our mass range, using a simple approximation to estimate the radiative acceleration. Extrapolating their results, it appears that radiation may be able to support O at an abundance one to two dex below the solar abundance. This conclusion is supported by the very small g_{rad} value for O at 12000 K found by Hui-Bon-Hoa et al. (2002). The rather mild underabundance of O that we observe (about 0.5 dex) is probably higher than the level that would be found by an equilibrium abundance calculation. Furthermore, as the stars in our sample age, T_{eff} and $\log g$ both decrease. The change in T_{eff} is expected to reduce g_{R}. However, the decrease in $\log g$ means that a smaller value of g_{R} is required to support ions of O, which in turn means that a larger abundance can be supported. It is not clear which of these two effects dominates, and in fact the observed lack of significant variation in the O abundance with age suggests that if the observed abundance is the result of radiative levitation, the two effects roughly cancel.

We do not have any explanation at present for the slight overabundance of O observed for a single star, HD 133880.

It would clearly be of interest to have available some published results of computed equilibrium abundances of He and O in our temperature range, and especially to have such calculations follow the evolution of a star of $3.5 M_{\odot}$ from $T_{\mathrm{eff}} = 13000$ K and $\log g = 4.5$ to $T_{\mathrm{eff}} = 10000$ K and $\log g = 3.5$, in order to determine the importance of radiative levitation of He and O in the observed abundance evolution of the stars of our study.

5.5.3 Light metals: Mg and Si

The Mg abundance, based generally only on the 4481 Å line of Mg II, appears to be about 1 dex below the solar abundance, or $\log(n_{Mg}/n_H) \approx -5.2$. This may be compared with the predicted Mg abundance profile for a star of T_{eff} = 12000 K of Leblanc et al. (2009) and of Alecian & Stift (2010). The abundance predicted by the equilibrium calculation ($g_R = g$ throughout the atmosphere) is mildly non-uniform through the line-forming region, but is of about this same value. Thus it appears that Mg may be an element in which the supply of atoms from below has been large enough to allow the development of an equilibrium stratification. No strong trend of abundance with age is observed.

We have no explanation at present for the two stars (HD 133880 and HD 45583) that deviate strongly from the mean behaviour, with Mg abundances about 1 dex larger than other, younger and older, stars.

Since Mg may well be described in the stars of our sample by the equilibrium abundance distribution, it would be of great interest to have calculations of the equilibrium atmospheric abundance of Mg following the evolution of T_{eff} and $\log g$ for our $3.5M_\odot$ stars.

Silicon equilibrium atmospheric abundance has been studied by a number of authors, including Alecian & Vauclair (1981), Leblanc et al. (2009), and Alecian & Stift (2010). While detailed results differ, the overall conclusion is that Si is expected to be of order 1 dex underabundant in the atmosphere at $T_{eff} \sim 12000$ K. Instead, as has been found in the past, we observe an overabundance of about 1 dex at all ages. This situation has been a long-standing puzzle. Because it is not clear how to obtain an atmospheric abundance that is nearly 2 dex larger that the maximum value that can be supported by radiation pressure, various explanations have been probed, such as support by a horizontal magnetic field, non-LTE effects, etc, but none have been found to offer convincing explanations of the observed overabundance at all ages.

5.5.4 Iron peak elements: Ti, Cr and Fe

Expected abundances for these elements based on equilibrium have recently been computed for stars in our mass range by Leblanc et al. (2009), Alecian & Stift (2010), and (for Fe) by Stift & Alecian (2012). The results are most extensive for iron. The computed equilibrium abundances are only qualitatively in agreement with one another, and depend on still uncertain physics, particularly on how to treat redistribution of momentum between ionisation stages, but also on the effects of the magnetic field, and the chemical composition assumed for the computation. However, all the computations of equilibrium abundances agree that Fe in the line-forming region of stars in our mass range should reach equilibrium at an abundance of

around -3 to -3.5 dex relative to H. This is reasonably consistent with the values that we observe (Figure 5.2), so this may well be an element for which the equilibrium assumption of zero diffusion is approximately correct. This implies that an adequate supply of Fe ions is available from below the atmosphere to replenish atmospheric atoms lost to space during the initial period of equilibration, and to keep the abundance high enough to satisfy the equilibrium condition.

It is clear from the few values of T_{eff} for which equilibrium Fe abundances have been computed that the radiative acceleration and the equilibrium abundance decrease with decreasing effective temperature. However, there is no computational information on how the equilibrium abundance varies as $\log g$ decreases from 4.5 to 3.5, except for the qualitative result that the effect of the decrease in $\log g$ should be to make it possible for a given radiative force to support more atoms. Since the observed evolution of Fe abundance is that the abundance decreases with time, it appears that the decrease in radiative acceleration with decreasing T_{eff} may dominate. This is certainly a question that could be studied by computing an appropriate series of equilibrium abundance models following the evolution of a $3.5 M_{\odot}$ star

The available equilibrium calculations for Ti and Cr in the mass range of our observations by Leblanc et al. (2009) have been cut off in the line-forming region because of artificial limits of 1000 times the solar abundances imposed on the calculations. Thus we may suppose that without these limits, the equilibrium calculations would imply equilibrium abundances of Ti and Cr of $\log(n_{\text{el}}/n_{\text{H}})$ similar to those of Fe, in the range of -3 to -4. This is confirmed by the calculations of Alecian & Stift (2010). Although we observe overabundances of these two elements of up to 2 dex when the stars are young, the Cr abundance seems to be generally less than the equilibrium value, and the Ti abundances almost certainly are below equilibrium even at young ages. These may well be elements for which the abundance would be closer to that predicted by the assumption of a stationary flow-through state, with atoms fed into the atmosphere from below and lost from the top (cf Alecian et al., 2011). In this case the limiting factor determining the atmospheric abundances is the available number density of Cr or Ti brought up from the envelope by diffusion.

As for iron, it is not known whether the decrease in radiative acceleration with declining T_{eff}, or the increased abundance that can be supported as $\log g$ decreases, is the dominant effect during main sequence evolution. It appears that the effect of decreasing radiative acceleration, which may well reduce the supply of Cr and Ti at the bottom of the atmosphere and thus may reduce the supply if these elements are in a stationary flow-through state but not in equilibrium, may dominate, as the abundances of both these elements are observed to decrease strongly with increasing stellar age (cf Alecian & Stift, 2010). It would be of great interest to have computations of equilibrium abundances of Ti and Cr following the evolution of a $3.5 M_{\odot}$ star

for more direct comparison with our results.

5.5.5   Trace heavy elements: Nd and Pr

As far as we know, there are no calculations of the equilibrium abundances of heavy elements such as Nd and Pr near the T_{eff} temperature range of interest to us here, except for the equilibrium stratification calculated for a simplified artificial low-abundance element with $T_{\text{eff}} = 12000$ K by Alecian et al. (2011). This artificial element is expected to behave somewhat like Hg, and the equilibrium abundance computed for it is about -8 dex without a magnetic field, and possibly even smaller high in the atmosphere in the presence of a strong magnetic field. It is not clear to what extent this result is applicable to Nd or Pr. More realistic computations would clearly be of great interest.

In considerably cooler magnetic Ap stars, it is known from modelling of observed spectra that these elements are strongly stratified, with the abundance of Nd as much as 4 dex more abundant high in the atmosphere than near optical depth unity (Mashonkina et al., 2004; Nesvacil et al., 2013). However, we know of no similar stratification models of rare earths in Ap stars in our temperature range. The stars in our sample are hot enough that we have not been able to identify the Nd II lines that would make stratification analysis possible.

We thus have no real evidence as to whether Nd and Pr at the temperatures of our stellar sample have approximately equilibrium abundance distributions, or are in a stationary flow-through state in which these elements are entering the bottom of the atmosphere from below and are being lost to space from the top.

Like the Fe-peak elements, these rare earths are observed to have mean abundances that clearly decrease with stellar age. This could be because the radiative acceleration upward is declining with decreasing T_{eff}, and thus either decreasing the equilibrium abundance in the atmosphere, or decreasing the supply at the bottom of the atmosphere if the flow-through case applies.

5.6   Summary and conclusions

The results of this chapter can be summarised as follows:

1. The abundances of He, Ti, Cr, Fe, Pr and Nd in magnetic Bp stars exhibit evidence of time evolution during their main sequence lifetime. For He, the abundance increases with time from about 2 dex to 0.5 dex below the solar ratio. The Fe-peak and rare-earth element abundances decrease with time. The Fe-peak elements begin about 2 dex overabundant (1.5 dex for Fe) compared to the Sun and approach the solar abundance

ratio with increasing age. Young stars start out about 5 dex and 4 dex overabundant in Pr and Nd respectively, decreasing with time to a value that is still about 2 dex more abundant than in the Sun.

2. No apparent trends in abundance with time are observed for O, Mg or Si.

3. A trend in abundance with magnetic field strength is also observed for He, Ti, Cr, Fe, Pr and Nd. In this case, He decreases in abundance with increasing magnetic field strength, whereas the Fe-peak and rare-earth elements increase in abundance with increasing magnetic field strength.

4. No trend is apparent in abundance versus magnetic field strength for O, Mg, or Si.

5. As temperature increases, the abundances of Fe and Cr saturate at an abundance of about -3 dex and between -3 and -4 dex, respectively. For Cr, the peak value occurs at about 10500 K and decreases with temperature up to about 15000 K. The peak value in the Fe abundance occurs in a temperature range between about 10000 to 13000 K with larger scatter at hotter temperatures with abundances that can approach the solar ratio.

We explored the extent to which various stellar parameters (e.g. rotation period, $v \sin i$, T_{eff}, mass and B_{rms}) influence the evolutionary result by comparing the dispersion in the time evolution plots to the above listed parameters. No obvious correlations are observed with any parameters. Although we can say with certainty that the final derived abundance depends on the physical parameters of the star and contribute to the scatter, it is unclear as to the extent each parameter influences this value. It is quite remarkable that we are able to observe time evolution in abundances with our limited sample between 3-4 $M_{\odot}$.

The individual observed abundances and their variations with stellar age may be explained by diffusion processes. Specifically, we offered two possible scenarios: the "equilibrium abundance distribution" and "stationary flow-through." The former scenario occurs when the tendency for a trace ion to diffuse upwards or downwards vanishes ($g_R = g$). This situation is achieved when the fractional abundance of a specific atom at any position in the stellar atmosphere is satisfied and atomic diffusion stops. The latter case occurs when an insufficient reservoir exists for a specific atomic species below the atmosphere. Here, the species is slowly replenished from below via diffusion while contemporaneously being lost at the top of the atmosphere due to stellar winds. A stationary state can thus be achieved when the flux of atoms at a given height in the atmosphere is constant (but not at the equilibrium value).

The Fe-peak (Ti, Cr, and Fe) and rare-earth (Pr and Nd) abundances decrease with time. In the case of Fe, the equilibrium abundance of about -3 or -3.5 dex is achieved, which implies

an equilibrium abundance distribution. It is uncertain what the equilibrium abundances of Ti and Cr are, however, it is likely similar to that of Fe (between about -3 to -4 dex). These two elements are, in general, less than these equilibrium values and therefore assumed to be in the stationary flow-through state. At present, no equilibrium abundance calculations exist for Pr and Nd for stars within our temperature range of consideration. As such, it is unclear which scenario best describes the distributions of these rare-earth elements.

No strong trend of abundance with age is observed for Mg, however, the average abundance of about -5.2 dex agrees well with predicted abundance profiles and suggests that Mg is an excellent candidate for the equilibrium abundance distribution state. Si is expected to be of the order of 1 dex overabundant and no obvious trend with age is seen. Equilibrium calculations of O suggest that the atmosphere can support values 1 to 2 dex lower than the solar abundance ratio. As the star ages, a decrease in $\log g$ means that the atmosphere can support more ions of O. It therefore seems reasonable to conclude that O may be in the equilibrium abundance distribution state.

The most striking result is the secular increase in the abundance of He with stellar age. The radiative levitation of He is expected to be weak, so as to not play a significant role in the increase in abundance of He with time. We conclude that the observed increase is either the result of significant mixing in the stellar envelope of He that is not related to diffusion, or that there is accretion of He-rich gas from the interstellar medium.

We encourage both diffusion and stellar evolution theorists to utilise the results of this thesis to build upon our current understanding of these processes. More detailed calculations on the equilibrium abundances for elements are necessary to fully interpret the results we present. Further, efforts to follow the evolution of a 3.5 $M_\odot$ star from a series of equilibrium abundance models will help differentiate between competing effects, such as the decrease in gravity and the decrease in radiative acceleration with decreasing T_{eff} with time, that influence the amount of radiative support for atoms in the stellar atmosphere.

Future work will increase the number of stars in the current mass bin to enhance the current sample as well as increase the number of mass bins studied to include more massive stars (4-5 $M_\odot$) and less massive stars (2-3 $M_\odot$) to see if similar trends are observed.

Bibliography

Alecian, G. & Stift, M. J. 2010, A&A, 516, A53

Alecian, G., Stift, M. J., & Dorfi, E. A. 2011, MNRAS, 418, 986

Alecian, G. & Vauclair, S. 1981, A&A, 101, 16

Asplund, M., Grevesse, N., Sauval, A. J., & Scott, P. 2009, ARA&A, 47, 481

Bagnulo, S., Landstreet, J. D., Mason, E., et al. 2006, A&A, 450, 777

Bailey, J. D., Grunhut, J., Shultz, M., et al. 2012, MNRAS, 423, 328

Bailey, J. D. & Landstreet, J., D. 2013a, MNRAS

Bailey, J. D. & Landstreet, J. D. 2013b, A&A, 551, A30

Bailey, J. D., Landstreet, J. D., Bagnulo, S., et al. 2011, A&A, 535, A25

Cramer, N. & Maeder, A. 1980, A&A, 88, 135

Hui-Bon-Hoa, A., LeBlanc, F., Hauschildt, P. H., & Baron, E. 2002, A&A, 381, 197

Kochukhov, O. & Bagnulo, S. 2006, A&A, 450, 763

Kochukhov, O., Bagnulo, S., Wade, G. A., et al. 2004, A&A, 414, 613

Kochukhov, O. & Wade, G. A. 2010, A&A, 513, A13

Krticka, J. & Kubát, J. 2004, in IAU Symposium, Vol. 224, The A-Star Puzzle, ed. J. Zverko, J. Ziznovsky, S. J. Adelman, & W. W. Weiss, 201–207

Kudryavtsev, D. O. & Romanyuk, I. I. 2008, Contributions of the Astronomical Observatory Skalnate Pleso, 38, 229

Kudryavtsev, D. O., Romanyuk, I. I., Elkin, V. G., & Paunzen, E. 2006, MNRAS, 372, 1804

Kudryavtsev, D. O., Romanyuk, I. I., Semenko, E. A., & Yakunin, I. A. 2011, Astronomische Nachrichten, 332, 961

Kunzli, M., North, P., Kurucz, R. L., & Nicolet, B. 1997, A&AS, 122, 51

Kupka, F., Piskunov, N. E., Ryabchikova, T. A., Stempels, N. C., & Weiss, W. W. 1999, A&A, 138, 119

Kupka, F. G., Ryabchikova, T. A., Piskunov, N. E., Stempels, H. C., & Weiss, W. W. 2000, Baltic Astronomy, 9, 590

Landstreet, J. D. 1988, ApJ, 326, 967

Landstreet, J. D., Bagnulo, S., Andretta, V., et al. 2007, A&A, 470, 685

Landstreet, J. D., Dolez, N., & Vauclair, S. 1998, A&A, 333, 977

Landstreet, J. D., Silaj, J., Andretta, V., et al. 2008, A&A, 481, 465

LeBlanc, F. 2003, in Astronomical Society of the Pacific Conference Series, Vol. 305, Magnetic Fields in O, B and A Stars: Origin and Connection to Pulsation, Rotation and Mass Loss, ed. L. A. Balona, H. F. Henrichs, & R. Medupe, 206

Leblanc, F. & Monin, D. 2004, in IAU Symposium, Vol. 224, The A-Star Puzzle, ed. J. Zverko, J. Ziznovsky, S. J. Adelman, & W. W. Weiss, 193–200

Leblanc, F., Monin, D., Hui-Bon-Hoa, A., & Hauschildt, P. H. 2009, A&A, 495, 937

Mashonkina, L. I., Ryabchikova, T. A., & Ryabtsev, A. N. 2004, in IAU Symposium, Vol. 224, The A-Star Puzzle, ed. J. Zverko, J. Ziznovsky, S. J. Adelman, & W. W. Weiss, 315–322

Michaud, G. 2004, in IAU Symposium, Vol. 224, The A-Star Puzzle, ed. J. Zverko, J. Ziznovsky, S. J. Adelman, & W. W. Weiss, 173–183

Michaud, G., Charland, Y., Vauclair, S., & Vauclair, G. 1976, ApJ, 210, 447

Napiwotzki, R., Schoenberner, D., & Wenske, V. 1993, A&A, 268, 653

Nesvacil, N., Shulyak, D., Ryabchikova, T. A., et al. 2013, A&A, 552, A28

Piskunov, N. E., Kupka, F., Ryabchikova, T. A., Weiss, W. W., & Jeffery, C. S. 1995, A&A, 112, 525

Richer, J., Michaud, G., & Turcotte, S. 2000, ApJ, 529, 338

Ryabchikova, T., Leone, F., & Kochukhov, O. 2005, A&A, 438, 973

Ryabchikova, T., Leone, F., Kochukhov, O., & Bagnulo, S. 2004a, in IAU Symposium, Vol. 224, The A-Star Puzzle, ed. J. Zverko, J. Ziznovsky, S. J. Adelman, & W. W. Weiss, 580–586

Ryabchikova, T., Nesvacil, N., Weiss, W. W., Kochukhov, O., & Stütz, C. 2004b, A&A, 423, 705

Ryabchikova, T. A. 2005, Astronomy Letters, 31, 388

Ryabchikova, T. A., Piskunov, N. E., Kupka, F., & Weiss, W. W. 1997, Baltic Astronomy, 6, 244

Shulyak, D., Ryabchikova, T., Mashonkina, L., & Kochukhov, O. 2009, A&A, 499, 879

Stift, M. J. & Alecian, G. 2012, MNRAS, 425, 2715

Théado, S., Vauclair, S., & Cunha, M. S. 2005, A&A, 443, 627

Vauclair, S. 1983, in Saas-Fee Advanced Course 13: Astrophysical Processes in Upper Main Sequence Stars, ed. A. N. Cox, S. Vauclair, & J. P. Zahn, 167

Vauclair, S., Dolez, N., & Gough, D. O. 1991, A&A, 252, 618

Vick, M., Michaud, G., Richer, J., & Richard, O. 2010, A&A, 521, A62

Wade, G. A., Bagnulo, S., Kochukhov, O., et al. 2001a, A&A, 374, 265

Wade, G. A., Ryabchikova, T. A., Bagnulo, S., & Piskunov, N. 2001b, in Astronomical Society of the Pacific Conference Series, Vol. 248, Magnetic Fields Across the Hertzsprung-Russell Diagram, ed. G. Mathys, S. K. Solanki, & D. T. Wickramasinghe, 373

Chapter 6

Conclusions

6.1   Summary

This thesis presents detailed investigations of magnetic Bp stars, ranging from in-depth studies of the magnetic fields and atmospheric abundance distributions of individual stars to larger, broader studies of stratification and abundance evolution in these stars.

For two magnetic stars, HD 133880 and HD 147010, detailed analyses were performed. In both cases, a series of spectropolarimetric observations were utilised to calculate the best-fit magnetic field model (based upon both $\langle B_z \rangle$ and $\langle B \rangle$ measurements as a function of rotational phase) that consisted of colinear dipole, quadrupole and octupole components. Further, this magnetic field geometry was employed in deriving a first approximation to the atmospheric chemical abundance distributions for several elements using the fortran program ZEEMAN.

HD 133880 is a strongly magnetic, rapidly rotating Bp star ($v \sin i \sim 103$ km s^{-1}), which presented many challenges for modelling. In order to adequately model the magnetic field geometry, information about both $\langle B_z \rangle$ and $\langle B \rangle$ is required. A plethora of $\langle B_z \rangle$ measurements from Landstreet (1990), as well as four new polarimetric observations, indicate that the magnetic field variations differ in a significant way from a simple sinusoid: $\langle B_z \rangle$ varies from about -4000 to $+2000$ G with a strong quadrupolar component. The fast rotation made it impossible to measure $\langle B \rangle$ from Zeeman splitting. Instead, $\langle B \rangle$ was estimated using the techniques outlined by Preston (1971), in which the widths of two spectral lines of a given element, one with a large and the other a small Landé factor, were compared (i.e. lines that are strongly affected by the magnetic field to ones that are not). Employing this technique, it was found that the surface magnetic field strength varied from about 10 to 20 kG near the positive and negative magnetic poles, respectively. This information allowed the derivation of a new field geometry: $i = 55°$, $\beta = 78°$, $B_d = -9600$ G, $B_q = -23200$ G, and $B_{oct} = +1900$ G. Using this magnetic field geometry, a detailed abundance analysis using a three-ringed abundance model was em-

ployed that encompassed both magnetic poles and the magnetic equator because both magnetic hemispheres are clearly visible during the stellar rotation. The abundance distribution of most elements (Si, Ti, Cr, Fe, Pr, Nd) were more abundant at the negative magnetic pole as compared to the positive magnetic pole and were well in excess of the solar abundance ratios.

HD 147010, a hot (T_{eff} = 13000 K), high-field magnetic Bp star ($\langle B_z \rangle$ varies from about −2000 to −5000 G), was analysed using seven spectropolarimetric observations. The dataset was sufficient to obtain a first-order model of the magnetic field and obtain the abundance distribution of He, O, Mg, Al, Si, Ca, Ti, Cr, Fe, Ni, Sr, La, Ce, Pr, Nd, and Sm using a simple model of uniform abundance in each of two rings in the observed magnetic hemisphere with equal spans in co-latitude. The adopted magnetic field geometry consists of $i = \beta = 39°$, B_d = −21300 G, B_q = 30300 G, and B_{oct} = −800 G. The analysis revealed large overabundances of Fe-peak and rare-earth elements relative to the solar ratios. In all cases where strong variability in surface chemistry was observed, abundances were higher near the magnetic equator compared to values near the magnetic pole. In fact, HD 147010 is highly rich in rare-earth elements that are of the order of 10^5 times more abundant than in the Sun.

Evidence is available that indicates that the abundance of Si derived from lines of Si II and Si III leads to discordant results in B-type stars (see the study of HD 45583 by Semenko et al., 2008). It is found that different abundances need to be assumed for Si II and Si III in order to adequately model the observed line profiles.To further investigate this phenomena, a comprehensive study of different kinds of B-type stars was carried out to clarify which classes exhibit this discrepancy and to identify any regularities in the phenomena. The stars studied ranged in T_{eff} from about 10500 to 15000 K and included normal late B stars (that do not, in general, have detectable magnetic fields), the magnetic Bp stars (with strong magnetic fields and overabundances of Fe-peak elements) and HgMn stars which show overabundances of elements such as P, Mn, Ga and Hg, but are non-magnetic. Spectrum synthesis was carried out using ZEEMAN and for each class of star accurate abundances of Si II and Si III were determined. Multiple lines of Si II were used to deduce the abundance. The Si III abundances were found using the mulitplet (2) triplet $\lambda\lambda$ 4552, 4567, and 4574.

All the magnetic Bp stars exhibit a discordance between the derived abundances of the first and second ions of Si, with abundances derived from the latter being between 0.6 to 1.7 dex higher. The same behaviour is observed in the non-magnetic stars, but to a much lesser extent. Only three stars do not exhibit any noticeable discrepancy: HD 22136 (normal), HD 57608 (HgMn) and HD 27295 (HgMn). These stars are the only ones for which the microturbulence parameter (velocity distribution that de-saturates spectral lines) is significantly different from zero. This suggests that these stars have sufficient convective mixing in their atmospheres to produce a well-mixed environment in which this discrepancy cannot arise. A possible explana-

tion is vertical abundance stratification. In general, the stronger Si II lines will be formed higher in the atmosphere whereas the weaker Si III lines are formed deeper. It was found that a simple stratification model that has a reduced abundance of Si higher as compared to lower in the atmosphere can explain a large part of the discrepancy between the abundances derived from both ions of Si for magnetic Bp stars and may explain completely the discrepancy observed in both normal and HgMn stars.

Magnetic Bp stars exhibit large over/underabundances of many elements in their atmospheres that are probably the result of diffusion processes. Little is known about the time evolution of these anomalous abundances, nor the role that diffusion may play in maintaining them, during the main sequence lifetime of these stars. Therefore, we have performed an analysis, based on spectropolarimetric observations of a sample of 15 cluster member magnetic Bp stars, that effectively follows the abundance evolution on the main sequence of a 3.5 $M_\odot$ star. Using high-dispersion spectra collected by the ESPaDOnS spectropolarimeter and FEROS spectrograph of magnetic Bp stars with masses between 3 and 4 $M_\odot$, we performed spectrum synthesis on all stars in our sample using the program ZEEMAN, which can take into account the effects of the magnetic field. For each star, abundances of He, O, Mg, Si, Ti, Cr, Fe, Pr and Nd are obtained. For all magnetic Bp stars in our sample, we plotted the derived abundances against their cluster age. By restricting our study to a specific mass range we are, to a first approximation, evolving a single 3.5 $M_\odot$ magnetic Bp star in time. During the main sequence lifetime we observed clear, systematic variations in the atmospheric abundances of He, Ti, Cr, Fe, Pr and Nd. For all elements except He, the atmospheric abundances decreased with age towards the solar abundance for the Fe-peak elements and towards a value at least 100 times more abundant than in the Sun for the rare-earth elements. He is always underabundant compared to the Sun, evolving from about 1% up to 10% of the solar He abundance. We attempt to interpret the observed abundance variations in the context of radiatively driven diffusion theory, which appears to provide a framework to understand some, but not all, of the anomalous abundance levels and variations that we observe.

6.2   Future Work

Many avenues of research are still available in the study of magnetic Ap/Bp stars. Continued detailed analyses of hot magnetic Ap/Bp stars is still necessary. Although the list of hot magnetic Ap stars for which detailed abundance analyses is growing (thanks in part to the efforts outlined in this thesis) more work is necessary. The investment in observing time, CPU cycles and man hours required to perform Magnetic Doppler Imaging (MDI; see e.g. Kochukhov et al., 2004; Kochukhov & Wade, 2010) is very large, because observations in all four Stokes'

parameters is necessary to map the magnetic field and abundance patches on the surface of these stars. As a result, the comparably simplistic modelling offered by programs such as zeeman are essential to indicate which targets are worthy of that time investment.

More work will be done in the study of the time evolution of abundances in magnetic Ap/Bp stars. This thesis presented a study of stars between 3 - 4$M_{\odot}$, limiting the mass range because mass is a determining factor in the evolution of stars. Further studies will build upon this research, adding two more mass bins between 2 - 3$M_{\odot}$ and 4 - 5$M_{\odot}$. The larger of the two proposed mass bins will also extend the $T_{\rm eff}$ of our research above about 15000 K, the threshold where, above this value, non-LTE effects may be important (see Przybilla et al., 2011). As a result, the conventional approach to assume a completely LTE atmosphere in computing synthetic spectra may not be realistic. However, recent work by Nieva et al. (2012) suggests that the use of an LTE synthesis code can yield correct line profiles and derived abundances up to $T_{\rm eff} \sim 22000$ K for suitably chosen spectral lines. This research is essential to furthering our understanding of diffusion theory by providing the first observational constraints on the time evolution of the anomalous abundances in magnetic Ap/Bp stars, as well as clarifying the role that diffusion may play in maintaining them.

Bibliography

Landstreet J. D., 1990, ApJL, 352, L5

Nieva, M.-F. & Przybilla, N. 2012, A&A, 539, A143

Preston G. W., 1971, ApJ, 164, 309

Przybilla, N., Nieva, M.-F., & Butler, K. 2011, Journal of Physics Conference Series, 328, 012015

Semenko, E. A., Kudryavtsev, D. O., Ryabchikova, T. A., & Romanyuk, I. I. 2008, Astrophysical Bulletin, 63, 128

Curriculum Vitae

Name: Jeffrey Bailey

Post-Secondary Education and Degrees: University of Victoria
Victoria, BC
2003 - 2008 BSc., Combined Major in Physics & Astronomy

University of Western Ontario
London, ON
2008 - 2009 MSc., Astronomy

University of Western Ontario
London, ON
2010-2013 PhD., Astronomy

Honours and Awards: Administration Teaching Assistant Award
2012-2013

Related Work Experience: Teaching Assistant
University of Western Ontario
2008 - 2013

Publications:

1. "The surface chemistry of the magnetic Ap star HD 147010", **Bailey, J. D.**, Landstreet, J. D., 2013, MNRAS, doi: 10.1093/mnras/stt635

2. "Abundances determined using Si II and Si III in B-type stars: evidence for stratification and non-LTE effects", **Bailey, J. D.**, Landstreet, J. D., 2013, A&A, 551, A30

3. "An analysis of the rapidly rotating Bp star HD 133880", **Bailey, J. D.**, Grunhut, J., Shultz, M., Wade, G., Landstreet, J. D., Bohlender, D., Lim, J., Wong, K., Drake, S., Linsky, J., and the MiMeS Collaboration, 2012, MNRAS, 423, 328

4. "Magnetic field and atmospheric chemical abundances of the magnetic Ap star HD 318107", **Bailey, J. D.**, Landstreet, J. D., Bagnulo, S., Fossati, L., Kochukhov, O., Paladini, C., Silvester, J., Wade, G., 2011, A&A, 535, A25

Proceedings

1. "Magnetic Field of the Ap Star HD 318107", **Bailey, J. D.**, Landstreet, J. D., 2012, in Stellar Polarimetry: From Birth to Death, Eds. Jennifer Hoffman, Barb Whitney, and Jon Bjorkman, AIP Conference Proceedings (Melville, New York), Volume 1429, pp. 86 – 89